Author:
Thain, A

Title:
A d.c. SQUID susceptometer for the study of dHvA oscillations in heavy fermion compounds.

A d.c. SQUID susceptometer for the study of dHvA oscillations in heavy fermion compounds.

A. Thain

February 26, 1999

A dissertation submitted to the University of Bristol in accordance with the requirements of the degree of Ph.D. in the Faculty of Science, Department of Physics.

Abstract.

A d.c. SQUID susceptometer has been constructed, capable of observing de Haas-van Alphen oscillations at 3 mK in a magnetic field of 17 T. Two key problems that limited the sensitivity of the device were vibrations originating in the superconducting solenoid and the presence of a large field dependent background susceptibility. The first problem has been solved to the extent that 17 T experiments can be performed if the magnet is swept at less than 0.005 T/min, and any background changes in the phase of the susceptibility can be compensated for, by a dynamic electronic balancing system.

A series of preliminary experiments have been conducted on a single $CeCu_2Si_2$ crystal. While oscillations were observed that were definitely due to the de Haas-van Alphen effect, later background tests suggest that the majority of oscillations came from indium contaminants. The likelihood of the remaining oscillations originating in the sample is also discussed, although this possibility is viewed with caution. This study provided an unprecedented sensitivity to high frequency oscillations, and their absence is analysed in detail. The metamagnetic transition of $CeCu_2Si_2$ is also studied and on the basis of these experiments it would appear that the height of the peak in the susceptibility at the transition is dependent upon sweep rate.

The problem of the spurious oscillations is discussed and a series of modifications are proposed to eradicate them and further improve the sensitivity of the device. The estimated susceptibility resolution of the susceptometer could then be reduced from 2×10^{-5} to 10^{-8} (dimensionless S.I. units).

Author's Declaration.

I declare that the work in this dissertation was carried out in accordance with the Regulations of the University of Bristol. The work is original except were indicated by special reference in the text and no part of the dissertation has been submitted for any other degree.

Any views expressed in the dissertation are those of the author and in no way represent those of the University of Bristol.

The dissertation has not been presented to any other University for examination either in the United Kingdom or overseas.

SIGNED: Andrew Thain DATE: 26 2 1999

Acknowledgments.

I would like to thank my supervisors Phil Meeson and Mike Springford for their ideas and suggestions during the course of this study. This work has benefitted from the excellent technical support and helium production of Bob Wiltshire, Stewart Field and Dave Engeldew. There has also been a lot of help from all the other members of the group, past and present, Alex Bach, Dan Bintley, Nick Clayton, Michael Cuthbert, Martin Dann, Bob Doubble, Dave Ellison, Andrew Griffiths, Steve Hayden, Rob Hill, Hiroshi Ito, J.T.Janssen, Sankar Talari and Vlad Zavaritsky. Extra special thanks must go to my family and my friends outside the department, particularly Christiane for all her patience and support.

Contents

Chapter 1

Introduction to interactions in condensed matter physics.

The work contained within this thesis concerns the magnetic properties of heavy fermion compounds - alloys containing Lanthanide and Actinide elements combined with various other metals from the periodic table. These are not materials that occur in large quantities naturally, neither do they have any immediately obvious technological applications, so perhaps the first question to address is why there is such interest in them.

The distinguishing feature of the heavy fermion alloys is that they display, in a very pronounced manner, interactions between electrons in the solid state. It is at first surprising that these interactions are not more apparent in all materials, considering they all contain upwards of 10^{23} electrons travelling around a similar number of positive ions. However, due to the fact that two electrons cannot occupy the same quantum state, their opportunities to interact with each other are drastically reduced.

When inter-electron interactions are apparent they lead to some of the most remarkable behaviour in materials, such as magnetism and superconductivity, but even the behaviour of the simplest metals is not currently exactly predictable on account of interactions. In an alternative direction to trying to understand existing materials there is the sense that condensed matter is a subject that is very forward looking. There are 137 elements in the periodic table and so far, experiments on alloys have only begun in earnest in the last couple of decades, leading to the discovery of high temperature superconductors and heavy fermion compounds. The reason that these multicomponent materials display behaviour different from just the sum of their parts is again due to the fact that the electrons are interacting.

Apart from the conceivable technological results of this approach there are also the possible benefits for physics in general. There is a large amount of cross fertilisation between condensed matter physics and other branches, such as the BCS theory of superconductivity inspiring the Higgs mechanism of particle physics. Presumably any discovery in condensed matter physics might be of use to researchers in areas less amenable to experimental study. Also of note is the similarity between certain aspects

of heavy fermion systems and high temperature superconductors. They are both suspected of having unconventional superconducting pairing and strong Coulomb interactions at the rare earth and copper sites respectively.

Low temperature physics can make an important contribution to this study because without the randomising effects of temperature, the electron correlations become more apparent. This is particularly true for heavy fermions, whose unusual properties only manifest themselves below a characteristic temperature, T_{coh}.

The idea behind studying the magnetic properties, is that by exploiting a property known as the de Haas-van Alphen effect it is possible to find the area of the Fermi surface, the purity of the material and also the effective masses of the quasiparticles. The last value is of particular interest because it is a measure of interaction strength, but it is also what makes the experiments challenging, requiring ultra low temperatures and sensitive instrumentation.

The heavy effective masses have proved an equal problem for theorists and up to now band structure calculations have succeeded in predicting the gross features of the Fermi surface, but the values for the effective masses are often orders of magnitude too small. There are microscopic theories, that attempt to explain the enhanced masses, but so far it has not been possible to successfully marry these with traditional calculational schemes.

An important task for the experimentalist must therefore be to provide detailed Fermi surface measurements accompanied by measurements of the effective mass. It is the de Haas-van Alphen effect (dHvA) that can provide exactly these properties. This work describes the construction of a d.c. SQUID dHvA spectrometer and some preliminary experiments performed on it. Most of the study concerned the heavy fermion compound $CeCu_2Si_2$. Although dHvA oscillations were observed, the majority of them were conclusively ascribed to indium contaminants present in the experimental area. There remain some oscillations whose origin is more ambiguous and these are analysed.

This thesis will outline some of the salient features of the heavy fermion compounds and the current theories that attempt to explain them. There will then follow a brief introduction to the de Haas-van Alphen effect. The refrigerator will then be described, with particular emphasis placed on the d.c. SQUID susceptometer. The compound $CeCu_2Si_2$ is then reviewed. The results of the experiment will be outlined in chronological order and they will then be interpreted in a separate chapter.

Chapter 2

Heavy fermion phenomena.

2.1 Introduction.

Heavy fermion systems are metallic rare-earth or actinide compounds with extremely strong electronic correlations, reflected by the fact that the f-states exhibit both localised behaviour at high temperatures, whilst appearing as delocalised but strongly renormalised quasiparticles at lower temperatures. The interest in these compounds is that they lie at the intersection of a large number of long-standing problems in the physics of metals. The first compound to display these characteristic properties was $CeAl_3$, in 1975 [1], although all of the examples here will be in reference to $CeCu_6$, a more extensively studied heavy fermion. Discussion of $CeCu_2Si_2$ is postponed to a later chapter because this compound has the peculiarity of being superconducting and also displays a range of other sample dependent effects. The definitive properties of heavy fermion systems are displayed in their susceptibility, specific heat and thermal and electrical conductivities.

2.2 Susceptibility.

As can be seen in figure 2.1, the high temperature susceptibility is of the Curie Weiss form, $\chi = C/(T - \Theta_{CW})$, indicating that the Ce ions remain magnetic inside the Cu lattice. For heavy fermions in general Θ_{CW} is negative, and the effective moment, deduced from C, lies between the value expected for a free atom with a single f-orbital occupied, and that obtained for a free atom that respects Hund's rules and has 2 or 3 f-orbitals occupied. Deviations from this form are seen below 100 K but they can still be ascribed to local f-electron configurations. In this temperature regime, they are essentially indistinguishable from a host of other rare-earth or actinide compounds, but on lowering the temperature (inset) the susceptibility saturates to a value (up to 0.1 emu mol^{-1}) typically two orders of magnitude larger than the temperature-independent Pauli susceptibility in an ordinary metal. Neutron scattering investigations in this region show ordered moments of only $\approx 10^{-2}\mu_B$ [3], so the bulk magnetism is presumably of itinerant origin. If one were to interpret the low temperature

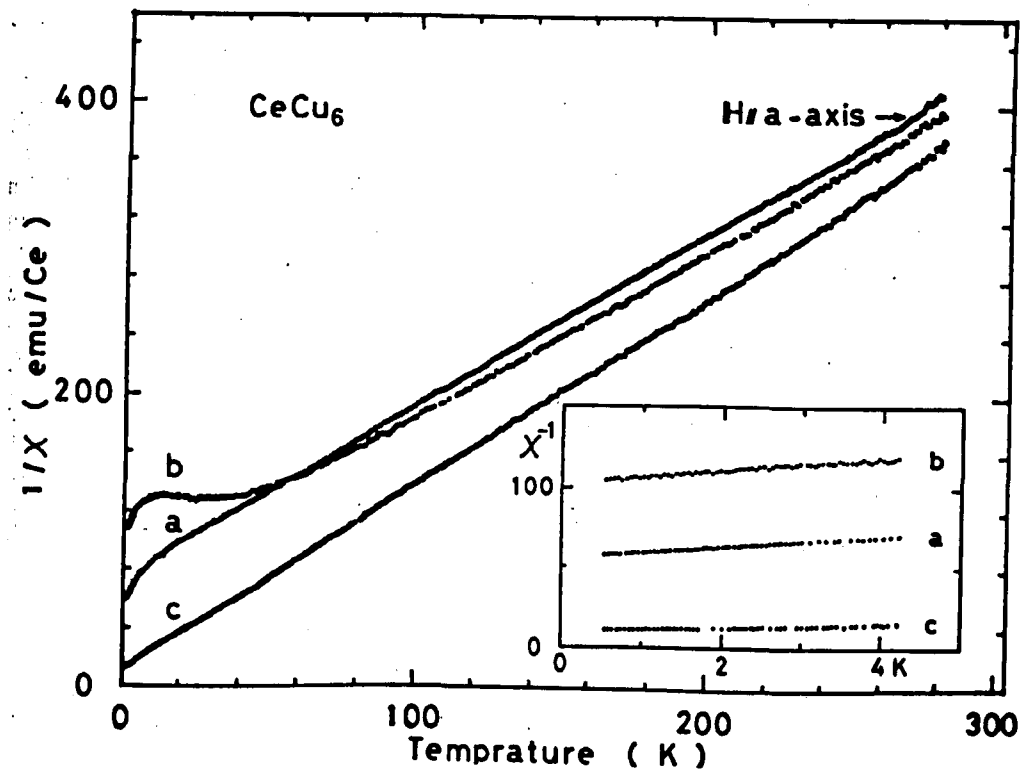

Figure 2.1: The temperature variation of susceptibility for $CeCu_6$. After Onuki *et al.* [2].

susceptibility in terms of Landau's Fermi liquid theory, it signals the presence of quasiparticles with effective masses enhanced by approximately 1000 times that of simpler metals. It is also evident from figure 2.1 that the susceptibility is strongly orientationally dependent. There is also a strong pressure dependence, and heavy fermion magnetostriction exceeds that of transition metals by at least two orders of magnitude.

2.3 Specific heat.

Due to the thermodynamic relation, $\gamma = C_p/T = dS/dT$, specific heat measurements provide an unambiguous picture of entropy changes in a system, and it is here where heavy fermions display perhaps their most outstanding property. It is also from where they derive their somewhat arbitrary present definition, as materials with a low temperature γ in excess of $400\,\mathrm{mJmol^{-1}K^{-2}}$.

Independent electron theory predicts that, on reducing the temperature, γ should become constant, yet in these compounds (see figure 2.2) it is seen to remain highly temperature dependent to temperatures below 10K. Three regimes can be defined: (i) Above 10 K, one observes the usual decrease with decreasing T. In some cases Schottky anomalies are observed, corresponding to crystalline effective field (CEF) excitations. (ii) Between 5 and 10 K there is weak temperature dependence. (iii) Below 4 K there is an enormous increase of γ with decreasing T. It can be seen that γ extrapolates to a value of 1.67 $\mathrm{Jmol^{-1}K^{-2}}$ at 0 K. This value is strongly enhanced over the value measured in ordinary

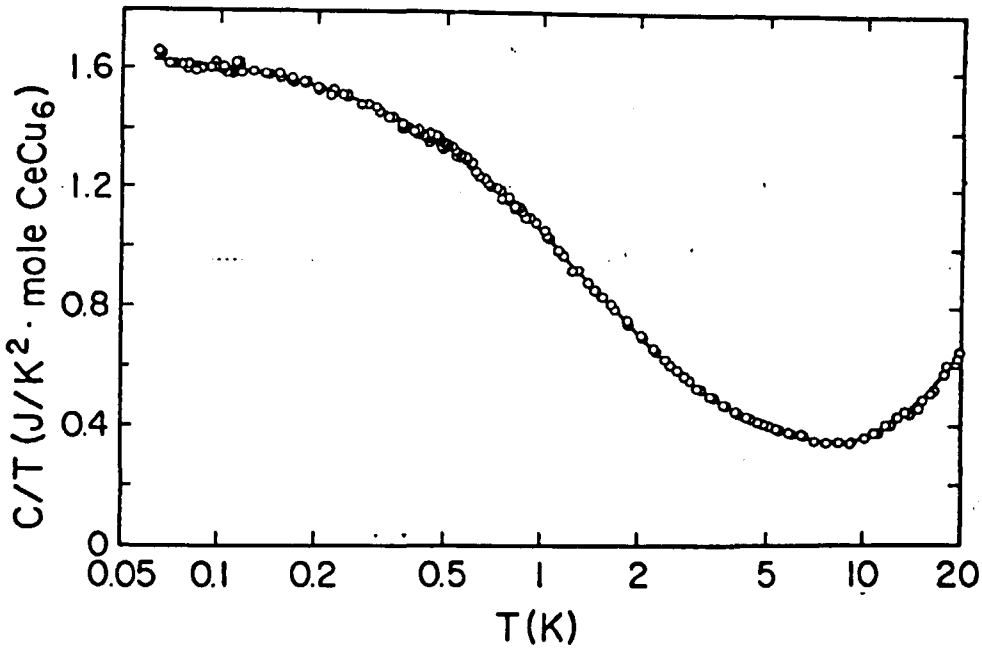

Figure 2.2: The specific heat of $CeCu_6$. After Amato *et al.* [4].

metals, where typically $\gamma \approx 1 \text{mJmol}^{-1}\text{K}^{-2}$. Once more, the result can be interpreted in terms of strongly enhanced effective masses. The amount of enhancement is highly sensitive to impurities. For example, substitution of 3.4 % of the uranium in UBe_{13} by thorium leads to 37 % increase in γ, but the substitution by a similar amount of lutetium depresses γ by the same amount [5].

2.4 Resistivity.

The resistivity curve for $CeCu_6$ (see figure 2.3) displays the characteristic regimes, defined for heavy fermions. The resistivity falls from room temperature and has a broad minimum around a characteristic temperature T^*. The temperature then rises with a $-\ln(T)$ dependence to a second defined temperature, T_{coh}, where it then falls with a T^2 dependence. Once more the low temperature regime follows the dependence predicted by free electron theory but with effective masses two orders of magnitude larger.

2.5 Miscellaneous properties.

The heavy fermions are defined as a group by resistivity, susceptibility and specific heat but there are other properties that lend clues to their nature. Firstly they tend to only form when there is a large separation (> 3.5Å) between neighbouring f-atoms, indicating that they require an absence of direct f-f wavefunction overlap. Like all metals they form one of three ground states, normal, superconducting or antiferromagnetic, and in the latter two cases, the large entropies involved at the

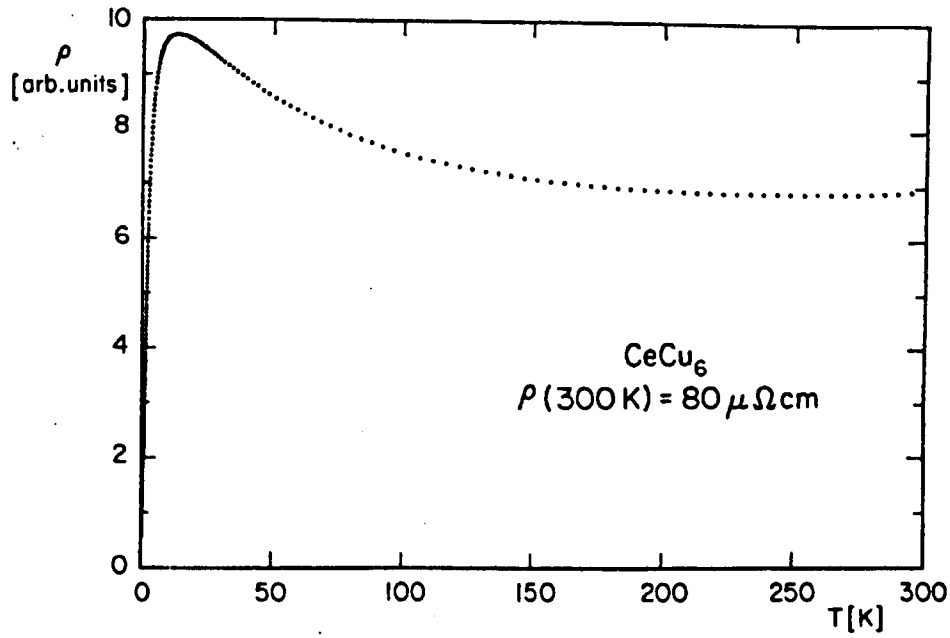

Figure 2.3: The resistivity of $CeCu_6$. After Ott *et al.* [6].

transitions indicate that it is the heavy quasiparticles that order in each case. This aspect will be discussed in greater detail with respect to $CeCu_2Si_2$ in chapter 6.

It is natural to enquire whether there are any other metallic systems that display some of the same behaviour as the heavy fermions. A group of alloys consisting of non-magnetic hosts doped with small concentrations of magnetic impurities, known as the Kondo alloys, do indeed share many of the same properties at and above T^*. Most notably, they show a minimum in the resistivity. Figure 2.4 is a sketch comparing the properties of conventional metals, heavy fermions and Kondo alloys.

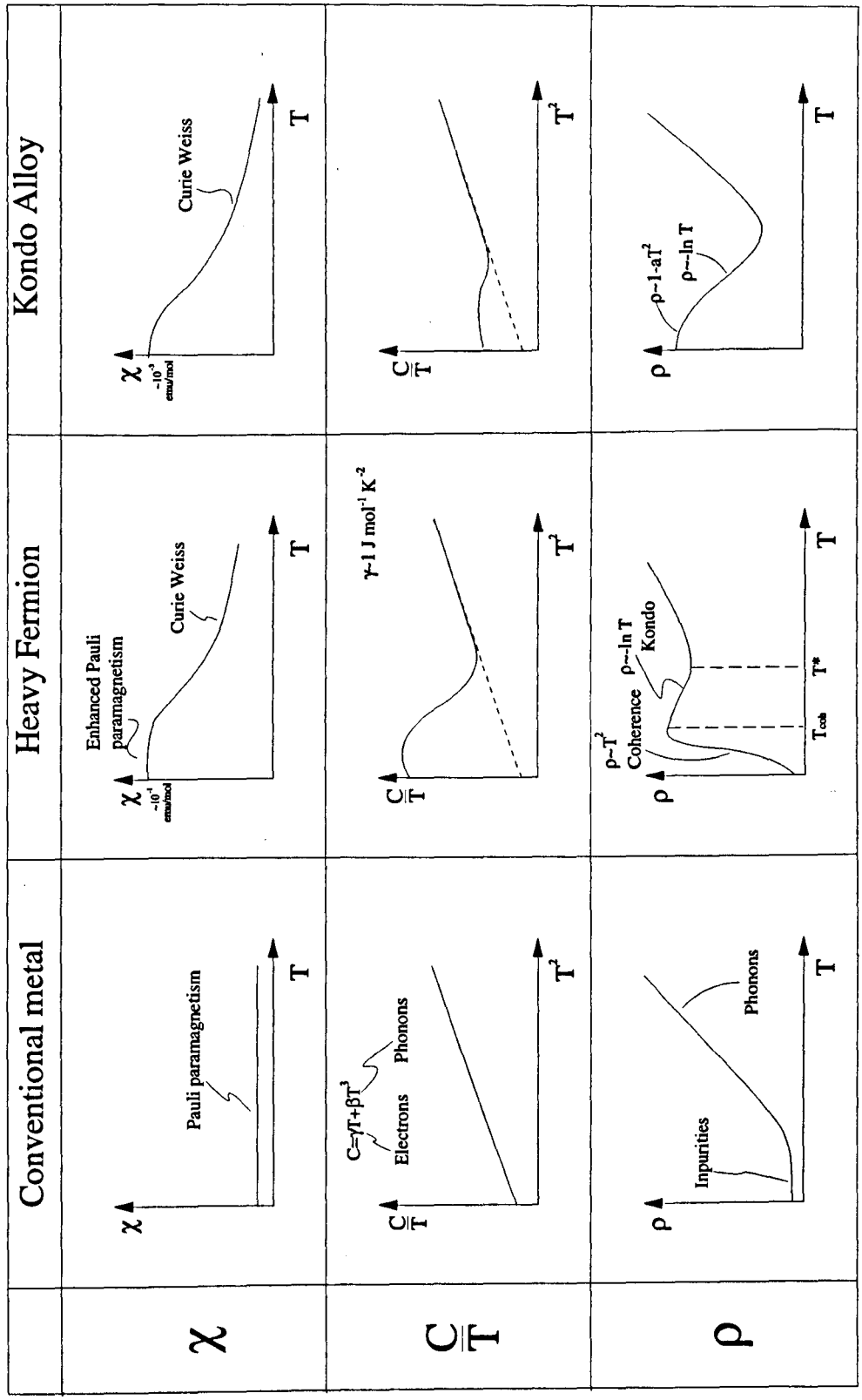

Figure 2.4: Sketch showing the main characteristics of conventional metals, heavy fermions and Kondo alloys.

Chapter 3

Heavy fermion theory.

3.1 Overview.

This chapter will briefly outline some of the current ideas employed in the study of heavy fermion systems. Perhaps one of the first questions to ask is why theories that have treated electrons as nearly independent, have been so successful in the description of more conventional metals. The natural interpretation for this is in terms of Landau Fermi-liquid theory, where the concepts of quasiparticles and effective masses are defined. Also presented are some of the microscopic models that attempt to predict the origin of the large effective masses encountered.

It can be seen that most of the high temperature properties of heavy fermions map onto those of the (well understood) Kondo alloys and in this sense there is some theoretical basis. However, it is the low temperature behaviour that single out the heavy fermions as a group and any successful theory must provide a description of this state. More specifically, the real goal must be a material specific description capable of predicting band structure and effective masses. There has been a tendency to employ 'Kondo like' models (and vocabulary) in the description of this state, although it is entirely possible that the correct description will come from a different starting point.

3.1.1 The Landau Fermi liquid.

The earliest quantum mechanical formulation of a metal was that of Sommerfeld. He neglected Coulomb interactions and just treated the electrons as filling up the energy levels in a potential well. This simple model had remarkable success in predicting observed specific heats, although it was not clear why. Sommerfeld's model relied on the electron occupancy being unity below the Fermi surface and zero above it. It seemed that, even at zero temperature, the strong inter-electron interactions would blur the Fermi surface and make this description invalid.

A clue to why this does not happen came from Homi Bhaba who realised that when one considers both momentum and energy conservation in a two particle scattering event near the Fermi surface, there is a very limited amount of allowed momentum space for the particles to scatter into, leading to

the relation

$$\frac{1}{\tau} \propto (p - p_F)^2 \tag{3.1}$$

where τ is the lifetime of an electron in a particular state with absolute momentum p, above the Fermi momentum p_F. Consequently, if there are no electrons appreciably above the Fermi energy, the situation tends to remain this way.

Lev Landau expanded on this idea, (originally in an attempt to understand liquid ^{3}He [7]), and imagined what happens to the Sommerfeld model as one adiabatically turns on electron-electron interactions. He proposed that certainly the energy levels would be modified, but because of the limited scattering, the energies of the various states would not evolve to cross each other or come in contact, so there would be a one to one correspondence with the states in the interacting system and the non-interacting one.

All the above can be performed with the addition of an extra particle in momentum state p_0. Similar reasoning to above predicts that the momentum of this extra particle will remain as before but its energy will have changed to $E(p_0)$. This new particle is known as a quasiparticle and the excitation energy required to produce it is

$$\varepsilon_{p_0} = E(p_0) - E_0 \tag{3.2}$$

As the temperature is increased, the number of quasiparticles grows (although stays small) so we no longer have a single-body problem. However the limited amount of momentum space in which to scatter means that the system is still comparatively stable and in the asymptotic low energy limit, the number of particles in each momentum state becomes a constant of motion.

Consequently, the energy of a gas of quasiparticles, can be expressed as a functional of the number of quasiparticles, n_p, at momentum p. In the (low temperature) low density limit, the energy can be expanded in small deviations of particle number $\delta n_{p\sigma} = n_{p\sigma} - n^0_{p\sigma}$

$$E(\{n_{p\sigma}\}) = E_0 + \sum_{p,\sigma} \varepsilon_p \delta n_{p,\sigma} + \frac{1}{2} \sum_{p,p',\sigma,\sigma'} f_{p\sigma,p'\sigma'} \delta n_{p\sigma} \delta n_{p'\sigma'} + \cdots \tag{3.3}$$

where

$$\varepsilon_p = \frac{\delta E}{\delta n_{p\sigma}} \tag{3.4}$$

and

$$f_{p\sigma,p'\sigma'} = \frac{\delta^2 E}{\delta n_{p\sigma} \delta n_{p'\sigma'}} \tag{3.5}$$

The first summation is the single particle contribution from each quasiparticle and the second one represents the change in quasiparticle energy due to the quasiparticles $\delta n_{p'\sigma'}$ at momentum p'. From this equation, Landau was able to deduce two important consequences.

Firstly, as an electron moves through the metal it produces a trail of quasiparticle excitations behind it, changing its inertia and modifying its energy as follows

$$\varepsilon(p) = \frac{p^2}{2m^*} - \varepsilon_F \tag{3.6}$$

i.e.

$$m^* = (1 + F_1^s)m \tag{3.7}$$

where F_1^s is one of the parameters that Landau chose in his expansion so that it converges quickly and also produces physically meaningful coefficients. This mass renormalisation corresponds to the energy levels being compressed and has the consequence of enhancing the linear contribution to specific heat

$$\gamma^* = \frac{m^*}{m}\gamma \tag{3.8}$$

Interactions with the cloud of quasiparticles also allow it to be spin polarised, so likewise the magnetic susceptibility is renormalised

$$\chi^* = \frac{m^*}{m(1 - F_0^a)}\chi \tag{3.9}$$

Here F_0^a is another Landau parameter.

Heavy fermions can be interpreted in this framework, but unlike for ^{3}He it has proved difficult to produce a quantitative description. The main reason for this being that the complicated crystallographic environment requires one to also include the effects of a band mass.

3.1.2 The molecular model.

A very simple model that introduces some of the phenomena present in Kondo alloys and the heavy fermion problem is that of electronic behaviour in molecules [8]. A schematic diagram is shown in figure 3.1.

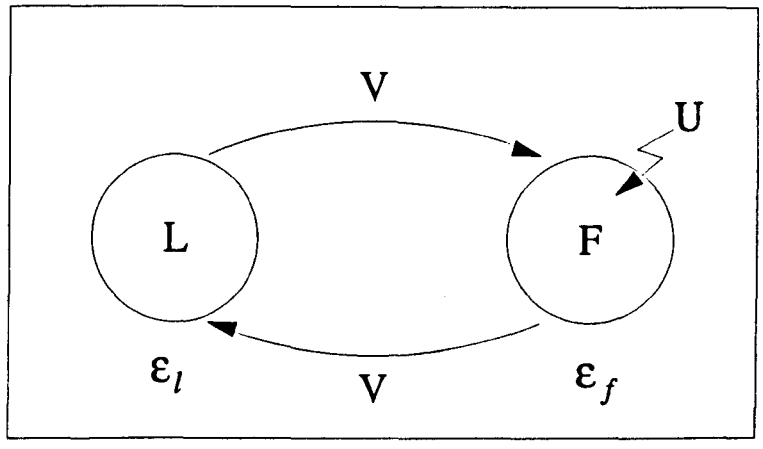

Figure 3.1: A schematic representation of electron hybridisation in a molecule. After Fulde [8].

The two spheres represent the ligand (L) and the f-orbital (F). The f-orbital is at a lower energy than the L orbital ($\varepsilon_f < \varepsilon_l$), but there is an energy penalty, U, for putting both electrons in the f-orbital, because of Coulomb repulsion. V represents the small ($V \ll (\varepsilon_l - \varepsilon_f)$) hybridisation energy between the two orbitals. The complete Hamiltonian is thus

$$H = \varepsilon_l \sum_\sigma l_\sigma^+ l_\sigma + \varepsilon_f \sum_\sigma f_\sigma^+ f_\sigma + V \sum_\sigma (l_\sigma^+ f_\sigma + f_\sigma^+ l_\sigma) + U n_\uparrow^f n_\downarrow^f \tag{3.10}$$

The operators $l_\sigma^+, l_\sigma, f_\sigma^+, f_\sigma$ and n_σ^f have their usual meanings and σ represents spin.

Considering first the case when V=0, the ground state of the system (with energy $\epsilon_0 = \epsilon_l + \epsilon_f$) has one electron in each orbit and is fourfold degenerate. The state with both electrons in the ligand orbital is an excited state with energy $2\epsilon_l$, and the state with both electrons in the f-orbital has a very large energy, due to the large Coulomb repulsion, and so will not be considered here. The states are listed below.

	Ground states		Excited state
Singlet	$\|\Phi_{S=0}\rangle = \frac{1}{\sqrt{2}}(f_\uparrow^+ l_\downarrow^+ - f_\downarrow^+ l_\uparrow^+)\|0\rangle$	Singlet	$\|\Phi_{ex}\rangle = l_\uparrow^+ l_\downarrow^+ \|0\rangle$
Triplet	$\|\Phi_{S=1}^1\rangle = f_\uparrow^+ l_\uparrow^+ \|0\rangle$		
Triplet	$\|\Phi_{S=1}^0\rangle = \frac{1}{\sqrt{2}}(f_\uparrow^+ l_\downarrow^+ + f_\downarrow^+ l_\uparrow^+)\|0\rangle$		
Triplet	$\|\Phi_{S=1}^{-1}\rangle = f_\downarrow^+ l_\downarrow^+ \|0\rangle$.		

When V is finite the situation is somewhat different. Now the two singlets $|\Phi_{S=0}\rangle$ and $|\Phi_{ex}\rangle$ become coupled whilst the triplet states remain as before.

The new singlet states are

$$|\psi_0\rangle = \left(1 - \left(\frac{V}{\Delta\epsilon}\right)^2\right)|\Phi_{S=0}\rangle - \frac{\sqrt{2}V}{\Delta\epsilon}|\Phi_{ex}\rangle, \tag{3.11}$$

$$|\psi_{ex}\rangle = \left(1 - \left(\frac{V}{\Delta\epsilon}\right)^2\right)|\Phi_{ex}\rangle + \frac{\sqrt{2}V}{\Delta\epsilon}|\Phi_{S=0}\rangle \tag{3.12}$$

where

$$\Delta\epsilon = \epsilon_l - \epsilon_f \tag{3.13}$$

The eigenvalues are sketched in figure 3.2.

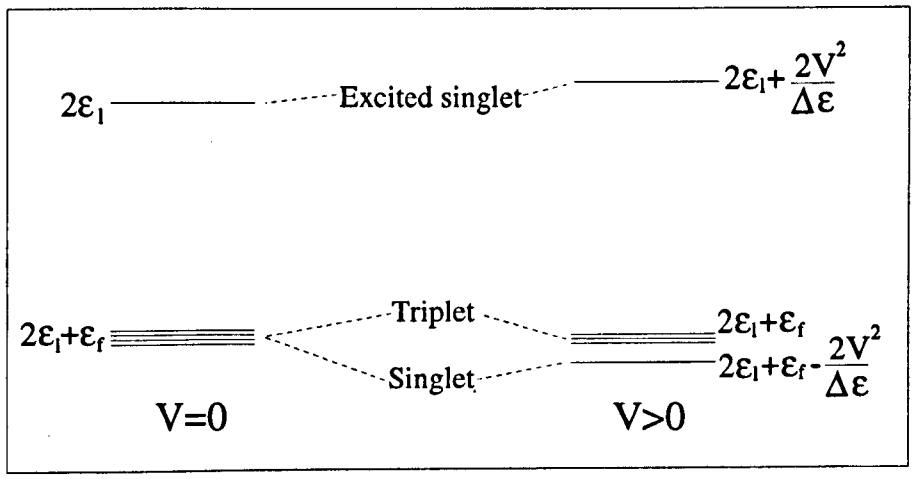

Figure 3.2: A schematic diagram of the energy levels associated with the molecular model. For cerium compounds the excited singlet is typically 2 eV above the triplets and the ground singlet $\approx$ 1 meV below them.

It is now possible to make the analogy to some of the phenomena seen in the heavy fermion compounds. It can be seen that the lowest lying excitation is from the singlet to the triplet states given

by an energy $\frac{2V^2}{\Delta\epsilon}$. One can thus define a characteristic temperature associated with this excitation $T^* = \frac{2V^2}{k_B\Delta\epsilon}$.

At high temperatures ($T \gg T^*$), the triplet and singlet states are both populated and the magnetic character of the f-electron, is evident. The electrons in the L and F orbitals are then effectively decoupled, but the high energy excitation (two electrons in the L orbital), remains. In a metal, one could model this regime as a Fermi sea consisting of conduction electrons, whose masses are slightly renormalised by scattering off the local f-electron magnetic moments.

In the low temperature regime ($T \ll T^*$), the singlet character of the ground state becomes apparent, as the lowest energy level becomes dominantly occupied. Below T^* there are then two types of excitation – a spin excitation with energy k_BT^* and a charge excitation of an electron from the f-orbital to the l-orbital of (larger) energy $\Delta\epsilon$. The presence of many low-energy excitations is reflected in the large specific heat C(T). In the metallic case, the f-degrees of freedom appear as itinerant fermionic degrees of freedom, forming a narrow quasiparticle band near the Fermi energy. The Fermi surface is determined by the number of conduction electrons plus f-electrons.

Although this description shows some of the qualitative features of heavy fermion systems, it is not appropriate because we are dealing with a hybridisation with a band of conduction electrons, not a ligand orbital. In a metal it is possible for the f-electron to hybridise with a range of states, not just one orbital. The extension of the molecular model is the Anderson Hamiltonian, but before discussing that, a simpler model is presented that explains the most notable feature of Kondo alloys – their resistance minimum.

3.1.3 The single ion Kondo effect.

It was noted by Meissner [9] in 1930 that a dilute concentration of certain impurities in metals produced a minimum in the resistance as the metal was cooled, instead of it just levelling off as would be expected from a mechanism involving simply phonon and (temperature independent) impurity scattering. Clearly what was required was some scattering mechanism that increased at lower temperatures. Kondo extended work by Zener [10] who noticed that the resistance minimum was always accompanied by a Curie-Weiss term in the high temperature susceptibility, indicative of localised magnetic moments. Zener considered the interaction of the conducting s-electrons with the localised d-electrons so the Hamiltonian had the form

$$H = H_c + H_v + H_{sd} \tag{3.14}$$

where as usual the non interacting conduction electrons have energy $H_c = \sum_{k,\sigma} \epsilon_k n_{k,\sigma}$ and scattering from non-magnetic impurities is given by H_v. The novel feature is the scattering with magnetic impurities

$$H_{sd} = J\mathbf{S}\cdot\boldsymbol{\sigma} \tag{3.15}$$

which has the Heisenberg form conventionally used for models of ferromagnetism ($J < 0$) and antiferromagnetism ($J > 0$). Zener had calculated the scattering to second order in the coupling constant, J,

but had only found terms which were constant (impurity and magnetic interaction) or rose (phonon contribution) with temperature. Kondo extended the calculation to the third order and found that the magnetic interaction scattering increased on reducing the temperature due to processes where the electron spin is flipped, along with the local moment, producing a compensating change of spin. These produce a logarithmic temperature dependence. The resistivity was thus found to vary as

$$\rho = \frac{3\pi m J^2 S(S+1)}{2\hbar e^2 \varepsilon_F}\left(1 - 4JN(\varepsilon)\ln\left(\frac{k_B T}{D}\right)\right) \tag{3.16}$$

where $\frac{k_B T}{D} \ll 1$ and D is the conduction bandwidth.

Although this result produced the desired rise in resistance there was an unphysical divergence at zero temperature and summing to higher terms only shifted this divergence to a finite, Kondo temperature, $T_K = \frac{D}{k_B}\exp(\frac{1}{2JN(\epsilon_F)})$. A solution applicable down to T=0 was produced by Wilson [11], applying his numerical renormalisation group. This produced the desired low temperature $1 - aT^2$ and higher temperature $-\ln(T)$ dependence. Further confirmation was provided in 1980 when Andrei provided exact solutions of the s-d model using the Bethe ansatz.

3.1.4 The Kondo lattice.

The natural extension of the Kondo problem to model heavy fermion compounds is to calculate the effects of a regular lattice of Kondo ions. This problem was tackled by Doniach [12], for the one dimensional case (the so called Kondo necklace).

Here the Hamiltonian is

$$H = H_K + H_{AF} \tag{3.17}$$

The two terms represent the tendency for Kondo like compensation to form a singlet ground state with a binding energy of

$$W_K \approx \frac{1}{N(\varepsilon_F)}\exp\left(\frac{-1}{N(\varepsilon_F)J}\right) \tag{3.18}$$

and the other term represents the RKKY [13, 14, 15] antiferromagnetic interaction with a binding energy of

$$W_{AF} \approx CJ^2 N(\epsilon_F) \tag{3.19}$$

J is the exchange coupling and C is a constant (≈ 1) governed by the electronic band structure. The dependence upon J for these two terms is plotted in figure 3.3.

Although not of direct quantitative use, this model goes some way to describing the variety of ground states evident in heavy fermion alloys. If the RKKY interaction is dominant the f-electrons order antiferromagnetically, however if singlet formation sets in first, they are screened, leaving only a weak lattice magnetisation. This is indeed thought to correspond to what is observed experimentally [16]. The model is of particular relevance to $CeCu_2Si_2$ where the complicated phase diagram is in part explained in terms of a changing exchange coupling.

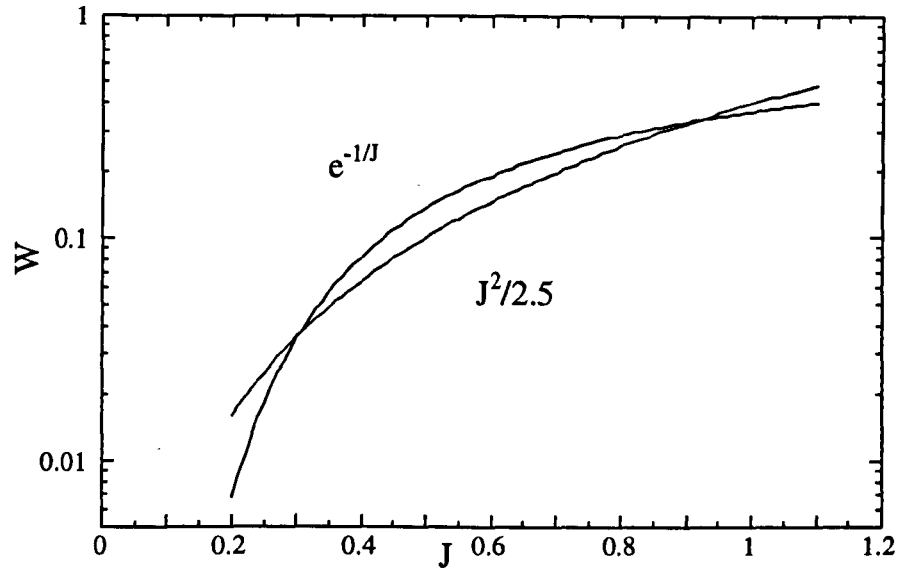

Figure 3.3: A plot of the strengths of the two terms in the Doniach Kondo necklace. For regions where $J < 0.3$ the behaviour is antiferromagnetically ordered and for $J > 0.3$ the spin compensated state arises. The second solution near 1 is out of the range of the approximation scheme used in the model.

3.1.5 The periodic Anderson model.

The Kondo model essentially treats the ions in a dilute magnetic alloy in the same manner as if they were in an insulator, with the addition of exchange effects. However when magnetic impurities are introduced into lattices of non-magnetic metals there is no guarantee that they retain their magnetic character. There can be a variety of reasons for this. Depending upon the relative energies of the conduction electrons and the impurity electrons, it is possible for an electron to drop into the lower state. Also if the ionic levels are degenerate with the conduction electron levels it is possible to have a mixing of the levels and the 'magnetic' electron can lose its localised character. Anderson [17] devised a model that displays these features, in which all the levels in the magnetic ion are represented with a single localised level, and the coupling between localised and band levels is reduced to a minimum.

$$H = H_c + H_i + H_{ci} + H_u \tag{3.20}$$

Here, $H_c = \sum_{k,\sigma} \varepsilon_k c^+_{k,\sigma} c_{k,\sigma}$ represents the conduction electrons, $H_i = \sum_\sigma \varepsilon_i n_{i,\sigma}$, the impurity and $H_{ci} = \sum_{k,i}(V_{i\sigma}(\mathbf{k}) f^+_i c_{\mathbf{k}\sigma} + V^*_{i\sigma}(\mathbf{k}) c^+_{\mathbf{k}\sigma} f_i)$ is the hybridisation term and $H_u = U/2 \sum_{i \neq i'} n_i n_{i'}$ is the double occupancy energy penalty.

This is an approximate but presumably very complete description, and in different limits produces the s-d model and the molecular model. In a similar manner in which the s-d model was extended by Doniach to make a model closer to that of heavy fermions so the Anderson model can be extended to a periodic case. The validity of this procedure is not clear, because from the s-d model we can see that the ionic separation is shorter than the Kondo screening length. However the model has been successful in describing much of the observed behaviour, most notably the appearance of a resistance

maximum at T_{coh}.

$$H = \sum_{k,\sigma} \varepsilon_k n^c_{k,\sigma} + \sum_{i,m} \varepsilon_f n^f_{i,m} + U \sum_{i=1}^{N} \sum_{m,m'} n^f_{i,m} n_{i,m'} + H_{cf} \tag{3.21}$$

The terms have similar meanings to before, but now there is also a summation over lattice sites i, and f-electron angular momentum state m. This Hamiltonian has not yet been solved exactly, but information can be extracted if certain assumptions are made. A reasonable starting place is to assume that U is infinitely large, because the double f-electron state is known to be well above the Fermi energy in most cerium compounds. A mean field solution to this approximation has been obtained [18, 19] using the slave boson method [20], assuming a coherent boson field. In this scheme the entire Kondo lattice forms a macroscopic singlet state.

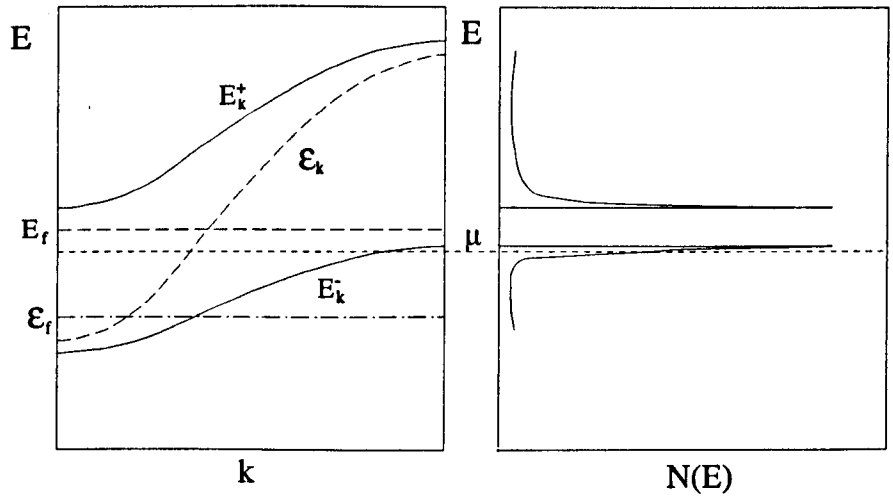

Figure 3.4: Sketch showing the renormalised band structure and density of states for a heavy fermion compound, employing the mean field solution of the periodic Anderson model. Without interactions, one has a broad conduction band ε_k and an f-level at ε_f. Interactions produce a quasiparticle band near E_f and hybridisation produces the two bands E_k^+ and E_k^-.

In the absence of any many body effects, the conduction electrons form a broad s-p-d band and the f-level is located at ε_f, below the chemical potential (see figure 3.4). When a finite hybridisation is turned on, the f-electrons and conduction electrons produce a hybrid band that remains centred at ε_f. Alternatively if there is no hybridisation but a finite Coulomb repulsion, a level is formed either side of the chemical potential, similar to the molecular model. When both effects act together the f-levels are renormalised to a new position, E_f, slightly above μ.

$$E_f = \mu + k_B T^* \tag{3.22}$$

Then, when the hybridisation is accounted for, they form two renormalised quasiparticle bands E_k^+ and E_K^-. Due to the extra f-electrons, the quasiparticle Fermi surface is lowered to k_F, where it lies on the lower flat band. In this way the enhanced density of states is predicted. The characteristic

temperature is given by

$$kT^* = \mu \exp\left(-\frac{|\epsilon_f|}{2N(\epsilon_F)V^2}\right) \tag{3.23}$$

and plays a similar rôle to the characteristic temperature in the molecular model. One expects to see the heavy fermion state forming for $T < T^*$.

3.1.6 Density functional theory for heavy fermions.

Density Functional Theory (DFT) has proved one of the most useful tools in the calculation of metallic band structure. It has enjoyed modest success in predicting the band structure of heavy fermion compounds, but it consistently underestimates the, strongly renormalised, quasiparticle effective masses.

Perhaps the earliest attempt to account for the collective charge in many body systems was that of Hartree. In this scheme the electron wavefunctions are calculated from the Schrödinger equation using a trial potential mimicking the effects of all the other electrons. Using the new wavefunctions it is possible to calculate a better guess to the trial potential. One continues this process, solving the problem, self consistently. The Hartree approximation was rather good at predicting the gross features but, due to the averaging performed, it failed to predict some of the properties produced by particular microscopic arrangements of electrons.

The Hartree scheme does regard electrons as fermions, by ensuring that there is only one per quantum state, however it does not guarantee the more fundamental definition that the wavefunction must be antisymmetric. By ensuring that the solutions produced are Slater determinants, one arrives at the Hartree-Fock formalism. One system which may be solved analytically is a free electron gas, with a constant background potential, (Jellium). In this case the average energy of each electron is increased by a quantity, called the exchange energy, $\langle \varepsilon^{exchange} \rangle = -\frac{3}{4}\frac{e^2 k_f}{\pi}$. Slater suggested that in more complicated systems one can allow for the exchange energy by adding a local energy proportional to $\langle \varepsilon^{exchange} \rangle$, with k_f evaluated at the local density. In this manner one approximates the effects of exchange by introducing a *potential* that acts in a way similar to the density dependence of the exchange term in the free electron energy density. One of the consequences is a volume, the exchange hole, surrounding each electron in which electrons of the same spin are excluded.

Density Functional theory follows a similar path, but is simpler by avoiding reference to the wavefunction, and instead only deals with the electron density. The earliest attempt at this was made by Thomas [21] and Fermi [22], although there were inaccuracies involved in their treatment of kinetic energy. The current formalism was provided by Hohenberg, Kohn and Sham [23, 24]. They showed analytically that the ground state energy of a many body system can be given precisely as a functional of electron density.

$$E[\rho, V] = \int d^3r V(\mathbf{r})\rho(\mathbf{r}) + F[\rho] \tag{3.24}$$

$F[\rho]$ is a functional of just the density, that accounts for the Coulomb repulsion, kinetic energy, exchange and correlation energy of the system.

$$F[\rho] = \frac{e^2}{2}\int d^3r d^3r' \frac{\rho(\mathbf{r})\rho(\mathbf{r}')}{|\mathbf{r}-\mathbf{r}'|} + T_0[\rho] + E_{xc}[\rho] \tag{3.25}$$

Equations 3.24 and 3.25 are exact but the actual form of E_{xc} is unknown. In the Local Density Approximation, (LDA), the exchange and correlation energy $\varepsilon_{xc}(\rho(\mathbf{r}))$ per electron of a homogeneous gas of density ρ is employed.

$$E_{xc}[\rho] = \int d^3r \rho(\mathbf{r}) \varepsilon_{xc}(\rho(\mathbf{r})) \tag{3.26}$$

So we see in this approximation that the exact electron density depletion around a particular electron is replaced by that of a homogeneous electron gas of density $\rho(\mathbf{r})$. This might not seem a particularly good approximation in such an inhomogeneous system as a metal, however only the spherically symmetric part of the exchange-correlation hole enters into the calculation of E_{xc} and so only this part need be well approximated. We do still require that the density varies slowly in space $k_F^{-1} \left|\frac{\nabla\rho}{\rho}\right| \ll 1$.

There are a number of reasons why this approach is not wholly successful with heavy fermions. Firstly they are strongly inhomogeneous systems, unlikely to be well approximated by Jellium. More importantly however, DFT is a ground state theory and has no provision for the appearance of new energy scales.

An attempt has been made to overcome these problems by adding on extra ingredients to describe the heavy fermion properties. The renormalised band method [25] attempts to merge ab initio band structure calculations and phenomenological considerations in the spirit of Landau. The principle idea is to account for the correlations by introducing a small number of phenomenological parameters which are determined by fitting to experiments. In the case of heavy fermion systems one adjusts to a single parameter, the quasiparticle effective mass obtained from specific heat experiments (γ). The f-band is then rescaled to produce the new band structure. The theory has met with some success, most notably in comparison with dHvA on $CeRu_2Si_2$ [26]. However, one must question whether it is more than just the sum of its parts – Density functional theory has been quite successful in predicting the Fermi surface features and scaling by γ will inevitably improve estimates of effective mass. A counter to this criticism is that the theory predicts the diversity of effective masses associated with different bands. It also demonstrates that the Fermi surface shape is generally not a function of electron-electron interactions.

Another consequence of the renormalised band method, is that the specific heat comes entirely from heavy quasiparticles, i.e. there are no other excitations present. It is possible to test this hypothesis by comparing an average of the effective mass determined by dHvA with γ. This view is in contrast to that of Kagan *et al.* [27] who hypothesise neutral spin excitations (spinons) that will contribute to the specific heat but not the dHvA effect. On the evidence of CeB_6, $CeRu_2Si_2$, and UPt_3, if they exist, spinons contribute only a minor effect.

Chapter 4

Quantum Oscillations.

4.1 History.

The idea of quantum oscillations was originally proposed by Landau in 1930. In the previous three years, the recently discovered, Fermi-Dirac statistics had successfully described the anomalously low specific heat in metals and the Wiedemann-Franz law. Landau's intention was to use the same means to understand diamagnetism in metals.

He predicted a contribution, now known as Landau diamagnetism, equal to one third of the paramagnetic electronic susceptibility. This contribution could be enhanced if the lattice field is taken into account, as is the case for bismuth. Also included in the paper, almost as a passing comment, was the fact that, at high magnetic fields and low temperatures there would be a *no longer linear dependence of magnetic moment on* H, *which would have a very strong periodicity in field.* He considered the oscillations unobservable on the advice of Kapitza. However, the effect was seen within two months of Landau's paper by de Haas and van Alphen who studied a single crystal of bismuth, earning it the name, the de Haas-van Alphen effect (dHvA). It is noteworthy that the initial motivation behind the experiment was to see whether there was a correlation between field dependent susceptibility and magnetoresistance, not to look for the effect predicted by Landau. Indeed they quote Landau's paper without making reference to this prediction. In the following years, due chiefly to the work of Shoenberg and Landau, the connection between theory and experiment became more apparent, as did the realisation that the effect could provide information about the Fermi surfaces of a large number of metals.

Other experiments have shown oscillations in resistance (Shubnikov-de Haas effect [28]), volume (oscillatory magnetostriction [29]), temperature, specific heat [30] and both the velocity [31] and attenuation of sound.

4.1.1 The response of a metal to a magnetic field.

As a preliminary to discussing the dHvA effect it is worth considering the various sources of magnetisation in a solid. The electrons can produce a magnetic field via their charge (by moving coherently) and via their inherent magnetic moment (by aligning).

It is conventional to divide the system up into ionic cores surrounded by a sea of conduction electrons. If the ions possess no net spin they respond diamagnetically to an external field ($\chi \approx -10^{-5}$) by changes in electron orbit. Alternatively if the ions have a magnetic moment there is also a far stronger paramagnetic contribution ($\chi \approx 10^{-3}$ at room temperature).

The conduction electrons also show a (Pauli) paramagnetism which is somewhat reduced due to the exclusion principle ($\chi \approx 10^{-5}$). Finally there is the (Landau) diamagnetic contribution of the conduction electrons ($\chi \approx 10^{-5}$), which is what concerns us here. The presence of interactions produces a host of other magnetic states, the most familiar being ferromagnetism.

This is clearly a very complicated system so it is helpful to begin by considering an idealisation – The free electron gas.

4.1.2 The response of a free electron gas to a magnetic field.

The simplest (and historically the first) description of the dHvA effect is for the free electron gas. Here we picture the electrons not interacting, yet still capable of reaching thermodynamic equilibrium. This is a highly idealised description but it is worth discussing because it provides an intuition of how dHvA works.

Quantum oscillations arise from a quantisation condition akin to that existing in the hydrogen atom. As a magnetic field is applied, the electrons circulate on helices. If one assumes that the orbits in a magnetic field are quantised by the Bohr-Sommerfeld relation

$$\oint \mathbf{p} d\mathbf{q} = (n+\gamma)2\pi\hbar \tag{4.1}$$

where

$$\mathbf{p} = \hbar\mathbf{k} + e\mathbf{A} \tag{4.2}$$

the uniqueness of solutions requires flux quantisation.

$$\Phi_n = (n+\gamma)\frac{2\pi\hbar}{e} = (n+\gamma)2\Phi_0 \tag{4.3}$$

This is identical to flux quantisation in a superconducting ring (because we are considering a perfect conductor) except that here the flux quantum, $\Phi_0 = \frac{h}{2e} = 2.0678 \times 10^{-15}$ Wb, is multiplied by 2 because single electrons are participating.

As flux is quantised, for any particular magnetic field there will be a series of orbits whose areas are given by the condition

$$A_n = \frac{\Phi_n}{B} \tag{4.4}$$

The areas of orbits in momentum space are therefore given by

$$S_n = A_n \left(\frac{eB}{\hbar}\right)^2 = \Phi_n \left(\frac{e}{\hbar}\right)^2 B \tag{4.5}$$

where S_n is the area in **k** space, and A_n is the area in real space. These tubes, separated by an energy $\hbar\omega_c$ are the so called Landau levels and are shown in a celebrated representation due to Chambers.

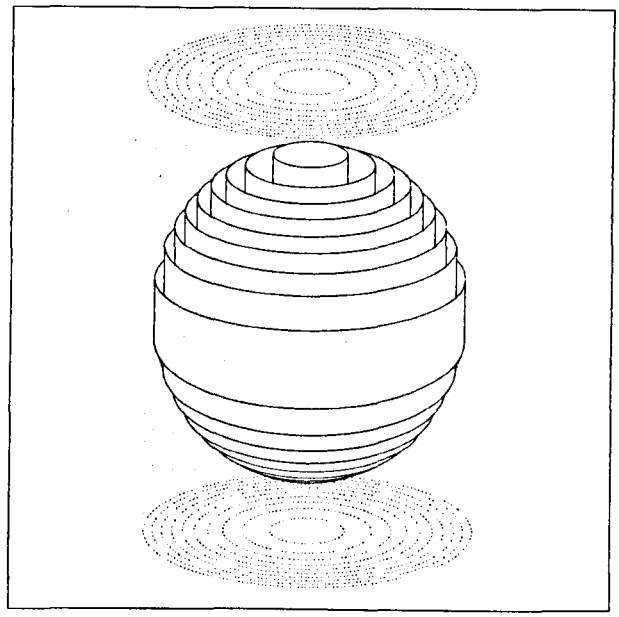

Figure 4.1: Landau levels for a free electron gas in the presence of a magnetic field. For clarity only a few levels are shown, as is the case for low electron density. For noble metals there will be about 10,000 levels below the Fermi energy, at a field of 5T.

The sphere depicts the Fermi surface of the electron gas, which in the absence of a magnetic field, is filled uniformly with electrons with a density of $(L/2\pi)^3$, where L is the size of the system. The Landau levels are highly degenerate. On each one there are as many states as, in zero field, would lie within $\pm\hbar\omega_c/2$ of the level. As the field increases they expand in k space, eventually passing through the Fermi surface where they are depopulated as the system reaches thermal equilibrium. This does not have a pronounced effect on the free energy of the system, Ω, (because other Landau levels are expanding from below) except at a so called extremal area, (in this case the equator of the Fermi sphere) where there is a discontinuous drop in the average Landau tube area, naturally leading to a decrease in Ω.

4.1.3 The semiclassical description.

The semiclassical approximation attempts to account for the presence of the periodic array of ions, and is invoked for the case where the spread of electron wavepackets can be considered large compared to the lattice constant but small compared to the wavelengths of applied fields. The motion of an electron in this regime is given by

$$\dot{\mathbf{r}} = \mathbf{v}(\mathbf{k}) = \frac{1}{\hbar}\frac{\partial \varepsilon(\mathbf{k})}{\partial \mathbf{k}} \tag{4.6}$$

and

$$\hbar\dot{\mathbf{k}} = (-e)\mathbf{v}(\mathbf{k}) \times \mathbf{H} \tag{4.7}$$

For simplicity, considering the case where the field is in the z direction, it is clear that it can do no work on $\mathbf{k_z}$, hence this is a constant of motion. The other constant of motion is the electron energy $\varepsilon(k)$. Therefore, the electron orbits are the intersection of these two surfaces.

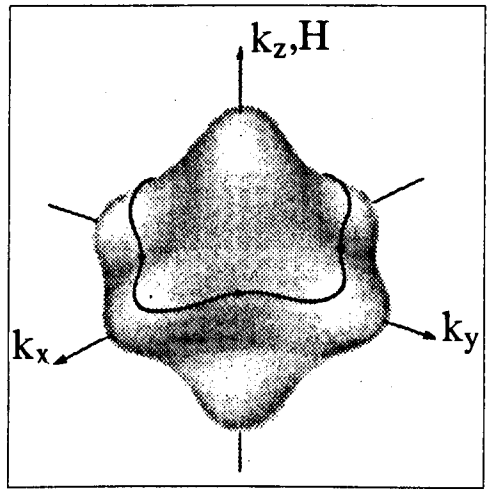

Figure 4.2: An example of a semiclassical orbit. The arrow indicates the direction of motion for an electron (as opposed to hole) Fermi surface. From Ashcroft and Mermin [32].

The electron orbits in real space are given by

$$\mathbf{r}_\perp(r) - \mathbf{r}_\perp(0) = -\frac{\hbar}{e\hat{\mathbf{H}}} \times (\mathbf{k}(t) - \mathbf{k}(0)) \tag{4.8}$$

It is a remarkable feature of the magnetic field that it causes an image of what is essentially an abstract construct, the Fermi surface, to be mapped out in real space. We thus see that even for complicated Fermi surface shapes, the dHvA effect acts as a caliper for extremal areas, where one must now adopt the more general definition, that these are places where $\left|\frac{\partial A_i}{\partial k_z}\right| = 0$.

4.2 The Lifshitz Kosevich equation.

To calculate quantitative changes in magnetisation it is helpful to start with the free energy, Ω, of the system, and use the relation $\mathbf{M} = -(\nabla_H \Omega)_{T,V,\mu}$. A semiclassical equation for the oscillatory variation of the free energy was provided by Lifshitz and Kosevich [33].

$$\tilde{\Omega} = \left(\frac{e}{2\pi\hbar}\right)^{\frac{3}{2}} \frac{e\hbar H^{\frac{5}{2}}}{m^*\pi^2} \left|\frac{\partial^2 A_i}{\partial k_z^2}\right|^{-\frac{1}{2}} \sum_{r=1}^{\infty} r^{-\frac{5}{2}} R_T R_\sigma R_D \cos\left[2\pi r\left(\frac{F_i}{H} - \gamma\right) \pm \frac{\pi}{4}\right] \tag{4.9}$$

giving a magnetisation of

$$\widetilde{M} = -\left(\frac{e}{2\pi\hbar}\right)^{\frac{3}{2}} \frac{2Fe\hbar H^{\frac{1}{2}}}{m^*\pi} \left|\frac{\partial^2 A_i}{\partial k_z^2}\right|^{-\frac{1}{2}} \sum_{r=1}^{\infty} r^{-\frac{3}{2}} R_T R_\sigma R_D \sin\left[2\pi r\left(\frac{F_i}{H} - \gamma\right) \pm \frac{\pi}{4}\right] \tag{4.10}$$

where r is the harmonic index and $\left|\frac{\partial^2 A_i}{\partial k_i^2}\right|$ allows for the curvature of the Fermi surface (A cylindrical Fermi surface will have a *wider* extremal area than a lenticular one). The other terms are presented individually.

The dHvA frequency.

$$F_i(\theta,\phi) = \frac{\hbar A_i(\theta,\phi)}{2\pi e} \tag{4.11}$$

This term, which is the frequency of the dHvA oscillations with respect to $1/B$, provides A_i, the extremal orbit area. The coefficients θ and ϕ denote the crystal orientation relative to the field and by varying them, one can map out the three dimensional Fermi surface. The subscript i indicates that in most metals there are multiple sheets of Fermi surface.

In noble metals the so called belly orbits have an area of 5×10^{20} m^{-2} and consequently dHvA frequencies of $\approx$ 50 kT. Heavy fermions with their complicated chemistry have larger Brillouin zones and consequently lower frequencies. The physical meaning of the dHvA frequency (F) in terms of an actual magnetic field, is that at this field the lowest lying Landau level leaves the Fermi surface, the so called quantum limit. This effect has been observed in small sheets of Fermi surface for certain metals (e.g. bismuth) and is an area of current research in semiconductors.

R_D, R_T and R_S are damping terms that arise when the idealised equation is extended to more realistic situations. They will be considered individually as they can yield important information about a material.

Thermal broadening.

$$R_T = \frac{rX}{\sinh(rX)} \tag{4.12}$$

where

$$X = 2\pi^2 k_B T/\hbar\omega_c = 14.693\frac{T}{H}\left(\frac{m_T^*}{m_e}\right) \tag{4.13}$$

and

$$\omega_c = eH/m_T^* \tag{4.14}$$

This term arises because the experiment is performed at a finite temperature. Thermal fluctuations create electron-hole pairs that effectively smear out the Fermi surface making the depopulation of Landau levels less instantaneous. The effect is more pronounced, the larger the number of electrons affected, so it is strongly dependent upon the density of states at the Fermi surface, or the quasiparticle effective mass, m_T^*. The unusual form of the equation arises from the Fourier transform of the derivative of the Fermi-Dirac function.

A few things can be noted from figure 4.3. In order for the oscillations not to be totally damped in heavy fermions, one must operate in the thermally pacific conditions of millikelvin temperatures.

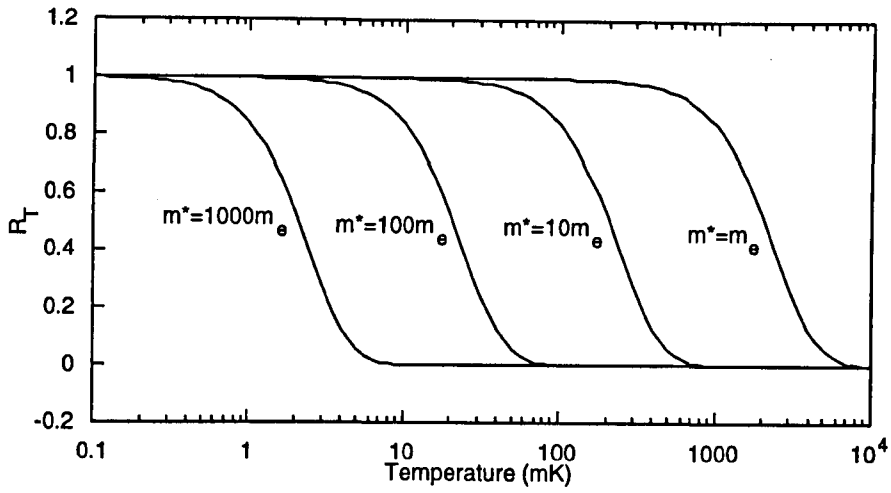

Figure 4.3: The thermal reduction factor for quasiparticles of different effective masses, in a field of 14 T.

Although this temperature dependence is primarily a problem, it can be used to advantage, because it provides a measure of quasiparticle effective mass. One conducts a series of experiments at a range of temperatures, and then fits the amplitudes to equation 4.3. The reason that the curve saturates at low enough (but finite) temperatures is because, even though there will still be some Fermi surface blurring, it becomes less than the Landau level spacing $\hbar\omega_c$. This is also the origin of this term's field dependence.

The Dingle term.

$$R_D = \exp\left(-\frac{r\pi}{\omega_c^*\tau^*}\right) = \exp\left(-\frac{2\pi^2 r k_B m_D^* T_D}{e\hbar H}\right) = \exp\left(-14.693 r \frac{m_D^* T_D}{m_e H}\right) \qquad (4.15)$$

This term, that accounts for scattering with non magnetic impurities and crystal inhomogeneity, was not part of the original L.K. formulation and was introduced by Dingle [34] in 1952. The effect of scattering is to broaden the Landau levels with $\Gamma = \hbar/2\tau$ the Lorentzian half-width. An intuitive interpretation is that it represents the reduction in wave amplitude of an electron which has completed r circuits of a cyclotron orbit. The alternative representation expressed as a function of a temperature, (the Dingle temperature, T_D) is of historical origin - Early investigations found that experimental results fitted the *original* L.K. formula if the temperature was assumed to be a constant, T_D, higher. Comparison of equations 4.12 and 4.15 show that in the limit $\sinh x \longrightarrow e^x/2$, the equations have the same form, if the assignment $T_D = \frac{\hbar}{2\pi k\tau}$ is made. The field variation is shown in figure 4.4.

Once more it is apparent that heavy fermions present problems, this time because of their generally imperfect sample quality (It is difficult to purify the rare earths because they are chemically so similar). The purity of a sample can be ascertained by producing a so called Dingle plot, whereby plotting $\ln(AR_T)$, (A being the dHvA amplitude) versus 1/H, one may determine the value of $m_D^* T_D$ from the gradient.

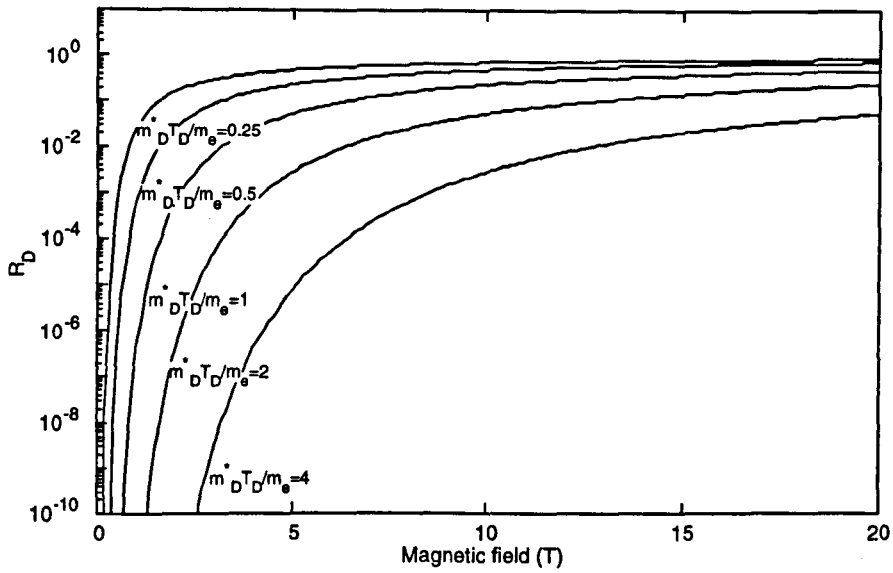

Figure 4.4: The Dingle reduction term for a variety of $m^*_D T_D/m_e$. The y-axis is logarithmic and, contrary to appearance, the function is still rising steeply over the high field region.

Spin splitting.

The final damping term arises from the Zeeman splitting of the electron energies due to their inherent spins. The spin will shift the energy of an electron, by the purely dipolar interaction $-\boldsymbol{\mu} \cdot \mathbf{B}$. In terms of the dHvA oscillations this can be viewed as a phase shift, hence there is a separate contribution from the up (parallel) electrons and the down (antiparallel) electrons.

$$D(H,T) = A_\uparrow(H,T)\sin(\phi_\uparrow(H)) + A_\downarrow(H,T)\sin(\phi_\downarrow(H)) \tag{4.16}$$

where

$$\phi_\sigma(H) = \frac{2\pi F_\sigma(H)}{H} + \xi_\sigma(H) + \xi_0 \tag{4.17}$$

In the original L-K formula, the energy splitting is assumed linear with field, $\xi_\sigma H$, which cancels with the inverse field frequency dependence to produce field independent phase factors given by

$$\xi_\uparrow = -\frac{\pi r m^*_\uparrow g_\uparrow}{2m_0} \tag{4.18}$$

and

$$\xi_\downarrow = \frac{\pi r m^*_\downarrow g_\downarrow}{2m_0} \tag{4.19}$$

If the amplitude , frequency, effective mass and g factor are assumed to be spin independent then one can employ the well known trigonometric equation, $\sin A + \sin B = 2\sin\frac{1}{2}(A+B)\cos\frac{1}{2}(A-B)$, giving

$$D(H,T) = 2A(H,T)\sin\left(\frac{2\pi F(H)}{H} + \xi_0\right)\cos\left(\frac{\pi r m^* g}{2m_0}\right) \tag{4.20}$$

Hence the additional R_σ term in the L-K equation.

When these quantities are not assumed to be spin independent more complicated situations can arise, as are discussed later with reference to $CeCu_2Si_2$.

4.2.1 The extended Lifshitz Kosevich equation.

The original L.K. equation was derived for non-interacting particles. Shoenberg [35] reviews some of the early attempts to include interactions. Many body interactions are often modelled as producing a complex self energy given by $\Sigma = \Delta(\zeta) + i\Gamma(\zeta)$ where $\zeta = \epsilon - \mu$, and μ is the chemical potential. In this picture the energies of the non-interacting states are shifted by $\Delta(\zeta)$ and broadened by $\Gamma(\zeta)$. It is seen that if $\Delta(\zeta)$ varies linearly with ζ and $\Gamma(\zeta)$ is negligible, then the form of the L.K. equation can be retained but with the band mass renormalised by $(1 + \lambda)$, where λ characterises the strength of the interactions.

Luttinger was the first to consider the effects of electron-electron interactions perturbatively [36] and discovered that the above conditions were approximately satisfied although $\lambda_{e.e}$ was small and $\Delta(0)$ is not identically zero, producing a small, k dependent, shift in dHvA frequencies. A striking result of the study was that these effects leave the volume of the Fermi surface unchanged.

The electron-phonon interaction was considered by Wilkins and Woo and again it was found that the band mass must be multiplied by a $(1 + \lambda_{e.p})$ term. Here $\Delta(\zeta) \approx 0$ so the dHvA frequencies are identical to the free electron case. The theory however predicts an unobserved temperature dependence of the Dingle temperature T_D. An explanation of this came from Fowler and Prange [37] and later Englesberg and Simpson [38] applying a full many body treatment. This approach, although lacking a simple interpretation predicts that the only effect of the e-p interaction will be a renormalised mass.

For heavy fermion compounds, the perturbative approach is no longer appropriate. i.e. the forces between electrons are unlikely to be accurately described by a power series in their interaction strength. Wasserman and Springford [39] have employed the mean field approach, starting with the periodic Anderson Hamiltonian. In this case, the oscillatory free energy is given by

$$\tilde{\Omega} = \frac{-2(eH)^{5/2}}{4\pi^4 m_T^*} \sum_r \frac{(-1)^r}{r^{5/2}} R_D^{HF} R_T^{HF} \cos\left(\frac{2\pi r(\mu + 2Dn_f/N)}{\omega_c} - g\frac{m_S^*}{m_0}\pi r J\left(1 + \frac{2Dn_f}{NT^*}\right) - \frac{\pi}{4}\right) \quad (4.21)$$

Once more, a conspicuous feature is the similarity to the original L.K. equation. The Dingle term has superficially the same form as before, as does the thermal term, if one substitutes a new effective mass m_T^*. Throughout this chapter, masses have been labelled independently, in anticipation of this result.

$$m_{HF} = m^*\left(1 + \frac{2Dn_f T^*}{N(T^* - Jh)^2}\right) \quad (4.22)$$

where h is the reduced field $h = g\mu_B H$. For weaker fields, $Jh \ll T^*$ this simplifies to

$$m_{HF} = m^*\left(1 + \frac{2Dn_f}{NT^*}\right) \quad (4.23)$$

This is the same as the enhancement predicted for the susceptibility and specific heat in heavy fermion systems, by the mean field approximation.

In general, the heavy fermion Dingle effective mass will be different from both the free electron effective mass and the thermodynamic effective mass. Thus, there is no longer a natural definition of the Dingle temperature, T_D, or the quasiparticle lifetime, τ^*. However, one can define the quasiparticle mean free path $\delta^* = v_k^* \tau^*$, where the Fermi velocity is assumed isotropic and given by $v_k^* = \frac{\hbar k_F}{m_D^*}$, where k_F is the Fermi momentum. One obtains

$$R_D^{HF} = \exp\left(-\frac{r\pi\hbar k_F}{He\delta^*}\right) \tag{4.24}$$

Of these values, k_F is unknown, so if one assumes a circular orbit one can use $\pi k_F^2 = \frac{2\pi eF}{\hbar}$, giving,

$$R_D^{HF} = \exp\left(-\left(\frac{2\pi^2\hbar^3}{e}\right)^{\frac{1}{2}} \frac{rF^{\frac{1}{2}}}{H\delta^*}\right) = \exp\left(-1.202 \times 10^{-41} \frac{rF^{\frac{1}{2}}}{H\delta^*}\right) \tag{4.25}$$

4.3 The field modulation technique.

A variety of methods have been applied to measure dHvA oscillations, the main requirement being that the field experienced by the sample is homogeneous compared to the period of dHvA oscillations. Two of the techniques which are still used are the pulsed field technique (which lends itself to high field experiments with resistive coils) and the field modulation technique, which is the topic of this study.

The field modulation technique was developed in 1964 [40] and is currently almost universally used for experiments employing superconducting magnets. The principle is that a large field H_0 (provided by the superconducting magnet) is linearly ramped at a very slow rate whilst a small oscillating field h_0 at a frequency ω is superimposed upon it. One then looks for the magnetic response of the sample at ω or any harmonic of it. In short, H_0 provides the quantisation condition and h_0 provides the dH/dt required to perform the measurement. It is thus possible to have very slow sweeps to reduce noise and still have an appreciable dH/dt. A further advantage of this technique, is that it is rather resilient to external vibrations being confused for dHvA oscillations, because it would require them to be modulating the reference frequency and then have the correct $1/B$ field dependence. It is necessary to consider the effect of this type of measurement on the resulting signal amplitude.

In the presence of a varying magnetic field the response of a metal is given by

$$\frac{dM}{dt} = \frac{dM}{dH}\frac{dH}{dt} \tag{4.26}$$

In the case of the field modulation technique, the applied field is

$$H = H_0 + h_0 \cos\omega t \tag{4.27}$$

so,

$$\frac{dH}{dt} = -h_0\omega \sin\omega t \tag{4.28}$$

The $\frac{dM}{dH}$ term is expanded as a Taylor series.

$$v = -cVh_0\omega \sin\omega t \left\{ \frac{dM}{dH} + \frac{d^2M}{dH^2} h_0 \cos\omega t + \cdots \frac{d^kM}{dH^k} \frac{h_0^{k-1}}{(k-1)!} (\cos\omega t)^{k-1} + \cdots \right\} \tag{4.29}$$

where v is the voltage generated in a pickup coil, V is the sample volume and c is a suitable coupling constant $c = v/\dot{m}$. Using double angle (and higher order) relations we can see the signal present at each harmonic

$$v = -cV\omega \left\{ h_0 \frac{dM}{dH} \sin\omega t + \frac{1}{2} h_0^2 \frac{d^2M}{dH^2} \sin 2\omega t \cdots + \frac{h_0^k}{2^{k-1}(k-1)!} \frac{d^kM}{dH^k} \sin k\omega t + \cdots \right\} \tag{4.30}$$

When the specific oscillatory nature of the magnetisation is substituted in for $\frac{dM}{dH}$, further manipulations furnish the equation

$$v = -2cV\omega A \sum_{k=1}^{\infty} k J_k(\lambda) \sin\left(\frac{2\pi F}{H} + \phi - \frac{k\pi}{2} \right) \sin k\omega t \tag{4.31}$$

where

$$\lambda = \frac{2\pi h_0}{\Delta H} \equiv \frac{2\pi F h_0}{H^2} \tag{4.32}$$

and $J_k(\lambda)$ are Bessel functions of the first kind, as in figure 4.5.

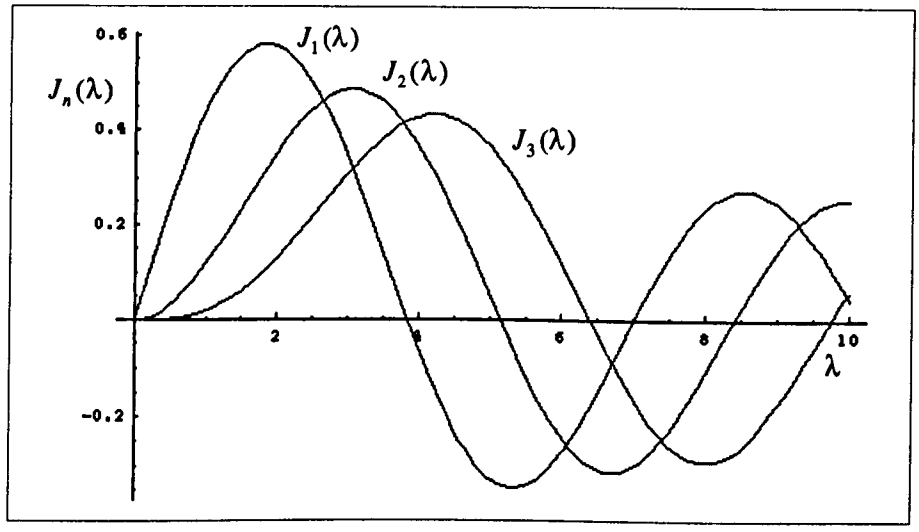

Figure 4.5: The first three Bessel functions. Note, for small λ, $J_n(\lambda) \approx \frac{1}{n!}\frac{\lambda^n}{2}$. The maxima are $J_1(1.841) = 0.582$ and $J_2(3.054) = 0.486$.

This can be qualitatively understood for the first harmonic by considering figure 4.6. The result is that, by tailoring the modulation amplitude, one can highlight particular frequencies. Another noteworthy result is that one can look at a higher harmonic (typically the second) in order to remove the, largely linear, background magnetisation. Neither of these methods are in fact possible in the experimental setup discussed in this thesis, because the prime factor is that the modulation amplitude must be small, for reasons of heating. For the experiments described in this thesis $\lambda \approx 0.01$. In this λ regime the first harmonic varies linearly and the second harmonic varies quadratically so there is more than a hundredfold gain in signal looking at the first harmonic. Consequently experiments here were only conducted looking at the first harmonic, with the result that background changes in magnetisation made a significant contribution to the signal.

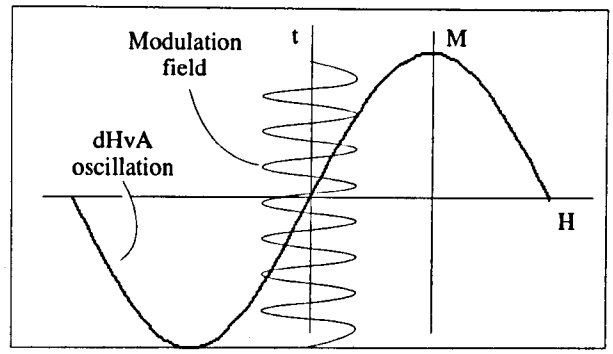

Figure 4.6: Schematic showing the modulation field and the dHvA. Considering the first harmonic, for low modulation amplitudes the modulation samples an almost linear magnetisation so the signal scales accordingly. As the modulation is increased this begins to tail off, until the modulation amplitude is the same as the dHvA period. This case considers the maximum dM/dt but a similar explanation can be given for arbitrary values.

4.4 The purpose of dHvA experiments in heavy fermions.

It has already been mentioned in chapter 3 how important good dHvA data has been in assessing theories. What makes it a particularly stringent filter is the ability to provide detailed pictures of, not just the Fermi surface, but the properties of excitations at each point on it. Furthermore, it is clear that there is a great need to study as many of the heavy fermion compounds as possible. Only then will we know that the same mechanisms are at the root of the strong renormalisation in each of these alloys.

These are among the present motivations for studying $CeCu_2Si_2$. Although its stoichiometry makes this a less than trivial operation, so much effort has been expended in characterising it by other methods and it displays such a wide variety of interesting properties that it has become one of the key heavy fermions for dHvA experiments.

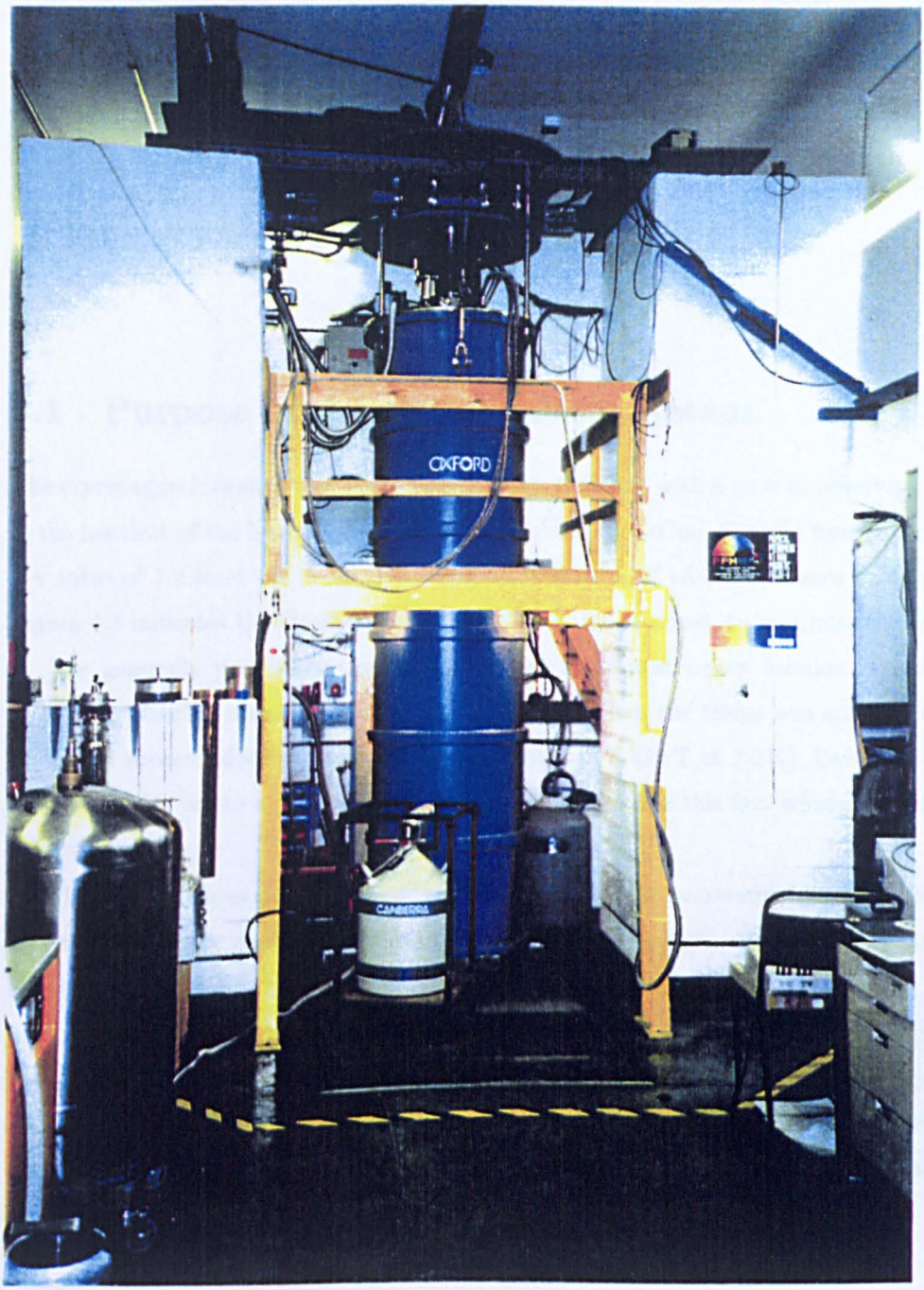

Plate 1. 1mK/17T Cryomagnetic System.

Chapter 5

The cryomagnetic system.

5.1 Purpose of the cryomagnetic system.

The cryomagnetic system (see previous page) was designed with a view to observing dHvA oscillations in the heaviest of the heavy fermion compounds, such as $CeCu_6$. Specific heat experiments have given a γ value of $1.6\,Jmol^{-1}K^{-2}$ for this material, indicative of effective masses upwards of 500 m_e [41]. Figure 4.3 indicates that temperatures under 5 mK are required, to minimise thermal damping.

The generally poor mean free paths present in current heavy fermion crystals mean that the maximum possible magnetic field is also desirable. When the fridge was commissioned, the state of the art in superconducting magnets could produce 17 T (19 T at 2.2 K). Low temperatures and high magnetic fields are to a certain extent incompatible and it is this fact which has dictated the scale of this project.

The most obvious problem is eddy current heating due to relative motion between the magnets and any electrically conducting parts of the fridge or the sample. This has led to an intricate system of vibration isolation. A secondary concern is that the field modulation technique (which inevitably involves an oscillating magnetic field) must also not introduce eddy current heating. Accordingly, low modulation fields are used and hence a very sensitive detection system is required. This takes the form of a SQUID (which can be crudely thought of as a current to voltage converter with a gain of 7×10^6 V/A). The great sensitivity of this device is another reason why vibration isolation is so important.

5.2 Description of the system.

The refrigerator is shown schematically in figure 5.2. Cooling is achieved by the traditional combination of a dilution refrigerator coupled to a nuclear demagnetisation stage. The dilution unit is an Oxford Instruments 'special sliding insert refrigerator system'. The demagnetisation stage and thermometry were installed by other group members (Hill, Meeson and Probst) [42]. A previous r.f.

SQUID susceptometer had been installed on the fridge by Hill, Janssen and Meeson [42] but was not found to work reliably (mainly due to the SQUID electronics). The current d.c. SQUID susceptometer was installed by the author as part of the Ph.D. project.

5.2.1 Vibration isolation.

In an effort to reduce any vibrations in the system, the precautions shown in figure 5.1 are employed.

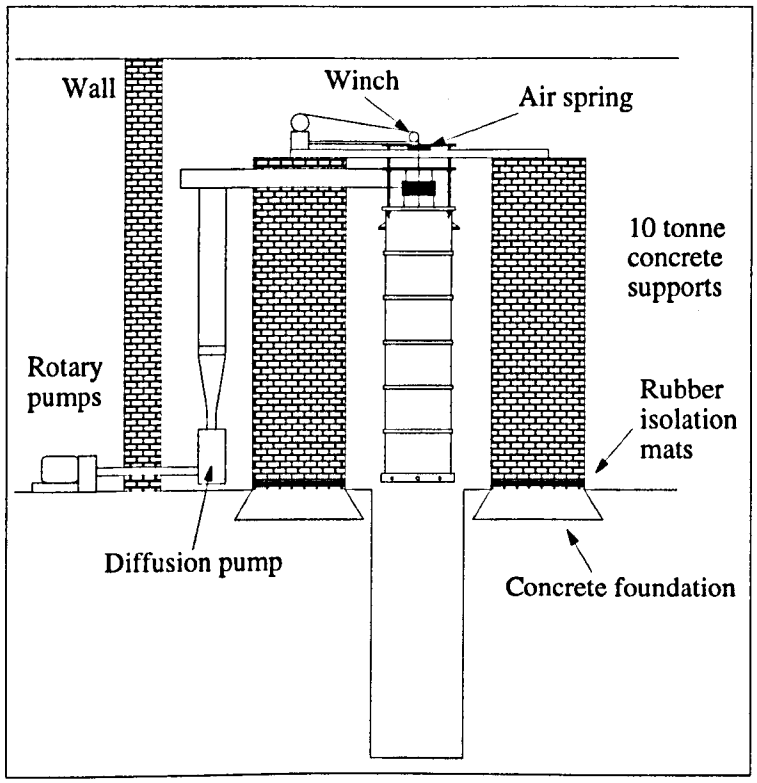

Figure 5.1: The vibration isolation.

The cryostat is located in a laboratory adjacent to a busy corridor, so ground vibrations were a prominent concern. The fridge support structure is decoupled by having its foundations built directly into the local Redland sandstone bedrock. A pair of ten tonne pillars are further isolated from the ground by rubber isolation mats. The cryostat and Dewar are suspended from a crossbeam by means of an airspring. All the rotary pumps are housed in another room, having their pumping lines firmly cemented into the wall. Finally all pumping lines are cemented into one of the pillars.

5.2.2 The cryogenic insert.

The cryogenic insert is suspended from the Dewar top plate by 1.52 m long stainless steel pumping lines and access tubes. The dilution unit consists of four gold plated copper plates, hereafter called the 1K pot plate, the still plate, the 50 mK plate and the mixing chamber top plate. The plates are separated by thin walled stainless steel tubes. The pot has a capacity of 250 cm^3 and is equipped with two

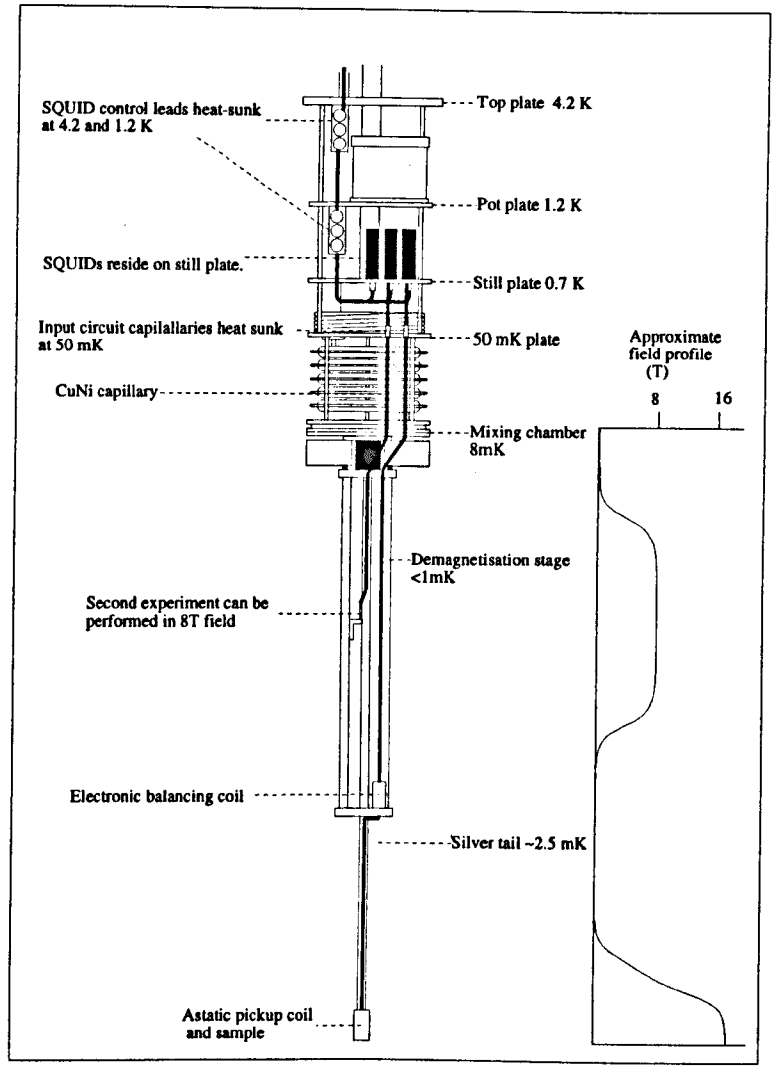

Figure 5.2: The cryostat insert. This diagram is not to scale in order to show the susceptometer adequately. In reality the demagnetisation stage is longer.

helium fill lines, should one fail. A radiation shield is suspended from the 50 mK plate, protecting the coldest parts of the dilution unit and the demagnetisation stage. The radiation shield is constructed from 0.5 mm thickness stainless steel, plated with copper to increase its thermal conductivity. Breaks in the copper were scratched along its length to avoid eddy currents. The dilution refrigerator has five quasicontinuous sintered silver heat exchangers between the 50 mK plate and the mixing chamber. Underneath the mixing chamber is a large, gold plated, copper stage allowing over forty sites for thermal connection.

Electrical connection from room temperature is made in two stages. Two sets of 18 way looms consisting of 47 swg Cu wires run from the top plate to the 1K pot plate. The heat leak to the 1K pot plate was estimated to be 2 mW per loom. From here the wiring is changed, by means of a D connector, to 42 swg Niomax CN61/05 superconducting wire, heat sunk at the still plate, the 50mK plate and the mixing chamber plate. Heat sinking is achieved by varnishing to OFHC Cu bobbins, which are screwed firmly to the appropriate plates. Twenty micro-coax leads are also run from a

vacuum tight BNC box at room temperature via a heat sink at the 4 K plate to a connector box on the 1K pot plate. The coax lines are used for capacitance measurements on ^{3}He melting curve thermometers and for the susceptometer modulation field.

5.2.3 The magnet and Dewar assembly.

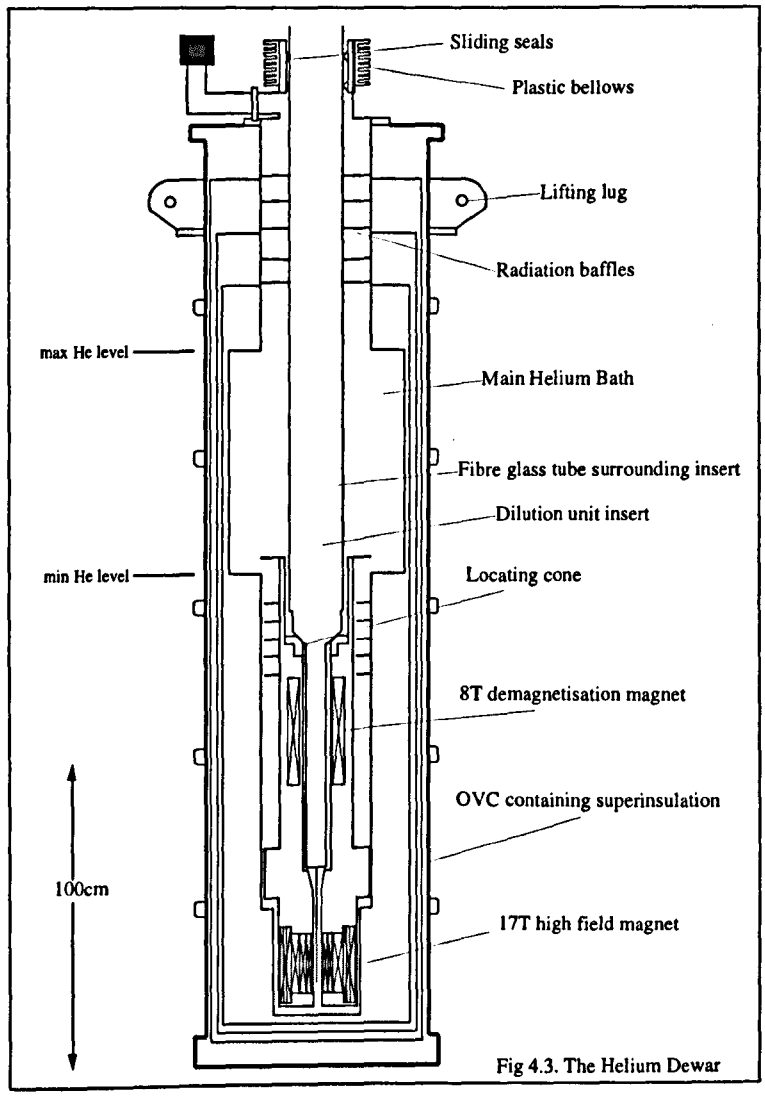

Figure 5.3: The Dewar and magnets. From Hill [42].

The Dewar (see figure 5.3) possesses a belly with a capacity of 200 l. The boil off from the bath is typically about 20 l per day, giving a hold time of 10 days, although this increases to more than 30 l per day when the magnet leads are energised. Boil off is reduced by five baffle plates along the pumping lines, which also serve to provide extra structural rigidity.

The main Dewar houses two solenoidal magnets mounted on a common axis. They are both equipped with a series of cancellation coils in order to provide a low field region for experiments, to reduce the mutual inductance between the magnets and to reduce the stray field over the mixing chamber (to avoid eddy current heating). The magnets are mounted on a support structure consisting

of a services top plate for electrical and cryogenic access, radiation baffles, a lambda point refrigerator and magnet protection circuitry.

The high field magnet consists of three sets of concentric solenoids wound on separate formers. The outer sections and the cancellation coils are made of NbTi, whilst the inner sections are made of Nb_3Sn. Both employ multifilamentary wire with a copper matrix. The demagnetisation magnet consists of a solenoid wound on a single former.

Both magnets are fitted with a superconducting heat switch, allowing the magnets to be left persisted at a finite field with no current supplied externally. Protection resistors are located in series with diodes for both magnets, restricting the development of high voltages and allowing the dissipation of energy, in the event of a quench. Some useful operating properties are summarised in table 5.1.

Magnet	Critical field T	Max. sweep rate A (T)	tesla/amp	Inductance (H)
Demagnetisation	8	4 (0.69)	0.17372	97.4
Main	17 (19 @ 2.2 K)	5 (0.86)	0.17316	84.3

Table 5.1: Properties of the superconducting magnets.

An important requirement for magnets used in a dHvA experiment is that, over the volume of the sample, the inhomogeneity of the magnetic field must be appreciably less than the period of a dHvA oscillation, otherwise an extra phase smearing term will be introduced into the LK formula. This condition will be most stringent for studying noble metals (large Brillouin zone) at low fields (inverse frequency dependence). The magnet homogeneity is 0.1 % over a 10 mm volume so for (a 1 mm sample of) silver (F= 46 kT) this would correspond to a minimum usable field of 0.6 T (if we demand that the period of the dHvA oscillation be 5 times larger than any smearing).

The current to the magnets is supplied by an Oxford Instruments [43] PS120-10 power supply. This supply can produce a maximum of 120 A at 10 V. The current is measured by monitoring the voltage across an 83.3 mΩ series resistor (the "shunt") at the output of the current source. The voltage is logged continuously, along with the dHvA signal. The slowest sweep rate permitted by the power supplies is 0.001 T/min, which is only just slow enough for these experiments. Being an LR circuit there will be a finite time constant that must be considered when converting from shunt voltage to magnetic field. This was measured by performing a dHvA experiment sweeping in alternate directions and then comparing the apparent locations of the oscillations. The material employed here was the polycrystalline silver cold finger (see figure 5.4). The spacing between any two identical features should equal $2r\tau$, where r is the sweep rate and τ is the time constant. For the main magnet τ was found to be 4.47 s.

5.2.4 The nuclear demagnetisation stage.

Demagnetisation is achieved with the 8 T magnet acting on a copper demagnetisation stage from which a silver cold finger is suspended into the high field region. The choice of metals used for these

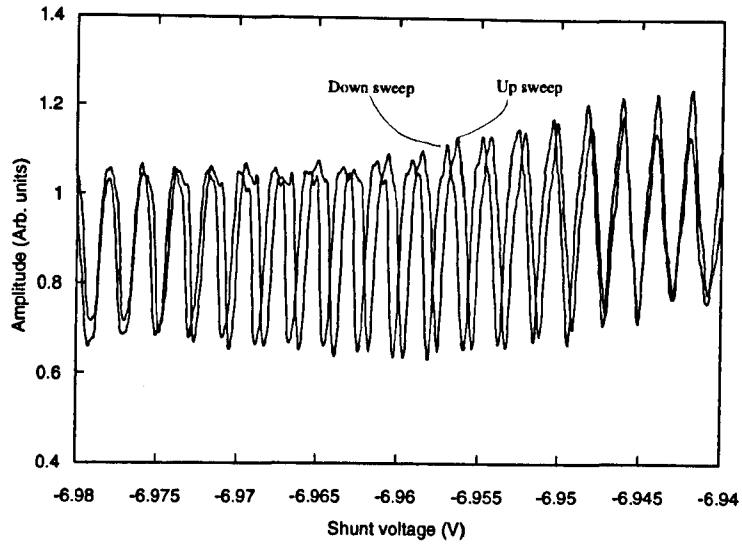

Figure 5.4: Some dIIvA oscillations from polycrystalline silver, for up and down sweeps. In each case the sweep rate was 0.02 T/min.At either end, the oscillations coincide because the sweep is brought to an end. In the middle the spacing is 2.98 $\times 10^{-3}$ T corresponding to a τ of 4.47 s.

two sections is dictated by their demagnetising abilities and also their heat capacity.

The principle requirement of a nuclear refrigerant is a large nuclear Curie constant, λ_n. This allows the nuclei to cool in the magnetic field. It is also important that the electrons then come into thermal equilibrium with the nuclei, so one also requires a small Korringa constant and good electronic thermal conductivity. Other requirements are the availability of the material, the absence of any ordering (superconducting or magnetic) and the absence of internal magnetic fields. Although many materials satisfy some of the requirements, it is copper that achieves a good compromise between them all.

The demagnetisation stage employed here is made from OFHC copper in the form of a tripod (figure 5.2). The design is intended for simplicity and speed of use. The estimated quantity of copper in the demagnetisation field is 8.2 moles. This is minute compared with many facilities, however it does allow a relatively fast precool time and achieves base temperatures adequate for these experiments. The demagnetisation stage is suspended from the mixing chamber by three vespel rods. Thermal contact is achieved by a superconducting switchable thermal link based on a design by Mueller [44], consisting of six sheets of 0.25 mm five nines pure aluminium clamped into gold plated copper with BeCu screws. The small solenoid used for switching is surrounded by a lead can with the dual purposes of shielding the aluminium sheets from any external magnetic fields and preventing the solenoid from producing stray magnetic fields. The switching ratio has been measured to be at least 1000 which is sufficient for the present purposes.

The sample is mounted on a silver cold finger that is firmly bolted to the demagnetisation stage. Silver is chosen because one requires a material with a good thermal conductivity and a minimal heat capacity. The cold finger has a cruciform cross-section to reduce the eddy currents to one hundredth that of a rod with a similar diameter. This part of the experiment is not yet perfected, however,

and the rising specific heat of silver in high fields and low temperatures is found to limit the cold finger base temperature to 2.5 mK at 17 T. A further problem is that eddy current heating is evident for sweep speeds above 0.005 T/m. No other metal lends itself to this application, and more exotic solutions, such as a miniature ^{3}He bath, are impractical. The best solution will probably be to use a small bundle of silver wires to provide the thermal conduction, and a more inert material to provide the mechanical rigidity.

The last part of the cooling stage is the sample. Large, single crystal $CeCu_2Si_2$ samples are not currently available, and indeed the sample employed in this particular study is only 3 mm $\times$1.5 mm $\times$1 mm. This is not a particular problem for dHvA measurements because larger samples require more stringent field homogeneity.

5.3 Thermometry.

5.3.1 Introduction.

The fridge possesses a variety of thermometers. These include the diagnostic resistors which aid cool-downs and are occasionally used for warmer experiments. There is a primary thermometer in the form of a ^{60}Co crystal and for the low millikelvin regime, ^{3}He melting curve thermometers.

5.3.2 Diagnostic thermometers.

Seven diagnostic thermometers are installed on the cryostat. Their location and other relevant information is included in table 5.2.

AVS channel	Location	Type	R.T. Ω	4K Ω	Base temp. Ω
1	1K pot	200 Ω Matsushita	580	906	898
2	Filmburner	200 Ω Matsushita	599	946	1291
3	Still	200 Ω Matsushita	199	461	843
4	50mK Plate	100 Ω Matsushita	110	220	1331
5	Mix Ch. 1	1 kΩ RuO_2	998	1271	12675
6	Mix Ch. 2	200 Ω Matsushita	204	405	$> 20M$
7	Demagnetisation Stage	1 kΩ RuO_2	1008	1304	7700

Table 5.2: Properties of the diagnostic resistance thermometers.

The resistances are measured by an AVS-46 resistance bridge with an excitation voltage of 30 μV to avoid Joule heating. The output is then logged on a Power Macintosh 7300/166 computer using *LabVIEW* software.

5.3.3 ^{60}Co nuclear orientation thermometry.

Nuclear orientation thermometry attempts to directly probe the Boltzmann population of the nuclear magnetic levels. It relies on the principle that, for certain modes of γ emission, the emission probability has a spatial anisotropy that differs for each of the (2I+1) levels. This is due to conservation of angular momentum. In the ^{60}Co crystal, the aligning magnetic field is provided by embedding the nuclei in a ferromagnetic ^{59}Co host.

The measurement is performed by observing with a γ ray detector along the magnetic orientation axis. At low temperatures one expects to only observe background radiation. As the temperature increases the distribution becomes more anisotropic so the count rate increases, until it saturates at around 100 mK. There is a well established theory describing these processes so it is a primary thermometer. The ^{60}Co crystal is located in the compensated field region, at the base of the demagnetisation stage. In the experiments presented here, nuclear orientation thermometry was not pursued because ^{3}He melting curve thermometry presented a simpler alternative, although it was previously used to confirm the calibration of the melting curve thermometers.

5.3.4 ^{3}He melting curve thermometry.

Although many physical processes are "frozen" out at millikelvin temperatures, ^{3}He remains liquid to the lowest temperatures measured, at atmospheric pressure. However, under application of pressure it does solidify and the purpose of the melting curve thermometer is to measure the pressure when the solid and liquid phases coexist and hence determine the temperature. The melting curve is shown in figure 5.5.

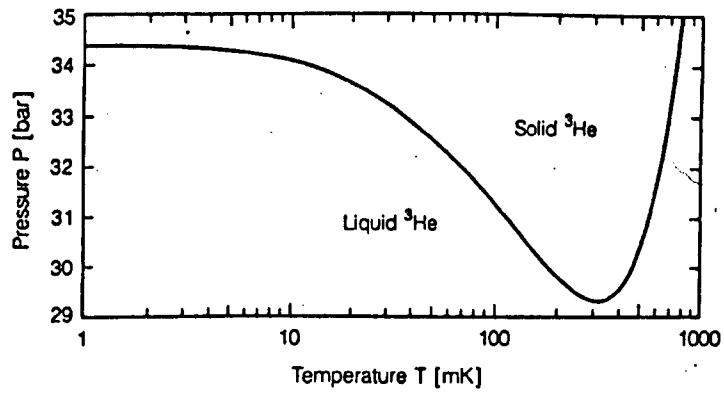

Figure 5.5: The melting curve of ^{3}He [45].

It is remarkable that ^{3}He does not solidify at ambient pressures and that there is a negative slope of the coexistance curve up to 0.3 K. Both these details indicate that the liquid phase is in fact more ordered than the solid one. The reason being that the low temperature entropy is dominated by the ($I=\frac{1}{2}$) nuclear spins, (other excitations being frozen out). Being a Fermi liquid, the Pauli principle causes the spins of the liquid state to be ordered. However, in the solid state, as the atoms are

localised, there is no such spin ordering and hence the entropy is larger.

One can employ the melting curve by measuring the melting pressure and hence calculating the temperature. This is not a primary thermometer, and the melting curve has been established empirically [46]. The existence of a pressure minimum makes it impossible to measure the pressure at room temperature because there will always be a solid blockage at some intermediate temperature. For this reason the pressure is measured in-situ using a capacitive manometer. The design of the thermometer is taken from Straty and Adams [47], and was constructed in the group by Hill and Meeson [42]. The principle is that one wall of the ^{3}He cell is constructed from a thin sheet of hardened BeCu and acts as diaphragm connected to a movable capacitor plate. Hence one expects the capacitance to be inversely proportional to cell pressure. The capacitance is measured using an Andeen Hagerling (AH) 2500A 1 kHz ultra precision capacitance bridge. The precision of the thermometers has been calculated to be 5 μK [42]. As part of this Ph.D. a *LabVIEW* programme was written, which aided calibration of the three melting curve thermometers.

5.4 The SQUID susceptometer.

An ac susceptometer (see figure 5.6) measures the magnetic response of a material by applying an alternating modulation field, and measuring the voltage generated across a coil which is well coupled to the sample. As the magnetic susceptibilities of most materials are small, the voltage contribution from the sample will just be a small fraction of that produced by the modulation field. In an effort to remove this larger contribution, an astatic coil is employed - A coil with each half wound in a different direction and the sample only well coupled to one half. In practice, it is impossible to balance the coils perfectly, so fine tuning can be achieved by inductively coupling a signal into the circuit at the same frequency with a suitable phase and amplitude - electronic balancing. Electronic balancing is also particularly useful in dHvA experiments when one is not interested in the bulk susceptibility, but only the small oscillations superimposed upon it. The signal is therefore in the form of an oscillation at the reference frequency, with an amplitude proportional to the (balanced) susceptibility. Conventionally one amplifies the signal and then demodulates it (and amplifies it further) with a lock-in amplifier.

This method has been used successfully down to temperatures of 20 mK. At lower temperatures the limitations to the signal to noise ratio arise from the fact that one is forced to adopt a small rate of change of modulation field (due to eddy current heating in the sample), and the finite input noise in the amplification process. This noise is attributable to the Johnson noise present in the leads running from the coils to the (room temperature) amplifier.

If one intends to go to lower temperatures, the modulation amplitude (or frequency) must be reduced further and so the sensitivity of the amplifier becomes yet more crucial. Here we adopt the technique of using a SQUID to achieve these goals. The SQUID employed in this study was a niobium, *Conductus* [48] LTS d.c. SQUID sensor. For details of SQUID operation see appendix A or the books by Gallop [49] and van Duzer [50]. However, for the purposes of this discussion the SQUID can be

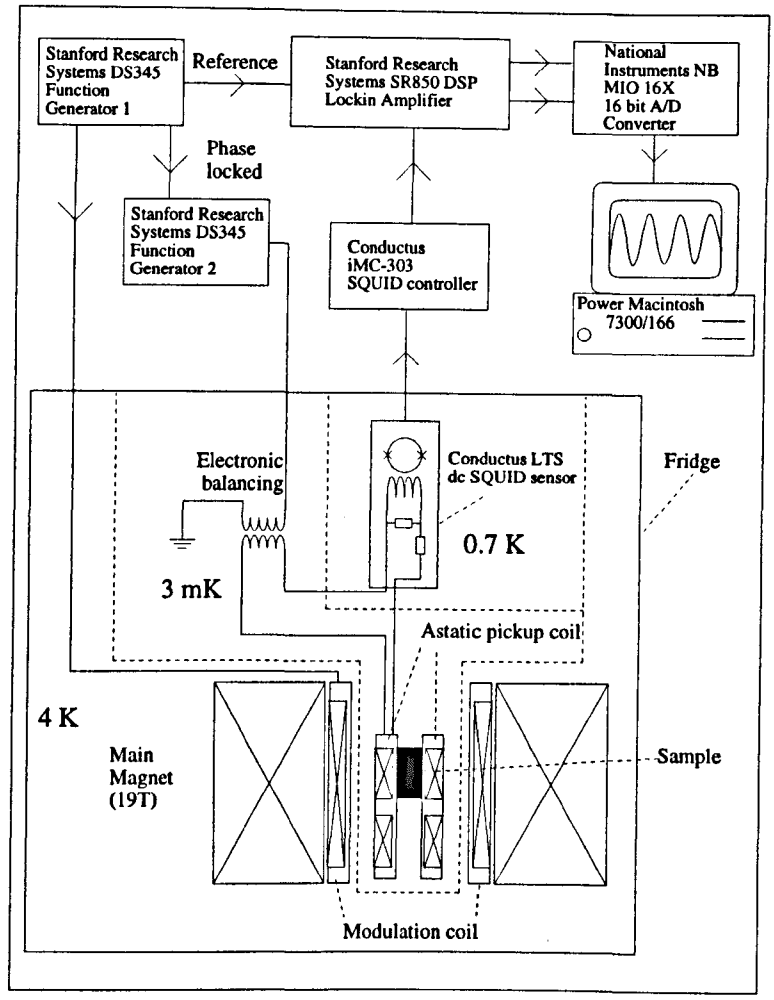

Figure 5.6: Schematic diagram of the SQUID susceptometer. The various temperature regions are bounded by dashed lines.

considered as a current to voltage amplifier with gains of up to 7×10^6 V/A and an input noise floor of $1\,\mathrm{pA}/\sqrt{\mathrm{Hz}}$.

If one were to attach a superconducting input circuit then the only impedance present would be that due to the inductances of the input, pickup and balancing coils. One then has a flux transformer, with a frequency independent response. In this regime any changes in d.c. magnetisation will be registered at the output of the SQUID.

There are a number of reasons why this circuit is impractical. When operating the susceptometer in a 17 T magnetic field, there will be approximately $4 \times 10^8\,\Phi_0$ inside each turn of the pickup coil. Using the measured mutual inductance between the input coil and the SQUID, one would then have to balance the coil to better than one part in 10^9. In reality this setup would be unworkable, so a high pass filtering effect is introduced intentionally, by adding a resistor in series with the coils (see figure 5.6).

The effect of adding the resistor is sketched in figure 5.7. The voltage induced in a resistive pickup coil is proportional to the modulation frequency (part (a.)). The impedance of this circuit will

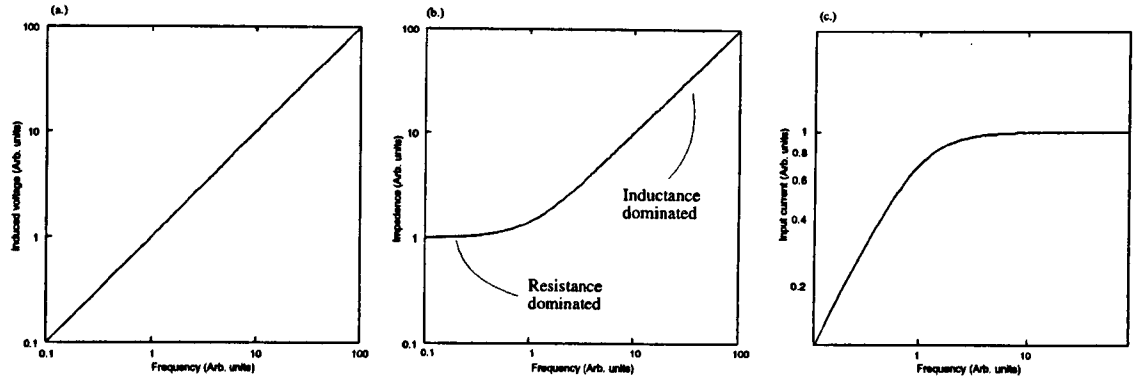

Figure 5.7: A sketch showing the effect of a SQUID input circuit, possessing both inductance (from the coils) and resistance. The induced current is only proportional to frequency as $f \to 0$.

have a constant resistive component which is of importance at low frequencies and and an inductive component, that is proportional to frequency (part (b.)). The resulting current displays a high pass filtering effect (part (c.)).

As one operates the experiment at a finite frequency there is also the option of removing any higher frequency noise too. This is achieved by adding a resistor in parallel with the input coil, which will act like a short circuit when the impedance of the SQUID input coil rises with frequency. This behaviour will be described quantitatively in section 5.5, for the resistances and inductances encountered in the experiment.

5.4.1 Preliminary tests.

On arrival, the SQUID was tested to ensure that the specifications quoted in its manual were correct. The noise floor was checked by leaving the input coil 'open' and immersing the SQUID into a transport Dewar. The SQUID controller output was then connected to a *National Instruments* NB MIO 16X 16 bit A/D converter and analysed using *LabVIEW* software. Figure 5.8 shows a SQUID input noise floor of $1 \times 10^{-12}\,\mathrm{A}/\sqrt{\mathrm{Hz}}$, (equivalent to a flux noise in the SQUID of $5\,\mu\Phi_0$).

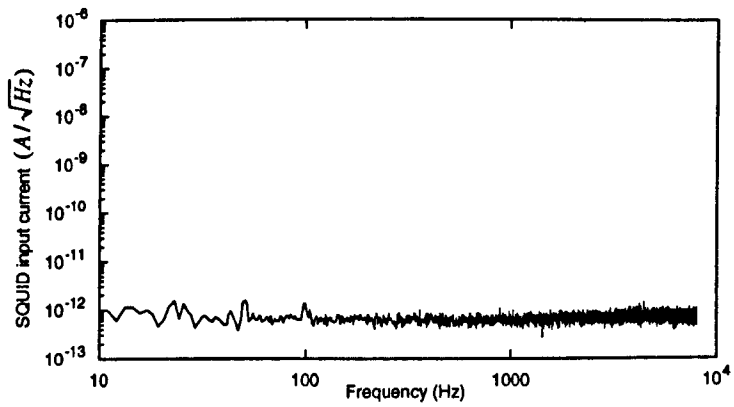

Figure 5.8: An FFT of the noise entering the SQUID sensor with an open input circuit. The SQUID gain is ×500. The SQUID input noise floor is $1 \times 10^{-12}\,\mathrm{A}/\sqrt{\mathrm{Hz}}$.

The V/Φ_0 gain was also checked. This was a simple test and involved injecting a d.c. magnetic flux into the SQUID ring using the 'offset' facility on the SQUID controller and then resetting the SQUID. When an offset is introduced that produces approximately one Φ_0 of flux in the SQUID ring, a reset will cause the SQUID to lock onto the next minimum of the V/Φ curve. The change in output voltage will correspond to the V/Φ_0 transfer function for that particular gain. This experiment was repeated with a variety of gain settings and each time was found to agree with the 2 significant figure quoted in the manual (0.28 V/Φ_0). The final test was to measure the input current/SQUID-flux ratio, i.e. the mutual inductance between the input coil and the SQUID. This test was slightly more complicated because it involved injecting a current directly into the input coil of the SQUID. A 9V d.c. voltage source was employed with a potential divider to introduce currents of the 0.1 μA level.

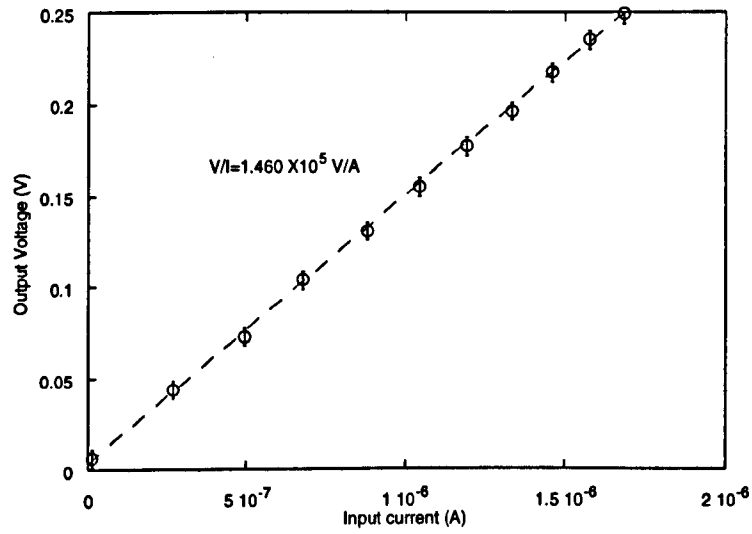

Figure 5.9: Measurement of the V/I transfer function for a gain of $\times 10$.

As can be seen from figure 5.9, this crude experiment had a low enough noise to produce a good fit to a straight line. The measured value (1.46×10^5 V/A) was slightly larger than the quoted value (1.4×10^5 V/A), but the mutual inductance between the input coil and the SQUID is expected to depend upon the impedance of the input circuit. This also means that this value cannot be used with confidence, once the susceptometer input circuit is attached.

To develop the susceptometer, a probe was constructed that allowed rapid cool-down of the SQUID in a transport Dewar (see figure 5.10). Trouble shooting the susceptometer, whilst installed on the cryostat was not viable because a complete thermal cycle typically takes almost a week and increases the chances of a fault developing, each time. This way, it was also possible for other work to be performed simultaneously on the cryostat.

The first modification to be made to the SQUID, consisted of changing the cable linking the sensor to the (room temperature) flux locked loop. The SQUID employed for this experiment came supplied with a so called 'cryogenic cable' consisting of 5 pairs of 31 swg Cu wires, double shielded with phosphor-bronze braid. This would have been too thermally conductive to install in the cryostat,

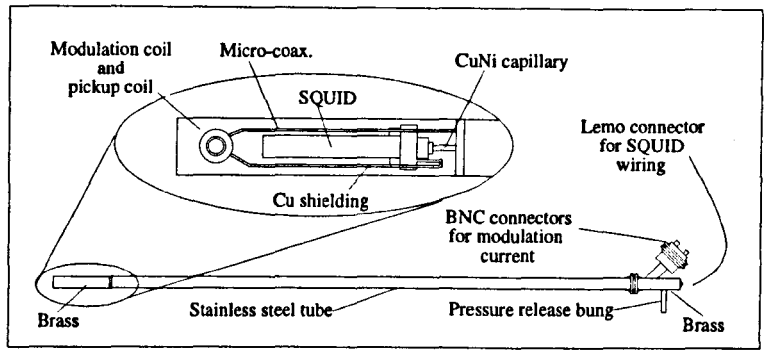

Figure 5.10: The SQUID test probe. Using this probe it was possible to solve any teething problems the susceptometer had, without the slow thermal cycling times of the mK system. The main properties tested were the maximum permissible wire resistances, the level of screening required, different input circuit configurations and a test to see if the SQUID would still function at 1.2 K.

so it was necessary to discover under what conditions the SQUID would operate reliably. It was found that using five twisted pairs of 48 swg Cu wire with an estimated resistance of 3 Ω and total heat leak of 0.2 mW, the noise floor was the same as that measured using the cryogenic cable. The tuning characteristics were found to be slightly different to before, which is what one would expect if resistances were added to the circuit.

The next stage in the development was to produce a replica of the susceptometer. Initially this was done using the simplest means possible. A 2×34 turn pickup coil was wound on a *Hysol* former using 50 μm CuNi clad *Vacuumschmelze* superconducting wire. The wire was twisted and clamped to the input of the SQUID sensor. The modulation field was provided by a 200 turn coil wound on a concentric former. Connection to room temperature was by way of stainless steel micro-coax. Initially the experiment was found to be highly unstable and the SQUID would frequently unlock. The exact cause of the unlockings was never located with precision but other experiments in a different part of the building were found to suffer similar problems and a possible culprit was r.f. interference originating in the paging system of a nearby hospital. Once the input circuit was carefully screened with copper, the problem was found to be reduced, although not eradicated. Moving the transport Dewar to another room, completely solved the problem. This is presumably due to screening effects from the building.

It was then necessary to design suitable resistors for the input circuit. Previously the wire was simply clamped to the SQUID input coil, and the series resistance was achieved by relying on the finite conductivity of the wire matrix and any contact resistance. There was no control over the value of this resistance. To try and produce a more systematic arrangement, small pads were constructed out of manganin. Manganin was chosen because suitably small resistances could be created using samples a few mm^3 in size and because it is known to have a very small thermal coefficient of resistivity. It was possible to produce resistances of the required value by a simple geometric calculation although the actual values were found to vary by ± 30 % from the calculated value, (but not from run to run). This is possibly due to a, still significant, contact resistance between the tag and the wire. An example of

a measured frequency response is shown in figure 5.11.

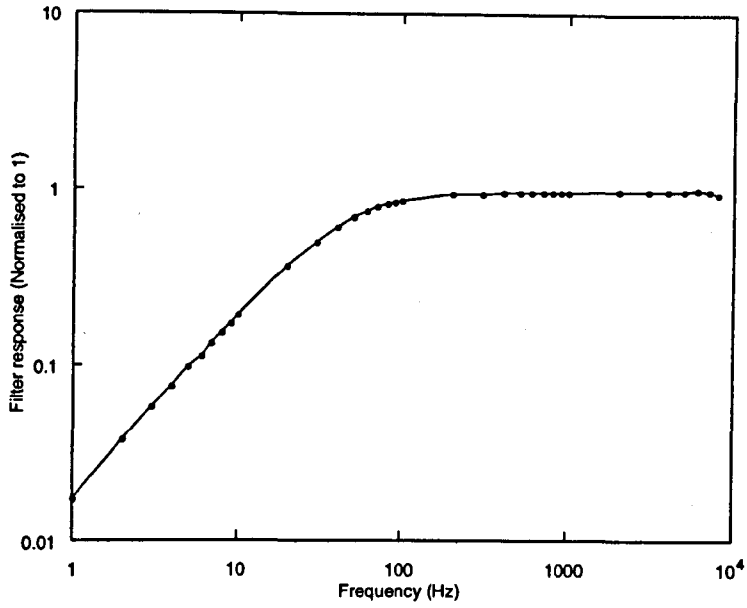

Figure 5.11: The measured input circuit filter response for a series resistor of 8 mΩ, employing the replica susceptometer contained within the transport Dewar probe. The 3 dB point given by R/L is 60 Hz. At higher frequencies slew rate effects are apparent.

5.4.2 Installation on the cryostat.

There are four possible locations for dIIvA susceptometers on the cryostat, the three turning points of the demagnetisation field and the maximum of the main field. In this project, two susceptometers were installed (one for each magnet). The susceptometer located in the 17 T magnet will be referred to as the main susceptometer and the one in the 8 T demagnetisation field, the secondary susceptometer. An extra SQUID was also installed for future thermometric or experimental work, although in this study it was just connected to a pickup coil without r.f. screening, to test the viability of using the SQUID in this mode. To avoid repetition, this chapter will concentrate on the operation of the main field susceptometer, mentioning any differences to the secondary susceptometer. The main susceptometer circuit is shown in figure 5.6.

For the main susceptometer, the modulation field is provided by a coil clamped to the main field magnet in the ^{4}He bath (see appendix B), whereas for the secondary susceptometer, the coil is mounted on a concentric *Hysol* former, as was used in the test probe. The reason for this is that it is possible to still employ a superconducting modulation coil in the 8 T region, but the 17 T field of the main magnet is above the critical fields of all superconducting wires that could simply be used for this application. Both coils are driven by a Stanford Research Systems DS345 30 MHz synthesised function generator. The pickup coils for the two experimental regions are shown in figure 5.12. They were designed to have good coupling to the sample and a self inductance similar to that of the SQUID input coil, and typically consist of between 14 and 35 turns on each side of a *hysol* former. A series

electronic balancing coil is inductively coupled to a second DS345 function generator. By using the phase lock facility it is possible to null the signal by adjusting the relative phase and amplitude of the other DS345.

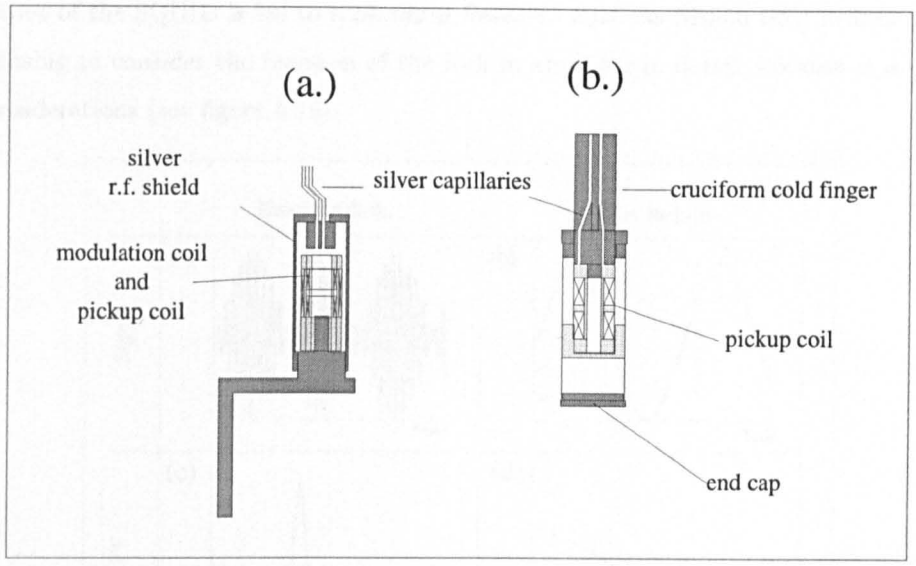

Figure 5.12: The pickup coil arrangements for (a.) the secondary susceptometer and (b.) the main field susceptometer. In (a.) the modulation coil is housed within the r.f. shield and consists of 200 turns of 50 μm *Vacuumschmelze* CuNi clad superconducting wire. The pickup coil (constructed of the same wire) contains 43 turns each half. In (b.) the modulation coil is mounted externally and the pickup coil consists of 14 turns of 250 μm copper wire.

To produce the same resistance as in the test, the SQUID was wired to the cryostat using 47 swg Cu wire. Three looms of five twisted pairs enter the IVC via three vacuum tight, *Lemo* sockets. The sockets are mounted on a stainless steel plate, fitted with a *Klein* flange so that it can be leak tested separately to the rest of the system. The cable was heat sunk at the 4.2 K top plate, the pot plate and at the still plate, where the SQUIDs reside, (see figure 5.2 on page 34). The wiring from the top-plate to the SQUID is screened with CuNi capillary, and heat sinking is achieved with a design of bobbin that maintains shielding. For the SQUID input circuit, superconducting wire is used for the distance to the base of the demagnetisation stage, then in the vicinity of the high field magnet it is necessary to swap over to copper wire. A convenient location for this junction is in the screened box containing the electronic balancing circuit.

A variety of noise sources were found to be present in the main field susceptometer (as will be discussed later in section 5.6.1). A series of low frequency oscillations meant that it was desirable to have a high pass filter with quite a high cutoff, so a 0.05 Ω series resistor was employed. When sweeping the magnet at high fields, intermittent noise bursts were visible, so a 0.02 Ω parallel resistor was included too. It might seem that these attempts at filtering are futile, as the signal will eventually be filtered by the sharp bandpass filter of the lock-in amplifier. The main point, however, is that it is desirable to filter these sources before they reach the SQUID, because it is a fragile measuring device. High frequency noise can exceed the slew rate of the SQUID and cause it to become unlocked (see

appendix A). The low frequency region is a problem purely because the dominant contributions of the vibrational noise are here. Although they will not cause slew rate effects they can exceed the dynamic range of the SQUID and/or the lock-in amplifier (depending upon the gains chosen for each device).

The output of the SQUID is fed to a *Stanford Research Systems* SR850 DSP lock-in amplifier. It is worth pausing to consider the function of the lock-in amplifier in detail, because it is of relevance to noise considerations (see figure 5.13).

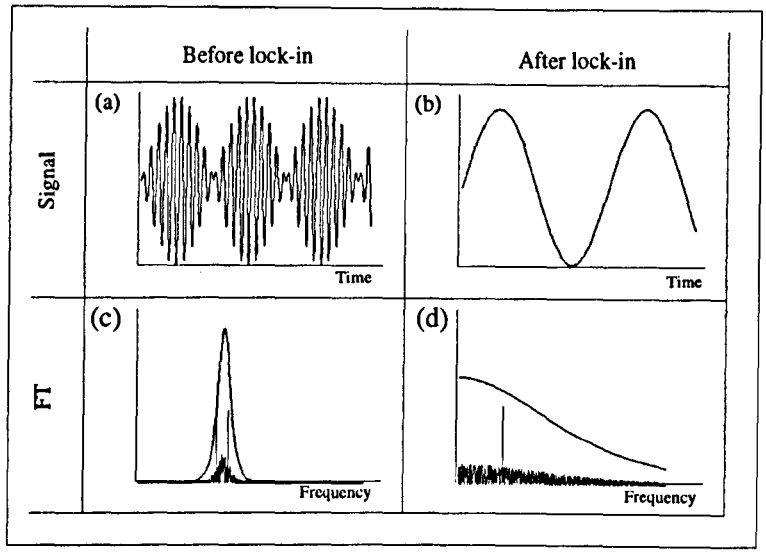

Figure 5.13: The operation of the lock-in amplifier. For simplicity a single time-periodic sine wave is considered. (a) The signal is in the form of an envelope carried on the modulation frequency. (b) The lock-in demodulates the signal, leaving the required waveform. (c) In the frequency domain the envelope takes the form of side bands. The time constant of the lock-in dictates the bandwidth of the filtering around the reference frequency. (d) After demodulating, the sidebands become a single peak in frequency space.

The main point to note is that, if the signal is Fourier analysed, then the lock-in filter cannot improve the signal to noise ratio at a particular frequency. Indeed, its purpose is mainly that of an anti-aliasing filter so that the data can be collected with a finite number of data points without noise at higher frequencies being folded down into the frequency domain of interest. In practice the lock-in time constant, $\tau = 1/2\pi f_c$, must be chosen to give a cutoff frequency f_c less than half the sampling frequency. This is the Nyquist limit. So a clever use of filters can never reduce the noise floor near the dIIvA frequencies. It can only reduce the number of points required to digitise the data.

The above considerations apply to the frequency domain but dHvA oscillations are observed in the magnetic field domain. One can reduce the noise with respect to field by expanding a unit frequency to cover more field. This is the intuitive fact that slower sweeps will be less noisy.[1]

Alternatively, if one wishes to fit to the data, there is a positive advantage to having it well low pass filtered, but this is best achieved afterwards using digital filters. Since the dHvA oscillations are *not* periodic in time it is impossible to choose an optimum filter time constant. However, applying numeric filters afterwards one can first transform to the $1/B$ domain before filtering.

[1] On the condition that the noise is constant with time, which is not strictly true here.

The lock-in itself has other functions than just being a filter. The most important of these is to demodulate the signal. It can also act as a $\times 10^6$ voltage amplifier but since the SQUID has already amplified the signal sufficiently, modest gains are chosen.

5.5 The transfer function.

In dHvA experiments, it is generally not strictly necessary to know the absolute amplitude of the oscillations since the majority of the information is contained in the frequency of the signal and the *variation* of the amplitude with temperature and field. However, it is useful to have an approximate idea of the signals being measured, as a diagnostic tool and for when signals are not observed.

The quantity measured in this experiment is the time derivative of the magnetic moment $\dot{\mathbf{m}}$, but since dH/dt is known, one can easily calculate the susceptibility. Using the L.K. formula one can work back to the magnetisation.

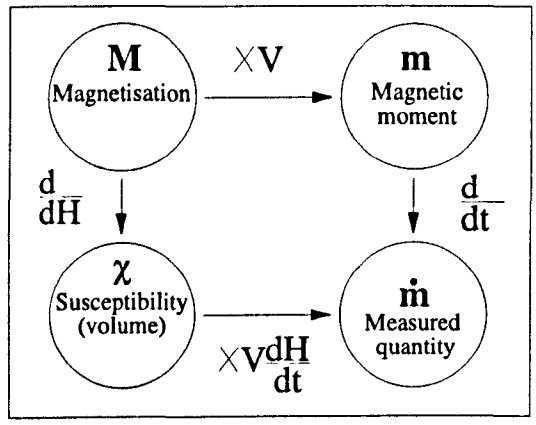

Figure 5.14: The relevant quantities involved in a dHvA measurement.

The transfer function $T(f)$ (the output voltage of the SQUID divided by χ) is given by

$$T(f) = \frac{v}{\chi} = -\frac{GK(f)S(f)cVh_0\omega}{\sqrt{2}} \tag{5.1}$$

where G is the SQUID gain, $K(f)$ is the frequency dependent input circuit (I/V) transfer function, $S(f)$ is an extra attenuation factor which is introduced in chapter 8 to explain some of the results, c is the coil coupling constant, V is the sample volume, h_0 and ω are the modulation amplitude and frequency.

The SQUID gains are listed in table 5.3 (for SQUID 214 with the flux locked loop 001094), and the values of c and $K(f)$ are calculated in the following two sections.

The experiments were conducted at 83 Hz, because in this region the field dependent frequency response was suppressed. At this frequency $K(83)S(83)2\pi \times 83 = 12,000\,\Omega s^{-1}$.

In general the results in this thesis will be presented in output volts, or SQUID input current, because of the uncertainty in the transfer function. So either one could choose error bars accordingly

Setting	V/I (V/mA)	V/Φ_0
×1	29.85	0.00597
×2	59.7	0.01194
×5	149.25	0.02985
×10	298.5	0.0597
×20	597	0.1194
×50	1,492.5	0.2985
×100	2,985	0.597
×200	5,970	1.194
×500	14,925	2.985

Table 5.3: Conversion factors for the *Conductus* SQUID gains (for SQUID 214 and flux locked loop 001094).

which would be much larger than the true noise or one would give a false impression of precision by employing the noise error bars.

5.5.1 The coil coupling constant, c.

The coil coupling can be defined in a variety of ways. Here we adopt the definition that is independent of sample volume.

$$V = c\frac{d\mathbf{m}}{dt} \tag{5.2}$$

hence it is given by the effective flux seen by *all* the turns in the coil divided by the *magnetic moment* of the sample. It involves the proximity of the sample to the coil and the coil turn density.
The sample is irregular in shape, so for simplicity it is modelled as a dipole.

$$\mathbf{B(r)} = \frac{\mu_0}{4\pi r^3}\left(\frac{3(\mathbf{m}\cdot\mathbf{r})\mathbf{r}}{r^2} - \mathbf{m}\right) \tag{5.3}$$

The z component in cylindrical coordinates will thus be given by

$$B_z(r,\phi,z) = \frac{\mu_0 m}{4\pi}\left(\frac{2z^2 - r^2}{(r^2+z^2)^{5/2}}\right) \tag{5.4}$$

The flux through a circle of radius r and at a height z, concentric to the dipole is

$$\Phi(r,z) = \int_0^r 2\pi r B_z(r,\phi,z)dr \tag{5.5}$$

The total flux through the pickup coil is then the sum of this contribution to each turn of the coil, and the coupling constant is

$$c = \frac{V\sum_{turns}\Phi}{m} \tag{5.6}$$

A *Mathematica* programme was written to perform the integrals, resulting in a value for c of 0.003 Ωsm^{-2}. In the $CeCu_2Si_2$ experiment the sample had an approximate volume of 5.25×10^{-9} m^3, so the coupling to the magnetisation, ($C = V/\dot{M}$), was 1.6×10^{-11} Ωms. It is also possible to calculate the coupling constant for other positions relative to the coil centre and this is used in chapter 8.

5.5.2 The input circuit transfer function $K(f)$.

$K(f)$ can be obtained by two different means. It is calculated using a first principles approach and estimates of all the component values. In chapter 8 it will also be seen that experiments conducted on $CeCu_2Si_2$ can provide an experimental value of this quantity with which to compare this estimate. A SQUID input circuit possessing both series and parallel resistors is depicted in figure 5.15.

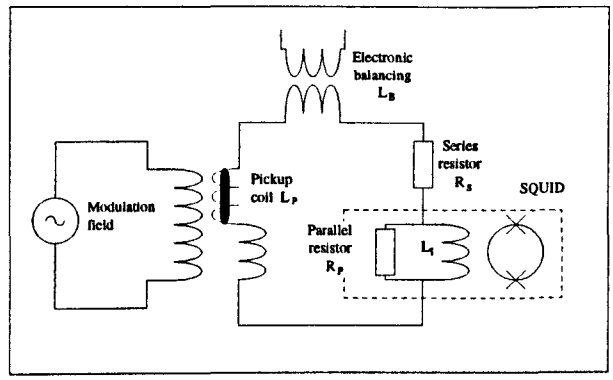

Figure 5.15: A SQUID input circuit possessing both series and parallel resistors.

The filter response is now given by

$$|K(f)\omega| = \left| \frac{\omega z}{(i\omega L_I)(z + R_S + i\omega(L_P + L_B))} \right| \tag{5.7}$$

where

$$z = \frac{1}{\frac{1}{i\omega L_I} + \frac{1}{R_P}} \tag{5.8}$$

A *Mathematica* [51] programme was written to calculate this function for the following values of the components. $L_I = 0.6 \times 10^{-6}$ H, $L_B = 6.5 \times 10^{-6}$ H, $L_P = 1 \times 10^{-5}$ H, $R_S = 5 \times 10^{-2}\,\Omega$ and $R_P = 2 \times 10^{-2}\,\Omega$, resulting in the curve displayed in figure 5.16.

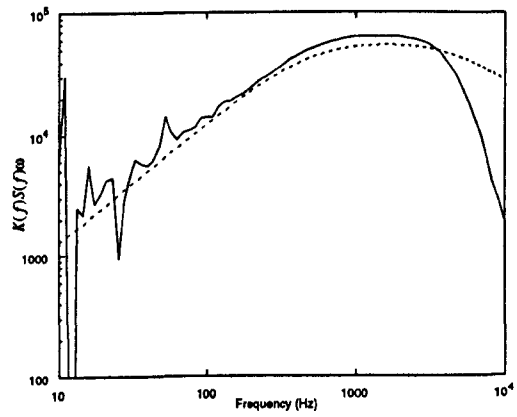

Figure 5.16: The value of $K(f)S(f)\omega$ (for the main susceptometer), based on the first principles calculation (dashed line) and based on the measurement of the superconducting transition in $CeCu_2Si_2$ (solid line).

The first principles calculation is seen to slightly underestimate the amplitude and fails to predict the high frequency attenuation correctly. The former effect is assigned to an uncertain knowledge of

the Φ_0/I transfer function, which is an error that cancels out for the results presented in this thesis. The latter effect is thought to be due to multiple causes because it possesses an approximate f^{-4} behaviour (rather than e.g. f^{-2} for slew rate effects). It is most likely due to a combination of input circuit filtering, slew rate and screening.

5.6 Noise considerations.

Noise will be considered in some detail, reflecting its importance to the experiment. The first, and simplest, analysis yields the smallest resolvable signal, allowing comparison with other experiments. Then a measurement is presented of the noise contributions from all the components associated with the measurement process. Finally a calculation is performed of the input circuit Johnson noise as this appears to be the dominant contribution.

5.6.1 Smallest resolvable signal.

Firstly, one can measure the instantaneous noise floor at the output of the SQUID. This will give a direct measure of the noise sources present in the input circuit. Typical FFTs are shown in figures 5.17 and 5.18.

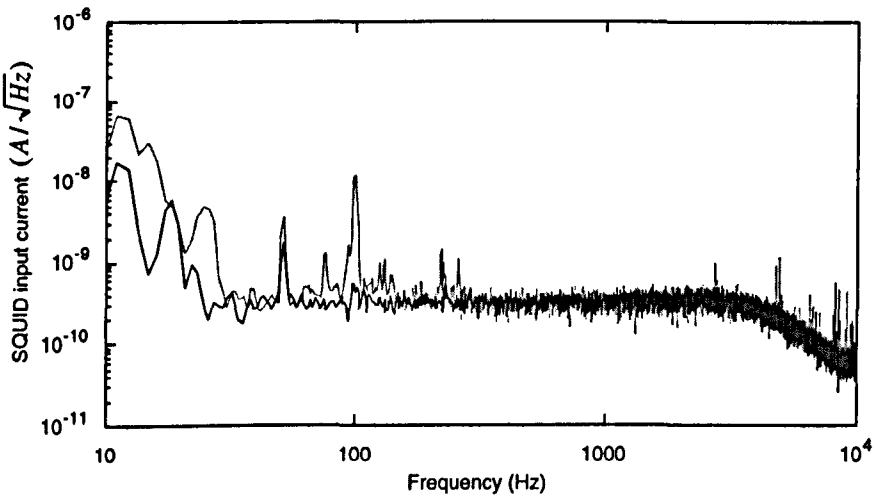

Figure 5.17: The noise spectrum of the susceptometer in zero field (black) and in 16 T (grey). The resolution is chosen as 1.22 Hz to illustrate high frequency noise. The noise floor is 3×10^{-10} A/$\sqrt{\text{Hz}}$. The downturn in noise at high frequencies is due to the filtering effect of the input circuit.

There are strong noise sources present between 10 and 20 Hz. This is presumed to be mostly of vibrational origin. Although there is a large component that remains in a nominally zero field, this could possibly originate from trapped flux in the magnet. An interesting phenomena that has become apparent is that when the demagnetisation field is energised, the low frequency noise is dramatically reduced. This can be ascribed to the demagnetisation field inductively clamping the demagnetisation stage due to Lenz's law, and so preventing the cold finger from vibrating in the main field.

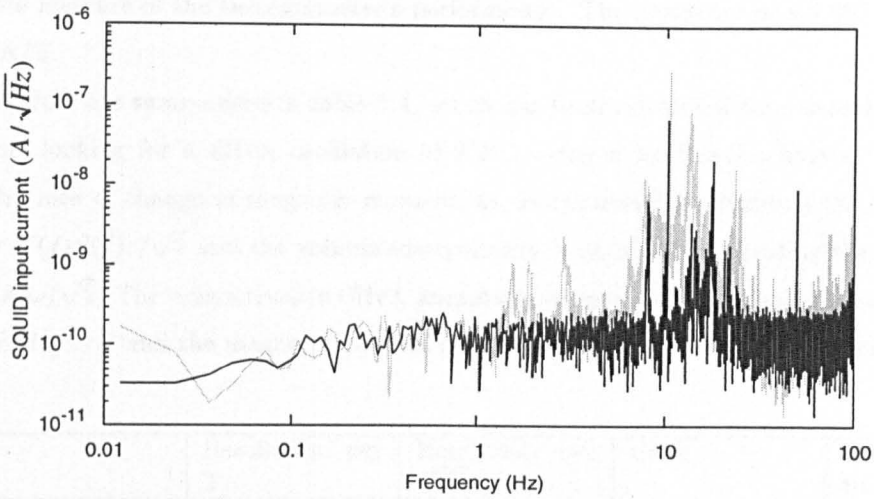

Figure 5.18: The noise spectrum of the susceptometer in 16 T (faint line) and 0 T (solid line). The resolution is chosen to be 0.01 Hz, to illustrate low frequency noise.

A measure which will also indicate the stability of the system is the noise on a field sweep. This is easily measured by taking the FFT of a sweep with respect to time rather than reciprocal field. An example is shown in figure 5.19. The effect of the lock-in can be ignored as long as one measures the noise floor at a sufficiently low frequency that it is not attenuated. Importantly, this noise is found to be of the same magnitude as was measured in the static field, suggesting that the susceptometer is limited by Johnson noise from the input circuit resistors. It should be mentioned that this is not the case when SQUID unlockings are present during a sweep, and the noise floor is dramatically enhanced.

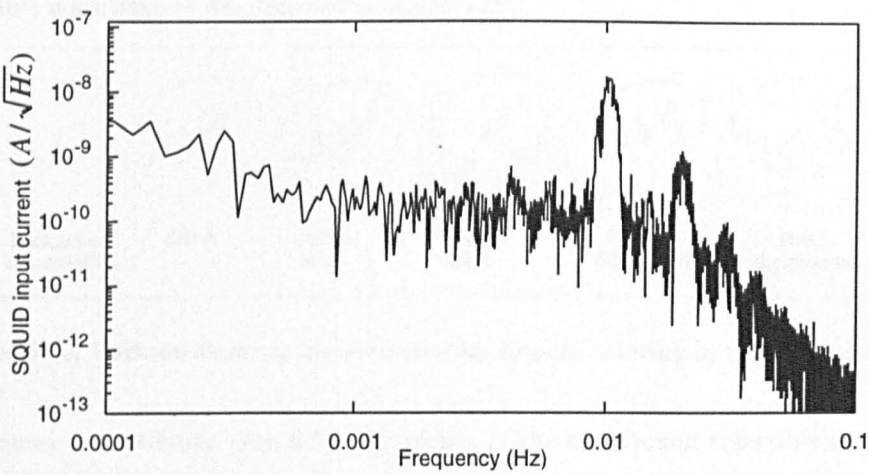

Figure 5.19: The noise floor of a dHvA sweep analysed with respect to time. The noise present at low frequencies arises from the background susceptibility and the spikes at and above 0.01 Hz are silver dHvA oscillations. The noise floor is estimated to be $3 \times 10^{-10}\,\mathrm{A}/\sqrt{\mathrm{Hz}}$. The cutoff above 0.01 Hz is due to the lock-in filter.

Lastly, and of most relevance to dHvA experiments, one can express the noise with respect to reciprocal field, by taking the FFT of the signal with respect to $1/H$ (for a typical sweep). In this way, allowance is made for the fact that a slower sweep will produce a cleaner signal, but it will not

be an absolute measure of the susceptometer's performance. The noisefloor of a 0.001 T/min sweep is 2×10^{-11} A/T.

All these values are summarised in table 5.4, which has been calculated for a sample 5.25×10^{-9} m^3 in volume, looking for a dHvA oscillation of F kT, using a modulation field of 8.2×10^{-6} T at 83 Hz. The rate of change of magnetic moment, $\dot{\mathbf{m}}$, is calculated by dividing the input current noisefloor by $K(f)S(f)c/\sqrt{2}$ and the volume susceptibility is obtained by dividing the noisefloor by $K(f)S(f)cV h_0\omega/\sqrt{2}$. The magnetisation dHvA amplitude M is equal to the volume susceptibility χ multiplied by $H^2/2\pi F$ and the magnetic moment dHvA amplitude $\mathbf{m}$ is obtained by multiplying M by V.

Property	Resolution per T	Resolution per $\sqrt{\text{Hz}}$	Units	Transfer function (A/unit)
SQUID input current	2×10^{-11}	3×10^{-10}	A	1
Rate of change of magnetic moment $\dot{\mathbf{m}}$	3.7×10^{-10}	5.8×10^{-9}	Am^2s^{-1}	0.05
Volume susceptibility χ	2.1×10^{-5}	3.2×10^{-4}	Dimensionless	9.2×10^{-7}
dHvA amplitude M	$6.4 \times 10^{-4}/F$	$10.0 \times 10^{-3}/F$	Am^{-1}	$3 \times 10^{-8} \times F$
dHvA amplitude $\mathbf{m}$	$3.4 \times 10^{-12}/F$	$5.2 \times 10^{-11}/F$	Am^2 (J/T)	$5.8 \times F$

Table 5.4: The sensitivity of the SQUID susceptometer to various properties.

5.6.2 Noise sources.

The principle aim here, is that the noise entering the SQUID will in general be difficult to reduce, but it should be possible to avoid compromising the signal further with the remaining pieces of equipment.

The possible noise sources are depicted in figure 5.20.

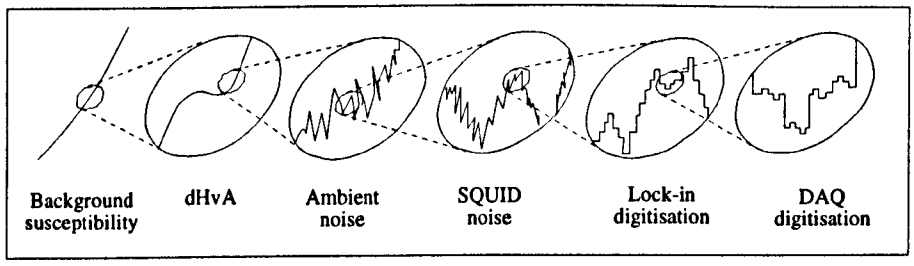

Figure 5.20: Cartoon showing the various noise sources entering in the measurement.

- Background susceptibility. The field dependence of the background susceptibility was found to be very large compared with the dHvA signal. Consequently, to avoid the SQUID overloading, either lower modulation fields were employed or the SQUID gain was reduced. In an attempt to eliminate the problem the signal was balanced dynamically, as will be described later in this chapter.

- de Haas-van Alphen oscillations. The dHvA itself is generally at a much higher frequency than the background susceptibility so these background contributions can be removed by subtracting a suitable low order polynomial fitted curve.

- Ambient noise. The origin of this is presumably due to r.f. interference entering the fridge, vibrational noise and Johnson noise in the input circuit. The former two sources generally have the characteristic of being isolated to a particular frequency. Vibrational noise has the further property of scaling with field. After the careful vibration isolation and filtering of electrical feedthroughs the noise was reduced to that of figures 5.17 and 5.18. Those peaks that remain in the frequency spectrum, do not contribute directly to the noise floor, but they are undesirable for the reasons already discussed. The remaining background noise, which is seen to be over 200 times larger than that for a SQUID with an open input coil, is thought to be due to Johnson noise in the input circuit resistors. This idea is pursued in the next section, where the calculated Johnson noise (9×10^{-11} A/$\sqrt{\text{Hz}}$) is a similar order of magnitude to that measured (3×10^{-10} A/$\sqrt{\text{Hz}}$). As this contribution is so large, it might eventually be desirable to move the resistors (which are presently located within the SQUID sensor shield at 0.7 K) to a colder region of the refrigerator.

- The SQUID noise. This is assumed to originate mostly in the SQUID amplification circuit, and only partly be due to any inherent Johnson noise in the SQUID. The value is taken as that of the SQUID output when the input terminals are left open circuit. In terms of SQUID input current, it was measured to be 1.4×10^{-12}A.

- The lock-in noise. This will be due to the input noise of the lock-in and the finite resolution of the electronics. The input noise was measured as 340 nV and any noise due to digitisation of the signal was found to be less than the input noise of the DAQ board.

- The input noise of the data acquisition board is governed by its finite voltage resolution. It is measured to be 1.4 μV.

5.6.3 Johnson noise calculations.

The purpose of this section is to estimate the expected Johnson noise originating from the input circuit resistors, to ensure that it is this and not some other contribution that ultimately limits the sensitivity of the susceptometer. The Johnson voltage generated over a bandwidth, B, by a resistance, R, at a temperature, T, is

$$\sqrt{4k_BTRB} \tag{5.9}$$

The current noise generated in the SQUID due to an input circuit possessing only a series resistor, is therefore

$$I_{RMS} = \frac{\sqrt{4k_BTR}}{\sqrt{R_S^2 + \omega^2(L_P + L_B + L_I)^2}} \tag{5.10}$$

This possesses the unusual property of increasing, at low frequencies, as the series resistor is lowered, because its impedance scales linearly whereas the Johnson voltage scales to the square root.

The case with two resistors is modelled as the incoherent summation of the current due to the individual resistors (see figure 5.21). One obtains the equation

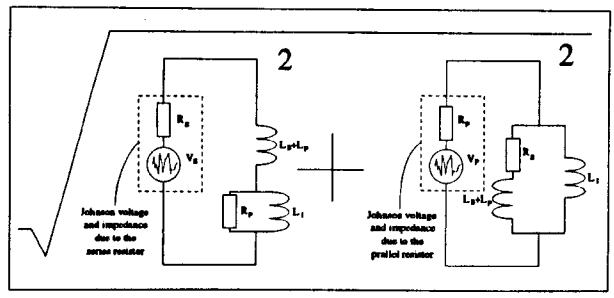

Figure 5.21: A model of the Johnson noise due to two resistors as an incoherent sum of the currents.

$$I_{RMS} = \frac{\sqrt{4k_BT}}{i\omega L_I}\sqrt{\left|\frac{\sqrt{R_S}(R_P^{-1}+(i\omega L_I)^{-1})^{-1}}{R_S+i\omega(L_B+L_P))^{-1})^{-1}}\right|^2+\left|\frac{\sqrt{R_P}}{R_P((i\omega L_I)^{-1}+(R_S+i\omega(L_B+L_P))^{-1})+1}\right|^2} \tag{5.11}$$

Substituting the estimated component values for this experiment, produces the curve shown in figure 5.22. It should be noted that the low frequency value is less than a third of the measured value (see figure 5.17), but this could be due to uncertainties in the mutual inductance between the SQUID and its input coil, when the entire input circuit is connected. This uncertainty does not effect the predictions of the thesis. The downturn at higher frequencies is also seen to be less sharp, although this could be due to uncertainties of component values. The similarities are convincing enough to conclude that the background SQUID noise is of thermal origin.

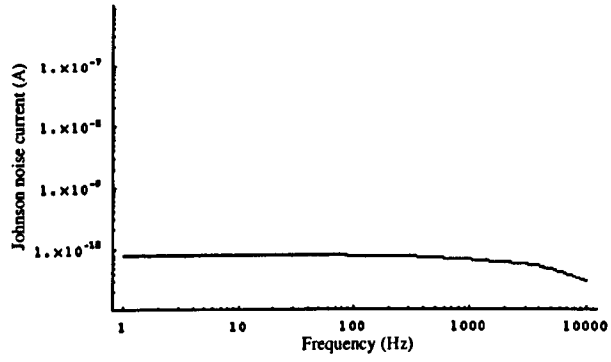

Figure 5.22: The predicted Johnson noise for the resistances and inductances employed in the susceptometer, based on equation 5.11.

5.7 System development.

Although the SQUID generally operated reliably, it was found to frequently unlock in sweeps performed at high magnetic fields. The initial causes of this seemed likely to be, either some vibrational contribution, that grew linearly with field strength, producing a large enough rate of change of field to unlock the SQUID, or the stray field from the magnet penetrating the SQUID shielding and causing it to unlock.

It took six months to conduct tests which localised the fault and went some way to curing it. A preliminary series of tests were conducted with no modulation field applied to the input of the SQUID, and simply logging the output on the computer DAQ interface. A typical trace is shown in figure 5.23.

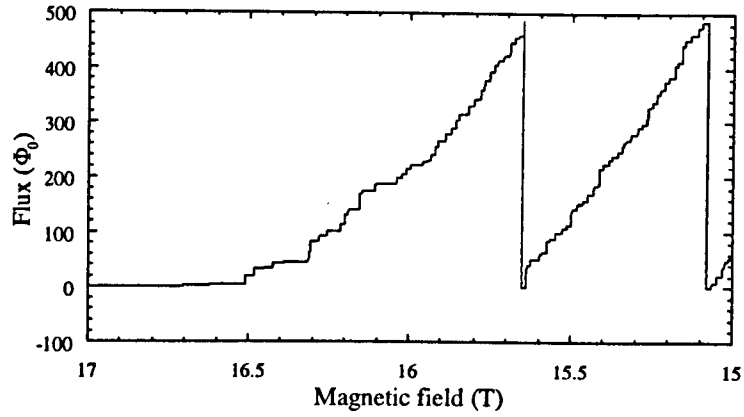

Figure 5.23: The SQUID output during a field sweep from 17 to 15 T. The small steps are unlockings and the large jumps are resets. The gain was set to $\times 1$. Typical unlocking sizes are 2-10 Φ_0. Note the hysteretic, calm half tesla before unlockings occur.

The following characteristics were noted.

- The problem was only present in the high field magnet and chiefly only appeared above 8 T.
- The rate of unlocking events was roughly proportional to the sweep rate. This meant that there was generally a fixed number of unlockings per field interval, consequently the problem could not be solved by simply sweeping the field at a slower rate. Long traces with the field held constant were found to be stable.
- There appeared a form of hysteresis in that, even in the high field region, the first half tesla was free from unlockings.

These facts were not consistent with the original ideas presented above. If the unlockings were due to the tail vibrating in the field it is not clear why the response would be hysteretic, and equally why the SQUID would be stable in constant field.

To gain a better understanding of the exact nature of the unlockings, a *LeCroy* 9410 150 MHz oscilloscope was employed. Originally part of our pulsed field experiment, this device has the capability of triggering on, and capturing individual events. The SQUID output was monitored directly, as was the susceptometer modulation coil via a university built current to voltage amplifier. The idea behind this is that the modulation coil is attached to the magnet assembly and is mechanically remote from the insert, so using it as a pickup coil can help localise the fault. An example of one of the triggering events is shown in figure 5.24.

One can see that noise is generated simultaneously in both the coil and the SQUID. The SQUID displays an oscillation at 80 Hz that decays with time (superimposed upon the low frequency fridge

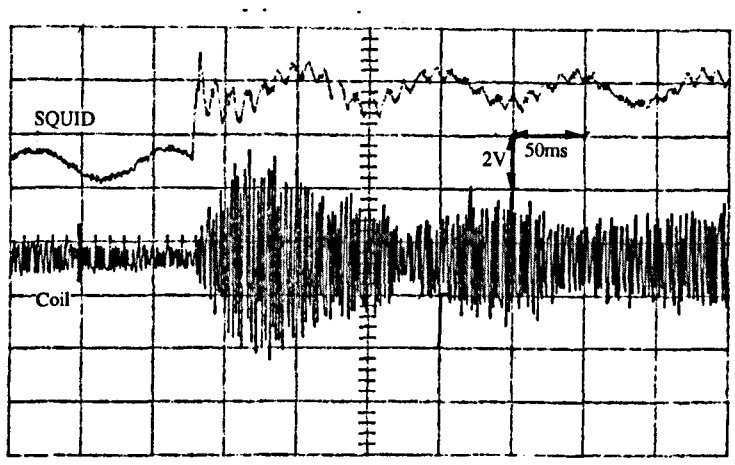

Figure 5.24: One of the unlocking events captured with the LeCroy 9410 oscilloscope. The upper trace shows the output of the main field SQUID while the lower one shows the signal induced in the modulation coil.

vibration), suggesting a vibrational cause of the problem. Another alternative would be that the oscillations are due to the SQUID feedback circuit 'ringing', although one would expect this phenomenon to be in the region of 250 kHz. The fact that an unlocking always coincides with a burst of noise visible in the modulation coil, suggests that a possible cause would be vibrations originating in the magnets. When the magnet was swept without the fridge insert inside, the vibrations were still visible in the modulation coil, confirming this idea.

Contact with Oxford Instruments [43] revealed that magnet vibrations are a fairly common problem, hampering the development of vibrating sample magnetometers. No single cause was found to be the root of the problem, but some candidates were.

- The protection resistors for the magnet were found often to contain magnetic impurities. In an external field they can become polarised and as the field is changed the force acting on them changes. One can then envisage that with some slip-stick process and a restoring force they could produce the required vibrations.
- The magnet current leads will carry a current proportional to the magnetic field and will then feel a force in the magnetic field. Again one needs to imagine a slip-stick process.
- The interaction force between the magnets can often produce relative motion between them. This is presumed to be, at most, only a contributing factor because the problem is still present when the demagnetisation magnet is de-energised.

The problem had been cured on other systems by generally tidying up the wiring to the magnets and securing the protection resistors. The magnets are usually constantly kept at 4.2 K, so at a convenient moment (when the helium liquifier was out of action for repairs) the magnets were warmed up.

A variety of possible vibration sources were identified. The magnet leads were poorly secured and in places cut perpendicularly through high field regions. The protection resistors were found to be

loose, the magnet support structure was generally shaky and many of the access lines were free to vibrate.

To remedy these problems (with the help of an *Oxford Instruments* engineer) the current leads were covered in fibreglass sleeving and tie wrapped in a more solid position (with more thought paid to their orientation in the field). Supporting screws were removed and glued back in place with *Loc-Tite* adhesive. Pumping lines were tied down more securely and PTFE sleeving was inserted in any concentric tubes to stop them shaking. The magnet protection resistors have the form shown in figure 5.25, and were remedied by applying silicone sealant as shown.

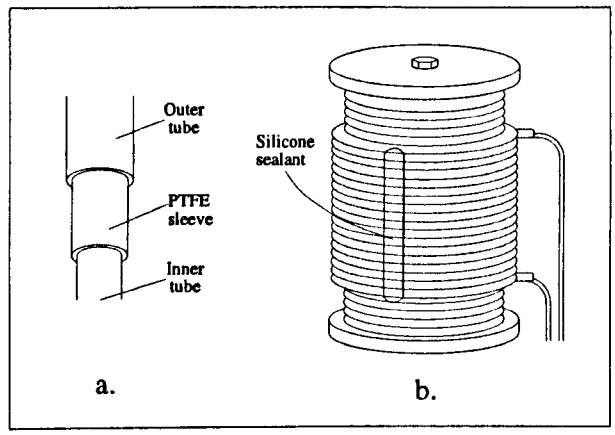

Figure 5.25: (a.) A lot of the support structure consisted of pumping lines and support tubes passing through a wider tube. To prevent them vibrating PTFE tubing was sandwiched in the middle. (b.) Silicone sealant was applied to the resistor in a manner that would provide structural rigidity but would still allow the resistor to radiate heat in the event of a quench.

There were three results of these changes. Firstly, there were far fewer unlockings per unit field. Secondly, the magnitude of the unlockings was less. Most importantly however, there now appeared to be a threshold of 0.005 T/min, below which one could sweep with no unlockings occurring for approximately 80 % of the field sweeps. These factors combined, meant that it became possible to access the high field regions (up to 17 T) if a suitably slow sweep rate was selected.

5.7.1 Dynamic balancing.

The main purpose of the electronic balancing in the SQUID susceptometer is to compensate for any imperfections in the pickup coil. This contribution is not field dependent, so it suffices to only balance at the start of the experiment. However, the sample will also have a changing background susceptibility which will be field dependent and if this is appreciably larger than the dHvA oscillations themselves, it will compromise the sensitivity of the susceptometer. It is therefore desirable to be able to introduce an electronic balancing signal that varies with field in the required way. The Stanford Research Systems DS345 30 MIlz synthesised function generator is capable of producing a sinusoidal signal whose amplitude and phase are programmable by a GPIB interface. There are a variety of ways of then telling the function generator the correct amplitude and phase. One possibility is to

employ a lock-in amplifier set with a time constant that is appreciably longer than the dHvA period. The option that was finally pursued was to measure the background susceptibility first, using the SQUID set to a low gain and applying a modulation signal without any balancing. The results of these experiments are shown in chapter 7, figures 7.7 and 7.8. One can then fit 3rd order polynomials to both the amplitude and phase of the background signal. A *LabVIEW* programme was then written to control the function generator. First the user enters the coefficients of the 3rd order polynomial fit. Then (s)he balances the signal as usual, and enters the starting field and sweep rate into the programme. The programme reads the amplitude and phase required to initially balance the signal and then scales them so that the signal remains balanced as the field is swept.

This aspect of the system worked very well but it was frustrated by the fact that the voltage resolution of the function generator was 1 mV, corresponding to a SQUID input noise of 1×10^{-9} A, which is appreciably larger than the noise floor of the susceptometer. On the other hand, the phase resolution was only 0.001^{o} which for the kind of voltages encountered here would correspond to a voltage of 4×10^{-6} V, and a SQUID input current of 4×10^{-12} A, $\frac{1}{5}$ of the susceptometer noise floor. The above calculations were confirmed experimentally. A further problem with the amplitude adjustment was that sometimes the function generator would change internal ranges and its output would drop discontinuously to zero, for approximately 1 ms. In many situations the phase change was more significant than the amplitude change so the system was arranged with only the phase being dynamically balanced. Dynamic balancing was employed for those experiments conducted with the SQUID in the main field between 6 and 8 T.

Chapter 6

Review of $CeCu_2Si_2$.

6.1 Introduction.

$CeCu_2Si_2$ is a particularly interesting heavy fermion because it not only displays superconductivity but also a very unusual phase diagram. It crystallises in the tetragonal $ThCr_2Si_2$ structure. The Ce atoms have the $4f^1$ configuration and possess, for T<150 K, a magnetic moment of $\mu = 2.54\mu_B$, as predicted by Hund's rules ($J=\frac{5}{2}$). The catalogue of experiments performed on $CeCu_2Si_2$ amounts to a roll call of modern condensed matter techniques.

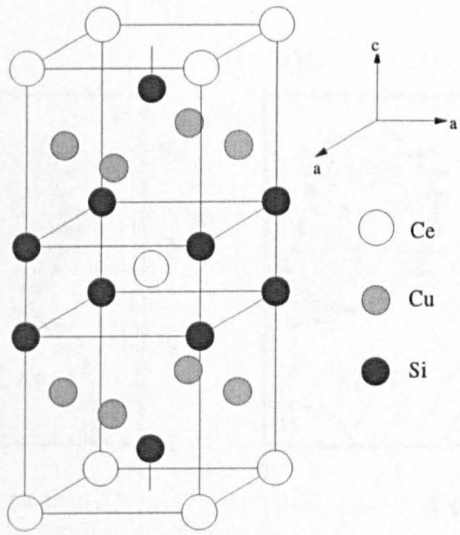

Figure 6.1: The tetragonal ($ThCr_2Si_2$) structure of $CeCu_2Si_2$. Two formula units are displayed (as are two primitive unit cells). The lattice parameters are a = 4.094 Å and c= 9.930 Å [52].

6.2 Thermodynamic and transport experiments.

Early experimental work on $CeCu_2Si_2$ was confounded by a large variety of sample dependent properties. A systematic study by the Darmstadt group revealed that these were due to a sensitive, but

well characterised, dependence upon stoichiometry [53]. The most notable variation was whether or not the samples were superconducting, however three other phases, A, B and C were discovered in certain crystals. The composition phase diagram is shown in figure 6.2 and the meaning of the labels S, A and S/A can be seen in figure 6.3.

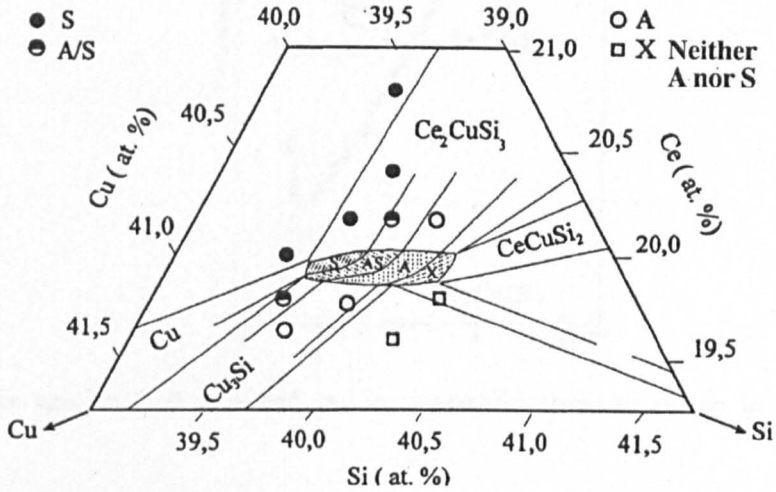

Figure 6.2: The concentration phase diagram of $CeCu_2Si_2$ [54]. Within a very narrow range superconducting and a separate A phase are possible as well as combinations of both or neither. The exact 1:2:2 ratio produces both phases. To achieve this it is necessary to start off with an excess of Cu.

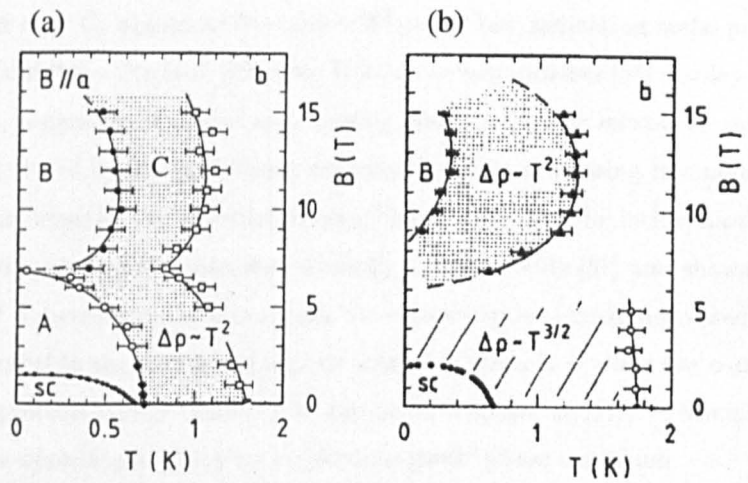

Figure 6.3: The Darmstadt group have adopted a notation where S, A, B and C correspond to regions on the B/T phase diagram and different crystals are classified as S, S/A and A depending upon which phases are present. Pictured are (a) A/S type and (b) S type phase diagrams [53]. The A type crystal possesses only the A phase.

The S phase is the superconducting state initially found by Steglich in 1979 [55]. This research aroused a lot of curiosity because it was a system that displayed superconductivity at low temperatures and Curie-Weiss behaviour above 50K, indicative of localised magnetic moments. The proof of superconductivity rested on the resistivity dropping to less than that of copper, the susceptibility

turning from paramagnetic to diamagnetic and the specific heat plot shown in figure 6.4.

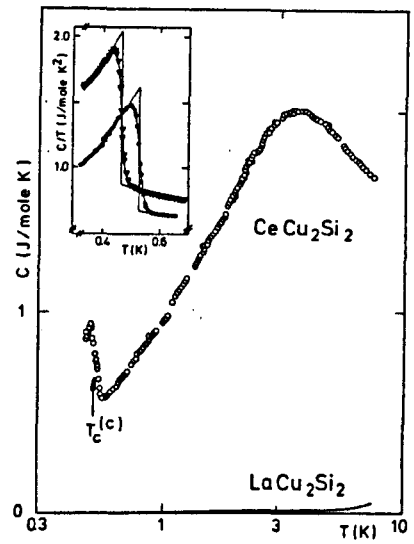

Figure 6.4: The specific heat observed at the superconducting transition in $CeCu_2Si_2$. From Steglich [55].

The specific heat displays the usual heavy fermion, anomalously large linear contribution $\gamma \approx 1$ JK^{-2} mol^{-1}. The jump in specific heat at the superconducting transition, ΔC, is of the order of γT_C suggesting that it is indeed the heavy quasiparticles that are forming the superconducting condensate. Below T_c, contrary to the predictions of BCS theory, the specific heat displays strongly non exponential behaviour. Neither does C_p appear to fit either a T^3 power law, indicating nodal points or a T^2 power law, suggesting nodal lines. Nuclear Magnetic Resonance experiments [56] display a strong reduction of the knight shift, suggestive of singlet type pairing, and the nuclear relaxation rate follows a T^3 law which has been modelled by unconventional superconductivity possessing line nodes.

In the A/S type crystals, the superconducting phase is found to lie inside another phase, A. This phase was revealed by transverse magnetoresistivity measurements [57] and shows up as a deviation from the usual T^2 dependence. In this region the resistivity is slightly decreased when a magnetic field is applied parallel to the a-axis and slightly increased when it is along the c-axis (see figure 6.5). Similarly, the magnetoresistivity differs from the usual increase in ρ(B) commonly observed in the paramagnetic state upon approaching an antiferromagnetic phase transition.

Although the magnetisation only displays a small kink on entering the A phase, ^{63}Cu-NMR [56] studies display an anomalous broadening of the NMR spectrum, indicative of inhomogeneously distributed hyperfine field at Cu sites. Possible explanations are a spin density wave or a spin glass transition. In the S type crystals a spin glass transition had been observed in the temperature dependence of Nuclear Quadrupole Resonance amplitude, but this was found to disappear in an applied field [56]. This characteristic was not shared by the A phase transition hence a spin density wave is currently the most likely candidate for this phase.

The transition is not of a solely magnetic nature, however, and experiments have revealed discon-

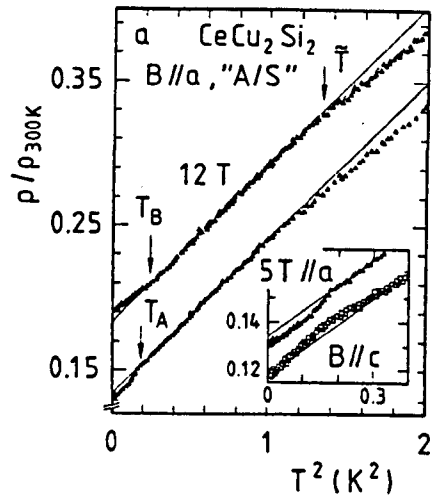

Figure 6.5: Normalised resistivity versus T^2 for an A/S type single crystal at fields of 12 T and 5 T applied parallel to the a-axis. The transitions into phases A and B are clearly visible, as is the T^2, C region. Inset – The behaviour of the A phase transition is orientationally dependent. After Gegenwart [53].

tinuities in elastic constant measured by ultrasound and anisotropic discontinuities in the coefficient of thermal expansion [58]. Comparison of the change in elastic constant, ΔC_{11}, at the A and S transitions in finite field suggest that these two phases do not coexist as is the case for other heavy fermion superconductors, rather the A phase is expelled by the superconducting phase.

One dissenting voice for the spin density wave interpretation is a μSR experiment [59]. Depolarisation of the muon spins in zero field was observed, indicative of either randomness in a static local field H_{int} or fluctuating dynamic local fields. Applying an external field can distinguish between these two alternatives by aligning a static field but having very little effect on a dynamic field. A longitudinally applied field was found to dramatically increase the depolarisation, favouring the spin-glass model.

The phase marked B is even more enigmatic. It shows up as a rise in the magnetoresistivity and a fall in the elastic constant but has not yet been detected by any other probe. Although this is perhaps due to lack of searching in some cases, it appears to conclusively be absent from susceptibility and specific heat experiments, suggesting a substantial reduction in ordered magnetic moment compared with the A phase. Due to its location at high fields and low temperatures, much of the dHvA work contained within this study took place in the B phase.

The C phase is the region in which the resistivity has a T^2 dependence. Unusually it is found to mirror the shape of the A and B phases. The reason for this is thought to be that it is due to short-range magnetic correlations precursive to the transitions into phases A and B.

The general description of such a wide range of behaviour can be viewed in terms of the competition between antiferromagnetic ordering (characterised by a binding energy $k_B T_{RKKY} \approx J_{loc}^2 W$) and local Kondo singlet formation (binding energy $k_B T_K \approx \exp(W/J_{loc})$), as mentioned with regard to Doniach's Kondo necklace (chapter 3). Here $J_{loc} < 0$ is the local 4f-conduction electron exchange integral, which decreases with a smaller unit cell, and W the conduction bandwidth. At a critical

value of J_{loc}, tuned by the control parameters pressure and composition, antiferromagnetic order can be suppressed, $T_N \to 0$. Either side of this quantum critical point (QCP) one observes the usual heavy fermion properties with short range and long lived antiferromagnetic fluctuations mediating the interactions between the quasiparticles. These interactions grow on approaching the phase transition. At the critical point one expects the following non-Fermi-liquid power law behaviour.

$$\text{Low T} \begin{cases} \gamma = \Delta C/T = \gamma_0 - \alpha T^{1/2} \\ \Delta\rho = \beta T^{3/2} \end{cases} \tag{6.1}$$

$$\text{Higher T} \begin{cases} \gamma = \gamma_0' \ln(T_0/T) \\ \Delta\rho \sim T^{\varepsilon} \qquad\qquad \varepsilon \approx 1 \end{cases} \tag{6.2}$$

The S type samples are thought to be located close to the QCP, and indeed in these specimens, the A and C phases are replaced by a region possessing $\Delta\rho \propto T^{3/2}$ and $\gamma = \gamma_0 - \alpha T^{1/2}$ behaviour. To further investigate this idea, the Darmstadt group endeavoured to change the control parameter in a well defined manner. The two approaches taken were doping with Ge to produce $CeCu_2(Si_{1-x}Ge_x)_2$ [60] and the application of pressure [61]. Ge is isoelectronic to Si but it has a larger atomic size so the unit cell for the antiferromagnet $CeCu_2Ge_2$ is 178 Å^3 compared to 167 Å^3 for $CeCu_2Si_2$. Looking at a range of concentrations, the A phase is found to evolve continuously into the antiferromagnetic phase, whilst the superconducting phase becomes suppressed. Similarly, the application of pressure was found to transform A-type crystals to S-type ones, with the associated arrival of non-Fermi-liquid effects.

6.3 Neutron scattering experiments.

Neutron scattering experiments on $CeCu_2Si_2$ have primarily been concerned with determining the nature of the excited states of the Ce^{3+} ion and the relative importance of valence fluctuations and Kondo-type spin fluctuations. The earliest experiment was performed by Horn *et.al* [62]. The low temperature spectrum consists of a quasielastic line and two inelastic lines at 12.5 and 31 meV. The quasielastic half-width and temperature dependence were characteristic of those seen in Kondo systems. No indication of any magnetic ordering was found by neutron diffraction down to the millikelvin range in any of the studies. Subsequent experiments have used polarised neutrons and have resolved the Kondo resonance with greater detail. The susceptibility was found to correspond to that measured in ac susceptibility experiments.

6.4 Fermi surface probes.

A study (on an S-type crystal) has also been performed by 2D angular correlation of positron annihilation radiation (2D ACAR) [63]. Experiments were conducted above (50 K) and below (4 K) the characteristic temperature ($T^* \approx 15$ K) in an effort to see the level of f-electron localisation in the

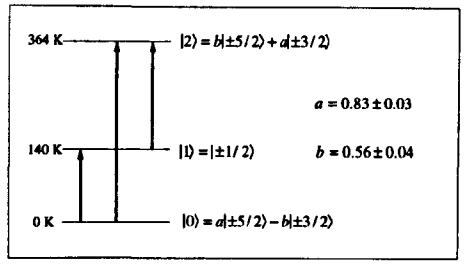

Figure 6.6: The crystal-field level scheme of Ce^{3+} in $CeCu_2Si_2$ obtained from neutron scattering experiments. After Horn *et al.* [62].

two cases. The technique is able to resolve a projection of the density of states onto a 2D surface, but the analysis is complicated by the need to account for the positron's interaction with the electrons. It is thus an experiment without the same resolving power as dHvA but with the benefit of being more flexible. Within the limits of experimental resolution, the general topology (for both temperatures) fitted with that calculated by DFT using LDA for $CeCu_2Si_2$ rather than its homologue $LaCu_2Si_2$. So the study concluded that f-bands were present in both temperature regions.

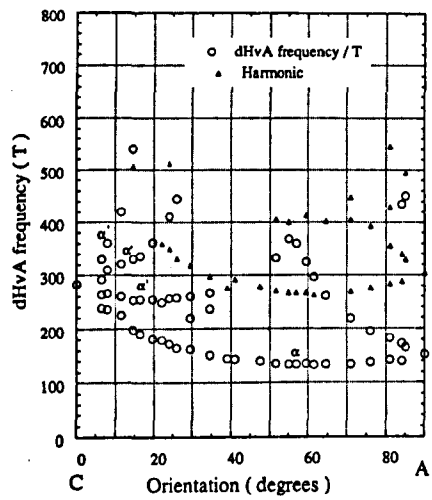

Figure 6.7: The angular resolved dHvA oscillations of Hunt *et al.* [64].

A more conclusive test, allowing very precise Fermi surface and effective mass determination, is provided by dIHvA. Unfortunately the uncertain stoichiometry of this compound has proved a stumbling block in the search for oscillations. The only successful study, was due to Hunt [64] here in Bristol. This work was conducted in a top-loading dilution fridge (TLM). The probe is fitted with a rotating sample holder so it was possible to produce a full rotation plot (see figure 6.7). However, the temperatures were limited to above 20 mK and the sensitivity was only that of a conventional field modulation system, so the study only detected a small, light ($4.6m_e < m^* < 4.8m_e$) section of the Fermi surface. The data were found to produce a convincing fit to a calculation [65] using a relativistic LAPW method within the LDA approximation. A better fit was found when the f-electrons were treated as being confined to the 14 f-orbitals in the ionic core. The experimental effective masses

found were far too small to explain the large linear contribution to specific heat, measured in this material and the band structure calculations suggested that much more extensive sheets of Fermi surface remained to be discovered. However, studies of sample purity and guesses of possible values of effective masses, suggested that there was little chance of seeing the rest of the Fermi surface in the TLM.

6.5 Theoretical description.

A variety of the theoretical approaches discussed in chapter 3 have been used to predict the band structure and effective masses present in $CeCu_2Si_2$. Perhaps the most conventional of these is the local density calculation performed by Harima and Yanase [65]. The motivation for applying such a simple theory is twofold. Firstly, although one anticipates that any predictions for the effective mass will be wildly underestimated, it is instructive to see how closely the topology of the Fermi surface matches that of experiment. It should then be possible to unravel which effects are due to the large renormalisations and which are due to the band mass. Secondly, many of the more sophisticated approaches have a DFT calculation as their starting point. They used a relativistic linearized APW method and obtained the results depicted in figure 6.8.

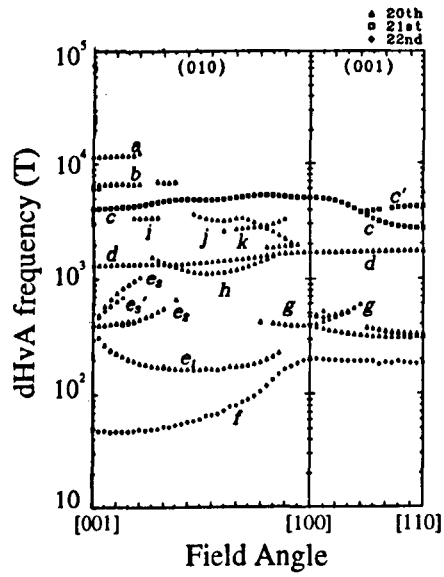

Figure 6.8: The dHvA spectra predicted for $CeCu_2Si_2$ by Harima and Yanase [65].

Sticht *et al.* [66] supplemented a LDA calculation with details based on the Kondo Lattice Ansatz (KLA). This formulation requires the specification of the symmetry of the scattering channel which is taken from neutron scattering data. It is then capable of making predictions of γ, although the results met with only partial success.

Kang *et al.* [67] used the Anderson Hamiltonian in an attempt to model the density of states measured by x-ray photoelectron spectroscopy (XPS), resonant photoelectron spectroscopy (RESPES) and bremsstrahlung isochromat spectroscopy (BIS). The hybridisation matrix elements were obtained from an *ab initio* calculation, performed within the local density approximation, so no fitting parameters were employed. Apart from matching the observed spectra rather well the study also concluded that the system is controlled more by the hybridisation of Ce $4f$ to Si and Cu s/p than to Cu $3d$ states. However a prediction of the band structure was beyond the limits of this calculation.

6.6 Heavy fermion superconductors.

Although this study is not primarily concerned with superconductivity, it would not be complete without mention of some of the ideas for superconductivity in $CeCu_2Si_2$ and its relation to the other heavy fermion superconductors. Some of the general features of heavy fermion superconductivity are as follows.

- The critical field slopes, $-(dH_{c2}/dT)$, are anomalously large near T_c, and, in the case of UBe_{13}, this slope changes substantially for magnetic fields above 1 Tesla.
- The critical fields at zero temperature are larger than the Pauli values calculated with the assumption that the heavy fermion quasiparticles possess a magnetic moment equal to one Bohr magneton.
- The superconducting properties of UPt_3 are remarkably sensitive to small concentrations of impurities.
- UPt_3 displays a complicated B/T phase diagram, featuring more than one superconducting phase.
- The dependence of specific heat, ultrasonic attenuation, thermal conductivity and NMR relaxation rates below T_c are found to be non exponential. A T^2 power law dependence has been found in UPt_3 indicative of line nodes. In UBe_{13} some early experiments showed a possible T^3 dependence but there has since been a convergence of opinion that this material possesses the T^2 form too. As yet, it has not been possible to fit $CeCu_2Si_2$.
- Generally, the non-f-electron reference compounds ($LaCu_2Si_2$ for example) are found to be non superconducting.

Of the microscopic theories currently invoked to explain the above behaviour, $CeCu_2Si_2$ is often treated as a separate case, and it is believed that phonon coupling may make a dominant contribution. Two mechanisms have been proposed [68]. One coupling mechanism results from the additional phase shifts of the scattered electrons caused by the Kondo ions, however it does not appear to be strong enough to explain why $CeCu_2Si_2$ is a superconductor and $LaCu_2Si_2$ is not. The second mechanism is due to the change of the Kondo temperature with pressure or volume, producing strong phonon coupling. This mechanism turns out to be sufficiently large to give a superconducting transition temperature of the order of 1 K.

For the other heavy fermion superconductors a pairing of magnetic origin is proposed and series of pressure studies [69] have produced a p/T phase diagram consistent with this interpretation.

Chapter 7

$CeCu_2Si_2$ experiments and results.

7.1 Introduction.

Once the susceptometer was installed, a number of experiments were performed on a single crystal $CeCu_2Si_2$ sample. A variety of effects were observed, including dHvA oscillations. On the basis of later background tests, most of the oscillations observed can conclusively be attributed to sources external to the sample, although there remain some oscillations which could be genuine. In the course of these experiments over 400 field sweeps were performed, during which much insight was gained into the experimental parameters that can be employed, and as such these experiments constituted as much a development of the susceptometer as a study on $CeCu_2Si_2$. For this reason the results will be presented in chronological order. Many of the results require a lengthy quantitative discussion and this is postponed to the next chapter.

This chapter will first present a short description of the systematics of the experiments. The results of some experiments conducted in the secondary susceptometer will then be displayed. Oscillations were observed in the frequency range 0 – 1.5 kT, although it is still uncertain whether these oscillations originated in the sample. The amplitude of one of these oscillations displayed the unusual property of decreasing at lower temperatures.

The remainder of the results concern the main susceptometer. Some studies of the apparent background susceptibility will be presented. The field dependence was seen to possess a form that was both field and modulation-frequency dependent. Similar anomalies in the frequency response of the input circuit will also be shown.

Oscillations were also observed below 1.5 kT in the main susceptometer, although the individual peaks were far less distinct. Using longer field sweeps, some clear oscillations were seen with frequencies as low as 50 T.

Results of pulsed field experiments will then be displayed that show the $CeCu_2Si_2$ A/B metamagnetic transition, and these results are used to plot a B/T phase diagram.

Then some results of slow, cold sweeps in high magnetic fields will be presented. These allowed

some smaller, high frequency oscillations near 30 kT to be observed and, although mass plots were impossible, an interesting field dependence was found.

Lastly, the results of background tests, with the sample removed, will be presented. The secondary susceptometer showed none of the previously seen oscillations but disconcertingly the principle oscillations observed in the main susceptometer remained. To see whether these oscillations could be coming from contaminants, a microscopic analysis was performed which revealed that indium was present.

7.2 The sample.

The crystal employed in this study was provided by S.Nuttgens of the University of Frankfurt.

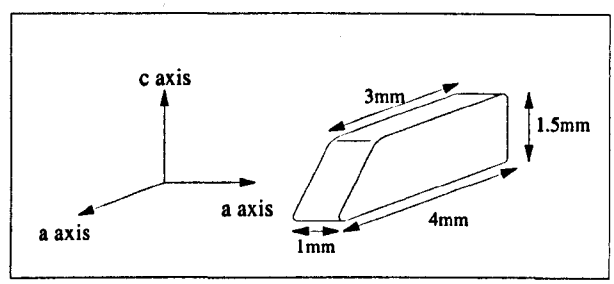

Figure 7.1: The $CeCu_2Si_2$ sample. The approximate sample volume is 5.25×10^{-9} m^3.

The crystal had the slightly irregular form depicted in figure 7.1. This meant that the coupling to the coil would be particularly strong when mounted with the magnetic field parallel to the a-direction. Other orientations are possible with modification to the pickup coil design or by cutting the crystal, but this would inevitably lead to a loss in signal so this study was conducted entirely on the crystallographic a-axis.

Before any work was performed on it using the d.c. SQUID susceptometer, the sample was found to be capable of producing dHvA oscillations in a conventional susceptometer by Hill (see figure 7.2).

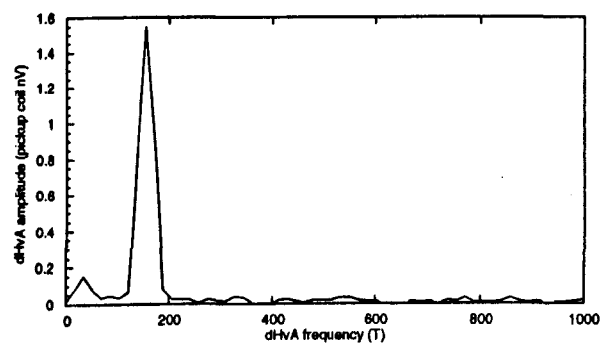

Figure 7.2: Fourier transform of a dHvA experiment conducted on the sample using a conventional dHvA susceptometer. The field was swept between 7.5 T and 13.5 T.

7.3 Experimental procedure.

Each experiment can involve a large number of variables, so a systematic method was adopted for choosing them. Typically one would start off by ensuring that the modulation field does not introduce excessive heating to the experimental region.

7.3.1 Thermal connection.

The thermal resistance between the sample and the cold finger will be due to the sample itself, the silver paste used to attach it and the boundary resistances at each interface. There are no direct reports in the literature of the thermal conductivity of $CeCu_2Si_2$ so it will be approximated as brass with $\kappa \approx 10^{-1}\,\mathrm{Wm^{-1}K^{-1}}$ and the thermal conductivity of the silver paste has been measured to be $2\,\mathrm{Wm^{-1}K^{-1}}$ at room temperature [70]. To extract the low temperature behaviour it is assumed to behave like silver with a residual resistivity of forty [45], giving a low temperature thermal conductivity of $5 \times 10^{-2}\,\mathrm{Wm^{-1}K^{-1}}$. The Kapitza resistance between the materials is completely unknown and is neglected as this should be a system where electronic contact exists and the poor thermal conductivity is the dominant effect.

Using the above values, the total thermal resistance is calculated to be 22,000 $\mathrm{KW^{-1}}$ where the whole length of the sample was considered and the silver paste was assumed to be 100 μm thick. The heat capacity of the sample is calculated to be only $3 \times 10^{-7}\,\mathrm{JK^{-1}}$ at 3 mK. Correspondingly the thermal relaxation time is only 7×10^{-3} s.

A more relevant measure is the permissible amount of heat that can be introduced to the sample without significantly warming it. Using

$$\Delta T = R\Delta Q \tag{7.1}$$

it can be seen that heat inputs of 5×10^{-9} W will only increase the sample temperature by 0.1 mK.

7.3.2 Eddy current heating.

The eddy current heating for the most commonly encountered geometries is given below [45].

$$\dot{Q} = PV\dot{B}^2/\rho \tag{7.2}$$

where

$$P = \begin{cases} r^2/8 & \text{for a cylinder radius } r. \\ \left(\frac{d^2}{16}\right)\left[\frac{k^2}{1+k^2}\right] & \text{for a rectangle, width } w \text{ and thickness } d, \text{ where } k = w/d. \end{cases} \tag{7.3}$$

In practice the dominant heating contribution is from the silver sample mount rather than the sample itself. A calculation of the heating due to the silver post, r.f. shield and end cap shown in figure 5.12

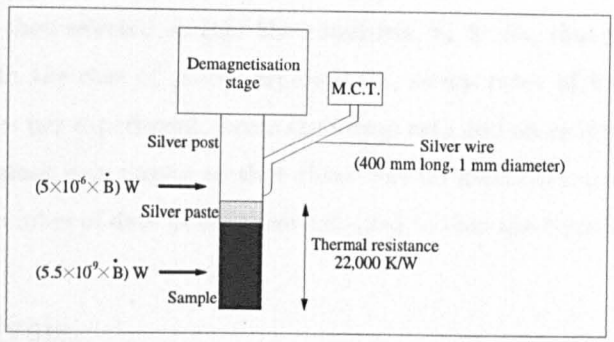

Figure 7.3: A schematic illustration of the heat entering the sample and the silver within the modulation field. The thermal resistance includes the sample and the silver paste. The melting curve thermometer is welded to the tip of the cold finger via 1 mm diameter silver wire.

on page 46 (assuming a resistivity of $\rho = 2 \times 10^{-10} \Omega$ m) gives a value of $(5 \times 10^{-6} \times \dot{B})$ W. The heating in the sample itself only amounts to $(5.5 \times 10^{-9} \times \dot{B})$ W. The situation is summarised in figure 7.3.

In the experiments conducted in the main field, the modulation field was chosen to be 8×10^{-6} T at a frequency of 83 Hz, hence $b_0\omega = 4.2 \times 10^{-3}$ Ts^{-1}. This produces a heating in the tail of 2×10^{-8} W, which is large but tolerable due to its good thermal connection to the demagnetisation stage. The melting curve thermometer also showed no indication of a temperature rise at low millikelvin temperatures even though it is very well connected to the cold finger. The heating in the sample for this $b_0\omega$ is only 2.31×10^{-11} W, which is negligible.

For the secondary susceptometer, heating is far less of a problem because the modulation field is located inside the r.f. shield and the limiting factor was found to be the field dependent background susceptibility, which would overload the SQUID if an excessive modulation was chosen. For these experiments, $b_0\omega = 0.15$ Ts^{-1}, producing an estimated heating in the sample of 8.25×10^{-10}W and in the silver post of 8×10^{-7} W, which is tolerable as this experimental region remains above 10 mK.

So, for each temperature, a suitable field and frequency was employed by the above calculation and by looking for any temperature increase on the thermometers. Care must be taken with the latter technique in predicting the sample temperature, due to boundary resistance, however the melting curve thermometer is well coupled to the cold finger, which we have just seen will be the major heat source.

A particular rate of change of modulation field $\dot{b_0}$ can be achieved by a wide variety of modulation amplitudes b_0 and frequencies ω. According to the modulation technique LK formula (in the low b_0 limit) any of them that produce the same $b_0\omega$ should be equivalent, however because of the input filtering present, this is not the case for the SQUID susceptometer and the proportionality to ω is cancelled by an impedance inversely proportional to ω, at higher frequencies. So if all other factors are constant it is better to operate at a lower frequency and higher modulation amplitude. In the experiments conducted in the secondary susceptometer the modulation frequency was chosen to be 717 Hz, and in the main susceptometer experiments the modulation frequency was chosen to be 83 Hz.

The sweep rate was then selected so that the condition, $\dot{b_0} \gg \dot{B_0}$, that was used to derive equation 4.29, is satisfied. In the case of colder experiments, sweep rates of 1 mT/min were employed, corresponding to 30 hours per experiment. From the sweep rate and an estimate of the dHvA frequencies, a lock-in time constant was chosen so that there was no attenuation of the dHvA oscillations. Finally an appropriate number of data points were collected so that the Nyquist criterion was satisfied.

7.4 Data analysis.

The last stage in the measurement process is the data analysis. Optimally one fits the L.K. formula to the oscillations using a standard fitting routine, such as the Levenberg-Marquart method. These experiments dealt with materials with many dHvA oscillations close to the noise floor, so it was impossible to use this method. It was therefore necessary to Fourier analyse the data.

The analysis was performed on a *PowerMacintosh* computer using software written previously [71] in the *LabVIEW* programming language. Fast Fourier Transforms (FFTs) were employed because they require $n\log_2(n)$ operations rather than the n^2 operations of a conventional Discrete Fourier Transform (DFT). The FFT requires equally spaced data points, and since the data is converted from a series with respect to B to one with respect to 1/B it is necessary to fit a spline curve to it. The programme also has the capability of then fitting and subtracting a polynomial from the data. This is particularly useful for an experiment employing first harmonic detection because a large background signal is present.

For the interpretation of some parts of this experiment the phase of the signal is of interest, so it is worth considering whether the phase of an oscillation is apparent in a Fourier transform. It is important to distinguish between the phase of the modulation signal (instrumental phase) and the phase of the actual dHvA oscillations which are carried on it (dHvA phase). The instrumental phase can easily be distinguished by the lock-in amplifier (except for when the relative phase is $n\pi$) and generally one chooses to put all the signal in one output channel. An absolute determination of the dHvA phase, on the other hand, is more difficult, and generally requires the oscillations to be taken close to the quantum limit. Any dHvA phase information is lost when a Fourier transform is performed, except in a few special cases. If the phase *changes* with field in anything other than a linear way there will be a broadening of the FFT peaks. This is not the only way that peaks can be broadened, however, and any variation of amplitude with field or the finite length of the field sweep can produce a similar effect. If there are two oscillations at the same (or similar) frequency the phase is of great importance and, just as in optics, the signal can add constructively or destructively, or cause beating effects.

7.5 Experimental history.

The first dHvA oscillations that the susceptometer measured did not come from a sample but instead came from the polycrystalline silver cold finger of the fridge. Some of the oscillations and their Fourier transform are shown in figure 7.4.

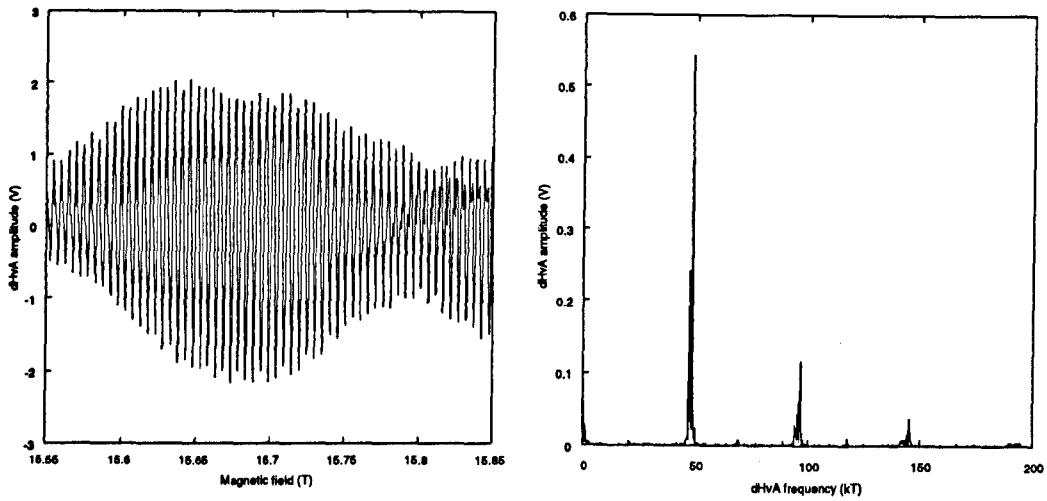

Figure 7.4: An example of dIIvA oscillations produced by the polycrystalline silver cold finger. Even though the silver is only weakly coupled to the coils, the belly oscillations are clearly visible up to the fourth harmonic where they are already heavily damped by the lock-in amplifier output filter.

The silver oscillations were a mixed blessing. They were testament to the sensitivity of the susceptometer and they were useful for various tests, such as measuring the time constant of the magnet, but they also prevented any smaller dHvA signals from being visible with respect to field. As the sweeps were invariably Fourier analysed and as silver provided such an effective thermal link, it was decided to leave the cold finger in place, although with hindsight it seems a good idea to replace its tip with an alternative material (see chapter 8).

7.6 Experiments using the secondary susceptometer.

A range of experiments were conducted on $CeCu_2Si_2$. The results are presented in chronological order to give a logical basis for each step. The first series of experiments conducted on this sample took place in the 8 T field of the demagnetisation magnet, whilst the main field was employed for a study on another heavy fermion, UBe_{13}.. The UBe_{13} experiment was inconclusive, showing what could have been dIIvA oscillations fractionally above the noise floor. It was decided that the $CeCu_2Si_2$ experiment would prove more fruitful. Some low frequency oscillations were observed (see figure 7.5), which were thought to be due to $CeCu_2Si_2$. They had a dHvA frequency of 200 T as opposed to the previously measured 150 T, but this difference was ascribed to misalignment of the crystal. There were also some higher frequencies visible. It might at first appear strange that earlier studies had discovered the 150 T frequency and not the others, although it must be born in mind that figure 7.5

shows results obtained by detection using the first harmonic, where signal amplitude is proportional to the dHvA frequency squared, whilst the conventional field modulation technique is performed at the second harmonic and is optimised for a finite frequency. An alternative interpretation, that became more evident later on, was that the oscillations could be an artefact of the experiment.

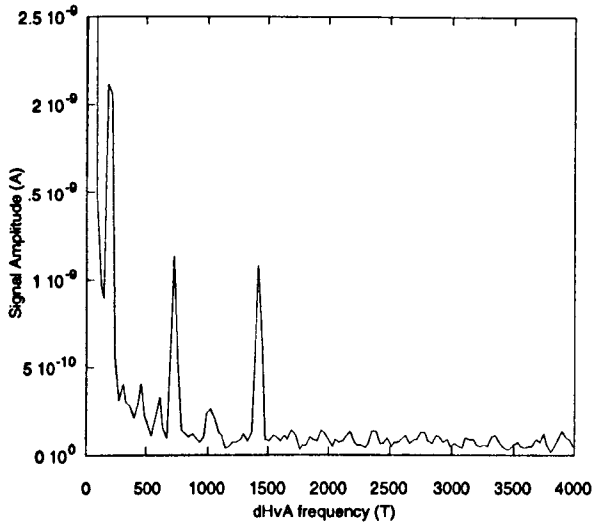

Figure 7.5: The dIIvA oscillations observed in the secondary susceptometer that were initially ascribed to $CeCu_2Si_2$. The field range was 6.2-7.8 T and the temperature is chosen to be 487 mK, to maximise the 1440 T peak.

These frequencies were rather low, compared with the size of the Brillouin zone (30 kT) and so would have corresponded to small sections of the Fermi surface and were therefore viewed as a fairly insignificant discovery. However, when an effective mass analysis was performed, an interesting property came to light.

Although the masses were invariably light, some unusual, non-L.K. behaviour was observed for the 1440 T frequency (see figure 7.6). On reducing the temperature the amplitude of the signal rises, as one would expect from the L.K. formula, but it has a maximum at around 0.7 K and then decreases with temperature eventually saturating at a finite value. A variety of models can be invoked to describe this behaviour, and are discussed in chapter 8. Because of the diversity of possible B/T phase diagrams, it was important to find the location of the A/B metamagnetic transition, in case one of the phases was the root of the decrease in signal. However, in spite of the great sensitivity of the susceptometer, no transition was observed at this stage (although this situation was remedied later).

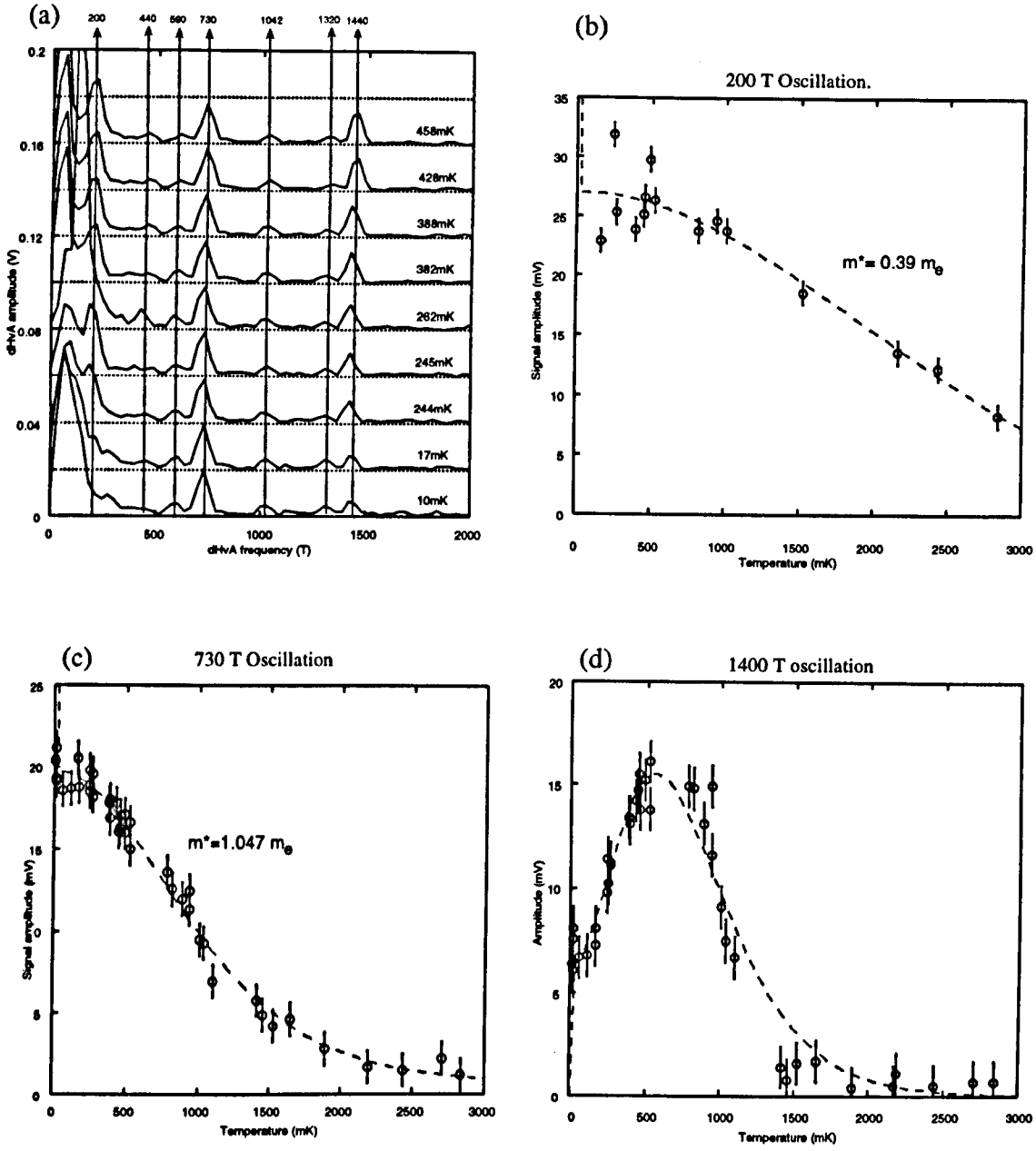

Figure 7.6: The results of the experiment conducted in the secondary susceptometer between 6.2 T and 7.8 T. (a) shows fast Fourier transforms over a range of temperatures. Note that consecutive Fourier transforms are shifted by a constant amount, for clarity. (b), (c) and (d) are mass plots for the prominent peaks. They were attempted for the others but the signal was too weak. Note the increased scatter on the 200 T mass plot at low temperatures arising from a more prominent background susceptibility. The 1400 T oscillation displays behaviour not expected from the L.K. formula.

7.7 Experiments using the main susceptometer.

It became clear that in order to study the crystal over a wider range of the B/T phase diagram it would be necessary to transfer it to the main magnet. Between these events was a period of four months, when repairs were made to our helium liquifier and alterations were made to the main magnet.

Another $CeCu_2Si_2$ crystal was placed in the secondary susceptometer. This sample had a plate like geometry so it was necessary to construct a larger coil to accommodate it. When experiments were attempted, a very large field dependent background susceptibility was found to be present, preventing any useful work being performed.

7.7.1 Field and modulation-frequency dependence of the background susceptibility.

With the original sample located in the main field, dHvA oscillations were not immediately visible, so some tests were conducted in order to optimise the system. The most prominent problem appeared to be that of the field dependent background signal. Its change with field was so large in magnitude that it was necessary to reduce either the modulation amplitude or the gain of the SQUID and lock-in. A possible solution to this problem was to use dynamic balancing, as outlined in chapter 5. In order to characterise the background susceptibility, some experiments were conducted with a very low modulation amplitude and without any electronic balancing (see figures 7.7 and 7.8).

It was immediately apparent, that there was a large phase change in the signal and a signal amplitude that possessed a paramagnetic peak. These features were found to depend upon the modulation frequency employed, with the paramagnetic peak shifting to higher fields if measured at a higher frequency. This property is discussed in chapter 8.

To investigate further the field dependence of the input circuit, its frequency response was examined over a range of magnetic fields, (see figure 7.9). Once more, anomalous behaviour was seen. A simple model would predict that the curves at different fields would have the same shape, and just be scaled relative to each other. One might expect small deviations due to the change in self inductance of the input coil as the susceptibility of the sample inside it changes, but it is not expected to be a large effect. The measured curves, on the other hand, displayed an unusual whale back shape and were clearly seen to have a form that was field dependent. One might question that this state of affairs is due in some way to the design of the input circuit, but this does not appear to be the case, because when one conducts the same experiments feeding a modulation signal into the electronic balancing coil (see figure 7.10), (which is similar to the input coil, but located away from the experimental region), one observes the characteristic bandpass response. Possible reasons why the pickup coil would respond in this manner are discussed in chapter 8.

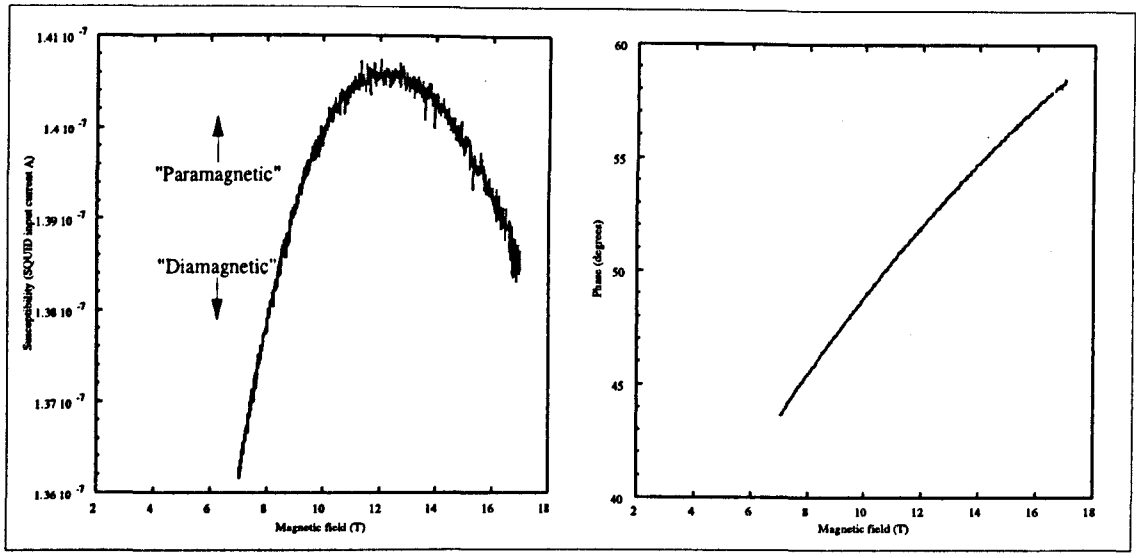

Figure 7.7: The susceptibility and its phase change with field for a 417 Hz modulation field, ($b_0 \approx 0.1\,\mu$T and SQUID gain $\times 10$). The labels paramagnetic and diamagnetic are identified by comparison to the superconducting transition in the $CeCu_2Si_2$ crystal and do not indicate any relation to zero susceptibility.

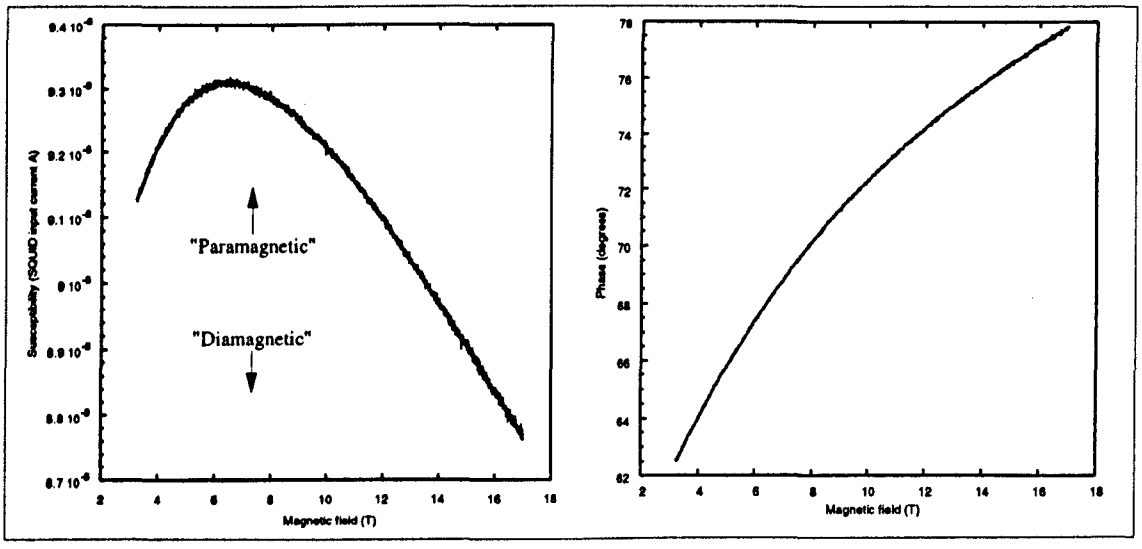

Figure 7.8: The susceptibility and its phase change with a 217 Hz modulation field, ($b_0 \approx 0.2\,\mu$T and SQUID gain $\times 100$).

Looking at figure 7.9, it might appear that the low frequency regions are far too noisy to use for experiments, however this is an artefact of the short time constant employed on the lock-in amplifier, and in fact it can be seen from the noise traces 5.17 and 5.18 (pages 51 and 52) there are regions of calm where one may employ phase sensitive detection if a suitably long time constant is chosen.

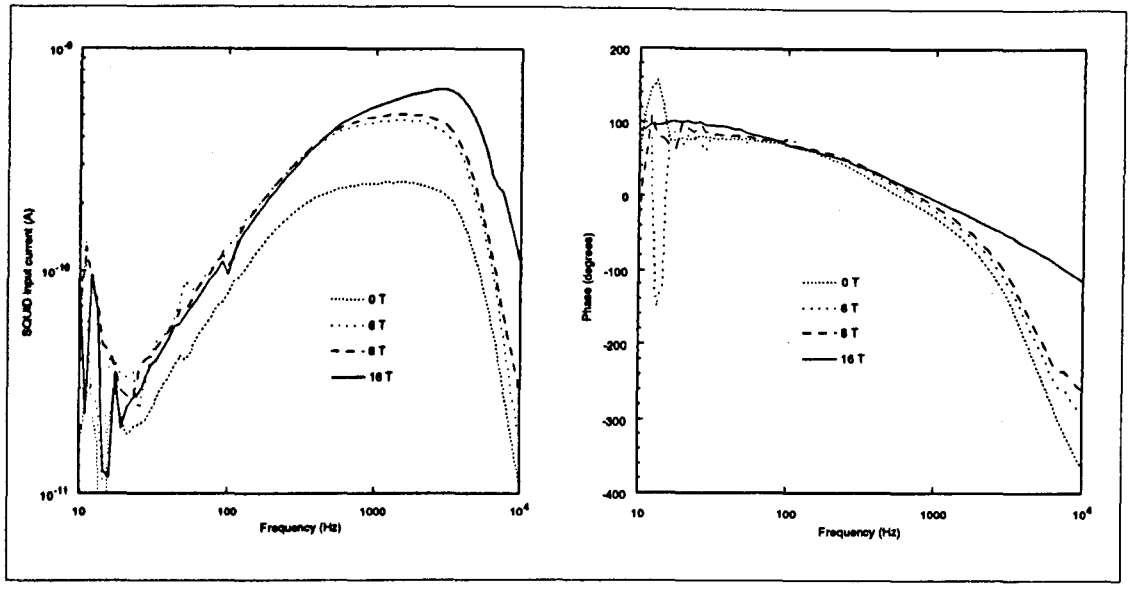

Figure 7.9: The frequency dependence of the amplitude and phase of the out of balance signal from a nominally balanced pickup coil with the $CeCu_2Si_2$ sample in it. The field applied was $4 \times 10^{-8} T_{RMS}$. The form is not as one would expect considering a simple L-R circuit. Also note the effect of the superconducting crystal at 0T. Both these features are discussed in chapter 8.

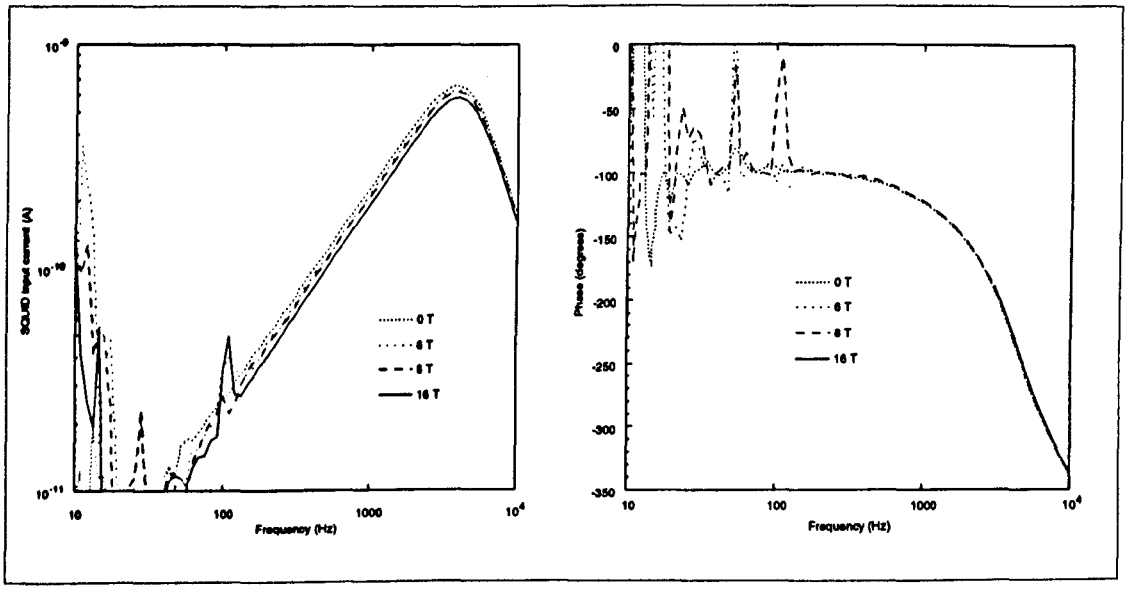

Figure 7.10: The frequency dependence of the amplitude and phase of a signal resulting from a modulation field applied to the electronic balancing coil. The anomalous features of figure 7.9 are seen to be absent.

7.7.2 dHvA oscillations below 2 kT.

By choosing a modulation frequency where the field dependence of the signal amplitude was reduced (83 Hz as opposed to 417 Hz) and by employing dynamic electronic balancing of the signal phase, it became possible to observe the dHvA oscillations again, although it was apparent that the dHvA frequencies were different to before (see figures 7.12 and 7.13).

This was originally attributed to a shift in the alignment of the crystal. Indeed, aligning the crystal is currently an imperfectly solved problem. One can align the crystal using a goniometer and an x-ray machine, but to then mount the crystal on the cold finger involves using only the shape of the crystal as a reference to its orientation. One can envisage some arrangement where a small stage could be designed to bolt on both the goniometer and the cold finger, but probably the most reliable solution would be to design a fully rotating sample holder. One could then look for symmetry directions in the dHvA oscillations.

It will be seen shortly that in fact these oscillations were a remnant of the experiment, and this explains not only the shift in frequencies but also why they were so indistinct and why the relative amplitudes of the oscillations were field dependent.

An experiment was also performed over a very long field range to resolve the low frequency oscillations (see figure 7.11).

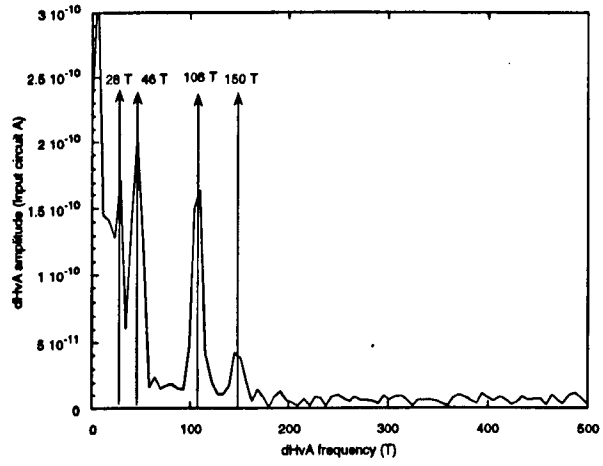

Figure 7.11: dHvA oscillations for a field sweep between 4.3 T and 13.2 T at a temperature of 16 mK. The absence of higher frequencies is due to the lock-in filter.

It became evident that there was far more structure at low frequencies than originally anticipated. A small peak is clearly visible at 150 T, where the $CeCu_2Si_2$ oscillation was observed in the conventional susceptometer. It could be argued that this is just the third harmonic of the 46 T oscillation (as the frequency resolution of this FFT is just 6 T). One would then require the second harmonic to either be the peak at 106 T or be obscured by it. This is again possible within the resolution of this FFT. It will be seen in the next chapter that the 150 T oscillation is of a suitable order of magnitude to come from the $CeCu_2Si_2$ crystal.

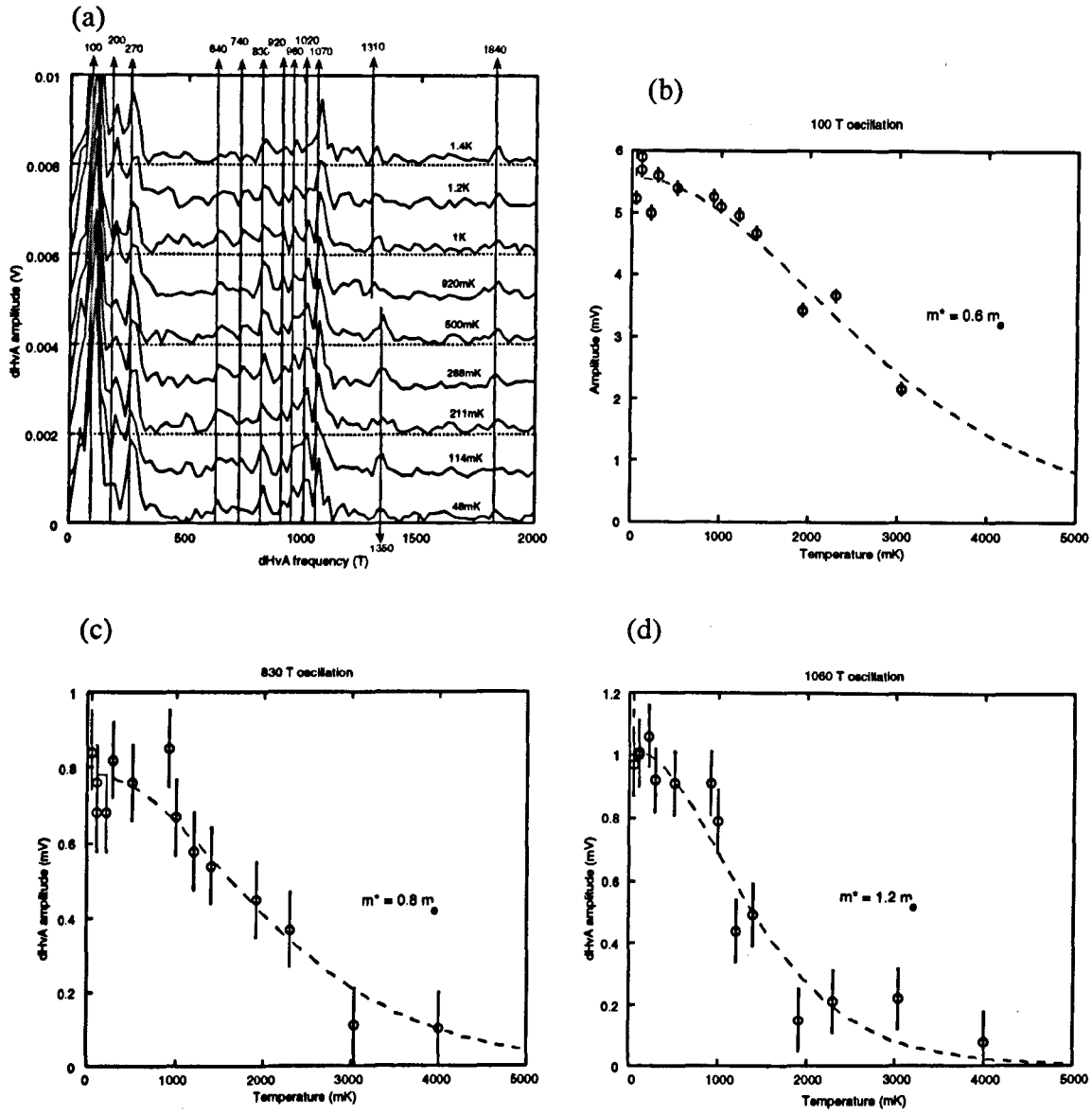

Figure 7.12: The oscillations observed between 8.7 and 14.5 T in the main field susceptometer. The mass curves are displayed for those oscillations that produced clean enough signals. The oscillations are shifted relative to those seen in the secondary susceptometer and are less distinct.

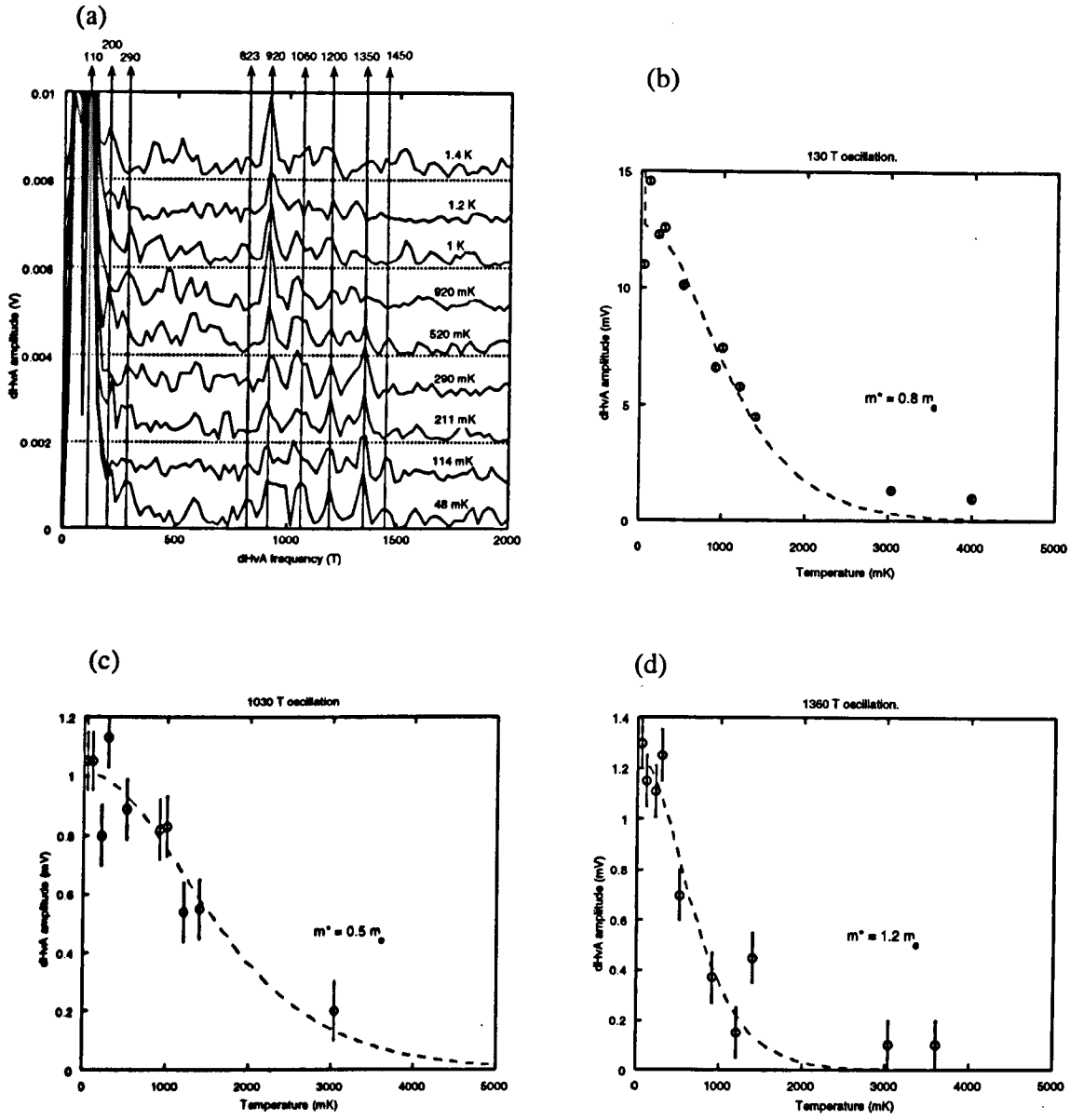

Figure 7.13: The oscillations observed between 5 and 6.5 T in the main field susceptometer. The mass curves are displayed for those oscillations that produced clean enough signals. Note that different frequencies are prominent compared to those in the higher field experiment shown in figure 7.12.

7.7.3 The metamagnetic transition.

Out of curiosity, an experiment was conducted with the susceptometer running in pulsed field mode. In this configuration no modulation field is applied, and the SQUID output is logged directly whilst the main field is swept rapidly. Although no dHvA oscillations were visible, the metamagnetic transition was now distinguishable (see figure 7.14).

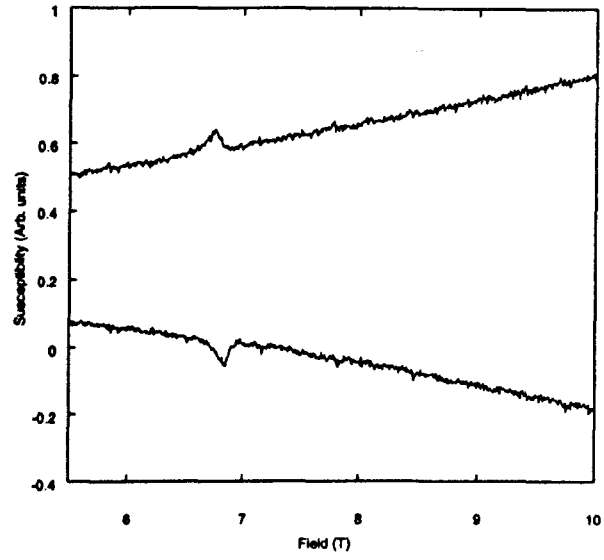

Figure 7.14: Pulsed field experiment with the sweep rate 0.693 T/min, a SQUID gain of 500 and a low pass filter of 1 Hz. The two traces correspond to an up sweep (below) and a down sweep (above). The metamagnetic transition is clearly visible.

It is initially surprising that any feature could be visible using this mode of operation and not using the field modulation technique. This unusual result is discussed in the next chapter. The B/T phase diagram was then plotted out using the pulsed field technique (see figure 7.15).

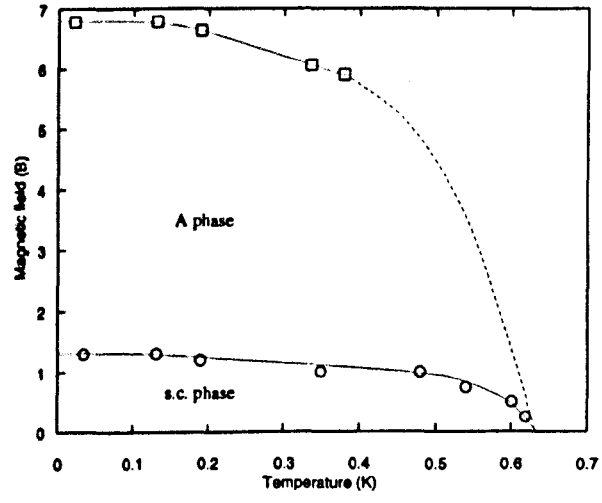

Figure 7.15: The B/T phase diagram of $CeCu_2Si_2$ measured using the pulsed field technique. The metamagnetic transition becomes indistinct above 400 mK so the dashed line is only drawn from analogy to experiments on other crystals measured by the Darmstadt group using magnetoresistivity.

The phase diagram shows the characteristics of the A/S-type crystal. It was then clear that the anomalous behaviour observed previously, overlapped three regions of the B/T phase diagram (if one assumes that phase B is present). Some traces were performed between 6 and 8 tesla to see whether any anomalous behaviour was still present (for any oscillations) but all the measurable peaks displayed the classic L.K. behaviour.

7.7.4 High frequency oscillations.

Locating the sample in the main field also allowed ultra low temperatures to be achieved. It was possible to choose base temperatures by demagnetising (and remagnetising) to an appropriate field. It is inadvisable to introduce heat to achieve any temperature change, because the former method always guarantees that the demagnetisation stage possesses its maximum heat capacity. When the sample was cooled to 3 mK, two new oscillations were visible (see figure 7.16).

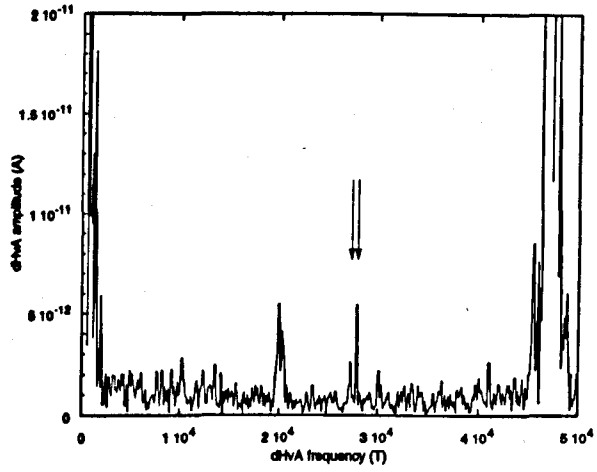

Figure 7.16: Fourier transform of a field sweep between 13 and 15 T at 2.8 mK. The oscillations that were originally attributed to $CeCu_2Si_2$ are at 27,250 T and 27,850 T. The oscillations at 20,000 T and and 47,000 T are explicable in terms of silver.

They were much smaller than the others and hence were only visible due to the improved noise characteristics resulting from slower sweeps. Mass plots for the two peaks are displayed in figure 7.17.

Initially the effective mass for the 27,250 T oscillation appeared to be over $100\,m_e$ because of an observed dip in amplitude at low temperatures, but with further experiments it seems that this was a statistical anomaly. A quantitative analysis of the effective mass was not possible due to the a rising noise background. The origins of this noise are not thought to be Johnson noise, but rather instabilities in the fridge when it is not running at its base temperature, because the noise was intermittent. A minimum magnetic field of 0.5 T was always left in the demagnetisation magnet so that the demagnetisation stage retained a large heat capacity, and also because this appeared to minimise the vibrational noise visible in the main field susceptometer.

A Dingle-like plot was also attempted (see figure 7.18). It was not possible to fit directly to the raw data so each trace had to be divided into sections and then Fourier analysed. The experiments were performed at 20 mK as this was an easily achievable and stable temperature. Traces were as long

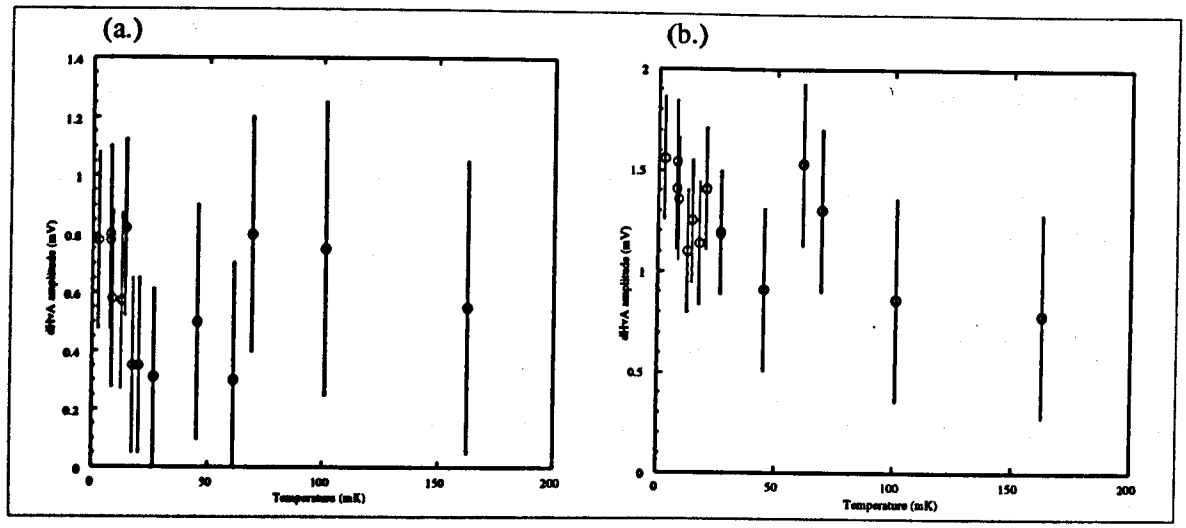

Figure 7.17: Mass plot for (a.) the 27,250 T oscillation and (b.) the 27,850 T oscillation.

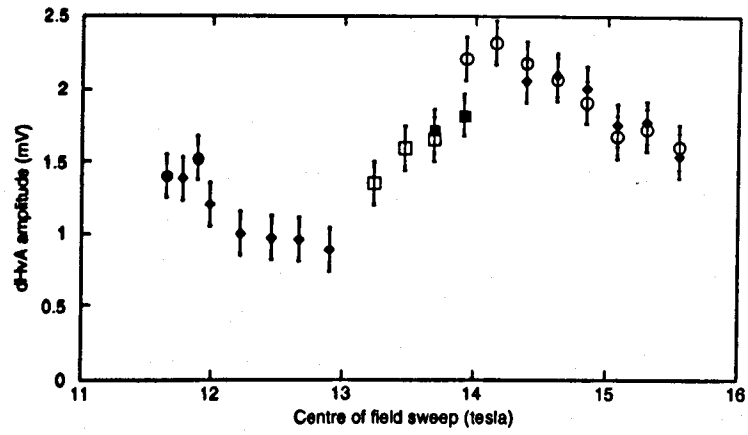

Figure 7.18: Plot of amplitude versus field for the 27850 T oscillation. Each symbol represents a different sweep. In some of lower field sweeps, the lock-in amplifier filter function was not negligible and allowance has been made for this by multiplying by the integral of the reciprocal of the filter function with respect to field.

as possible although there was inevitably a compromise between this, the number of points collected and the Nyquist criteria. Each trace was cut into sections of 0.01 T^{-1}, which is equivalent to the field between 13 and 15 tesla. The centre of each section is known to a resolution smaller than the size of the points on figure 7.18 although it should be born in mind that the amplitude results from contributions either side of this point, producing a low pass filtering effect. It can be seen that figure 7.18 does not have the familiar exponential rise in amplitude, and this effect appears to be obscured by a beat pattern. To ensure that the effect is genuine, the sweeps were repeated over a range of fields and each symbol corresponds to a different experiment. It would have been desirable to obtain enough of the field regime to try and fit a Dingle plot to it, but a small leak resulted in the fridge becoming blocked, so it had to be warmed up. The importance of conducting reference tests without a crystal and the long timescale involved in these experiments, made this an apposite time to remove the crystal.

7.7.5 Background tests.

Usually one would conduct background tests before attempting any other experiments. This procedure was not followed here, because a previous r.f. susceptometer experiment located on the same cold finger showed only the large silver belly oscillations and these were not thought to present a problem. Also, most of the optimisation of the susceptometer was accomplished in the months while the $CeCu_2Si_2$ experiments were being performed, so any small background signals would not have been visible in an initial experiment. These factors, coupled with the long thermal cycling times whenever the sample is changed, resulted in the background tests only being performed last.

As there was some doubt about how precisely oriented the crystal was, when the fridge was warmed up the tail was removed in its entirety and the crystal was x-rayed *in situ* using the Laue back-scattering method. It was confirmed that the crystal was aligned to within 2° along the a-axis.

Experiments were then rerun in both experimental regions with the crystals removed. To extract the crystals, the silver paste was softened with solvent but care was made not to wash it away. The results for the secondary susceptometer were encouraging, showing no sign of the characteristic oscillations for the same experimental parameters (see figure 7.19).

When tests were performed in the main field susceptometer the oscillations were still present (see figures 7.20 and 7.21). This was initially a very shocking result because the majority of the oscillations possessed frequencies which were unattainable by silver. The most notable of these were the very low frequencies, visible in figure 7.20 b. Part (c.) shows a Fourier transform with respect to time. The absence of clear peaks on this trace suggests that the oscillations were genuine dHvA.

It was then remembered that a previous group member had experimented with attaching samples, using indium as a solder. Information from him, revealed that indium had been used in both experimental regions but effort had been made to remove it afterwards. To resolve whether any indium was present, microscopic analysis was attempted.

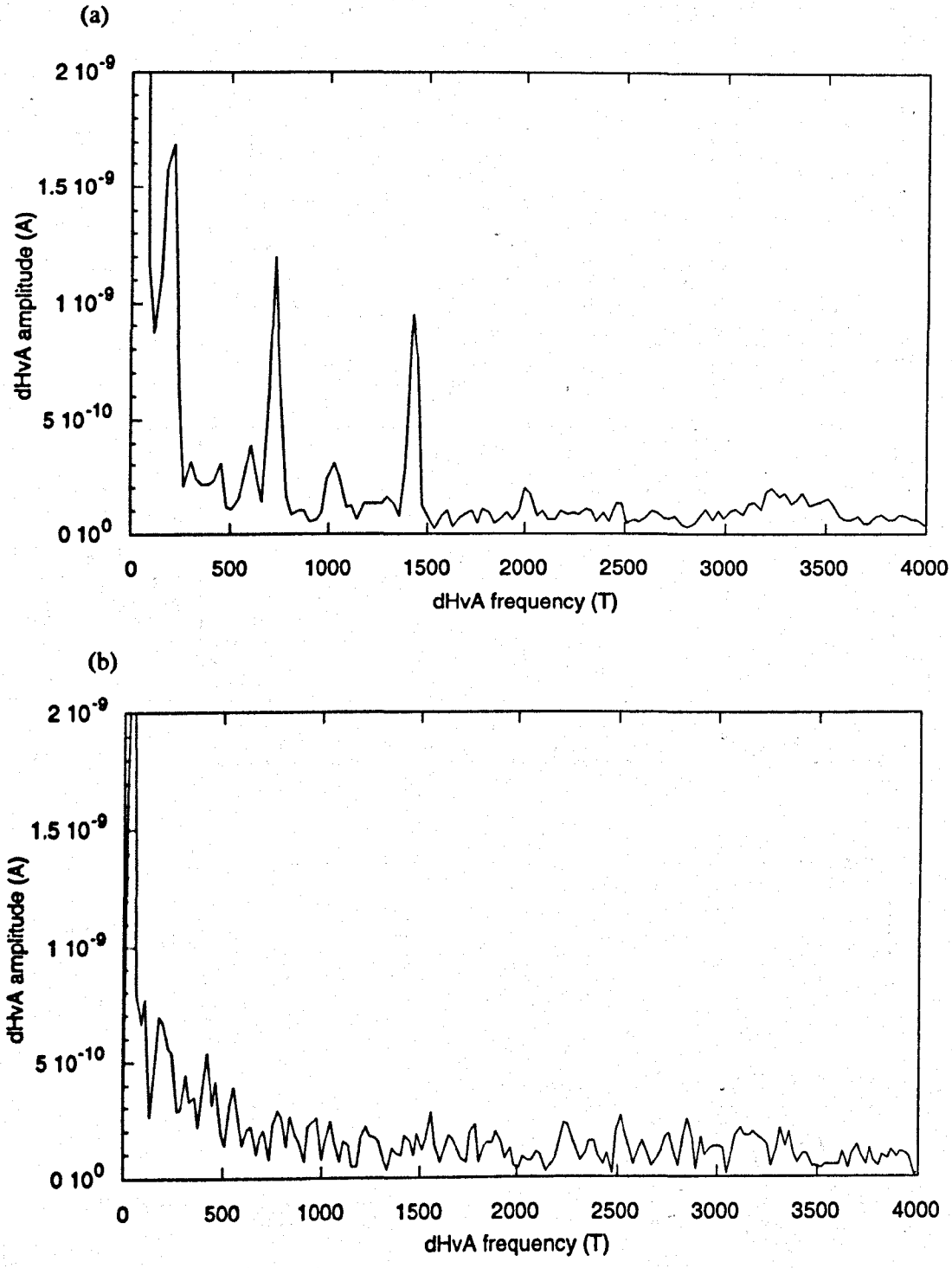

Figure 7.19: Comparison of the oscillations measured by the secondary susceptometer in field sweeps measured between 6 T and 8 T, (a.) with the crystal present and (b.) with the crystal removed. It should be noted that the pickup coil was changed between experiments.

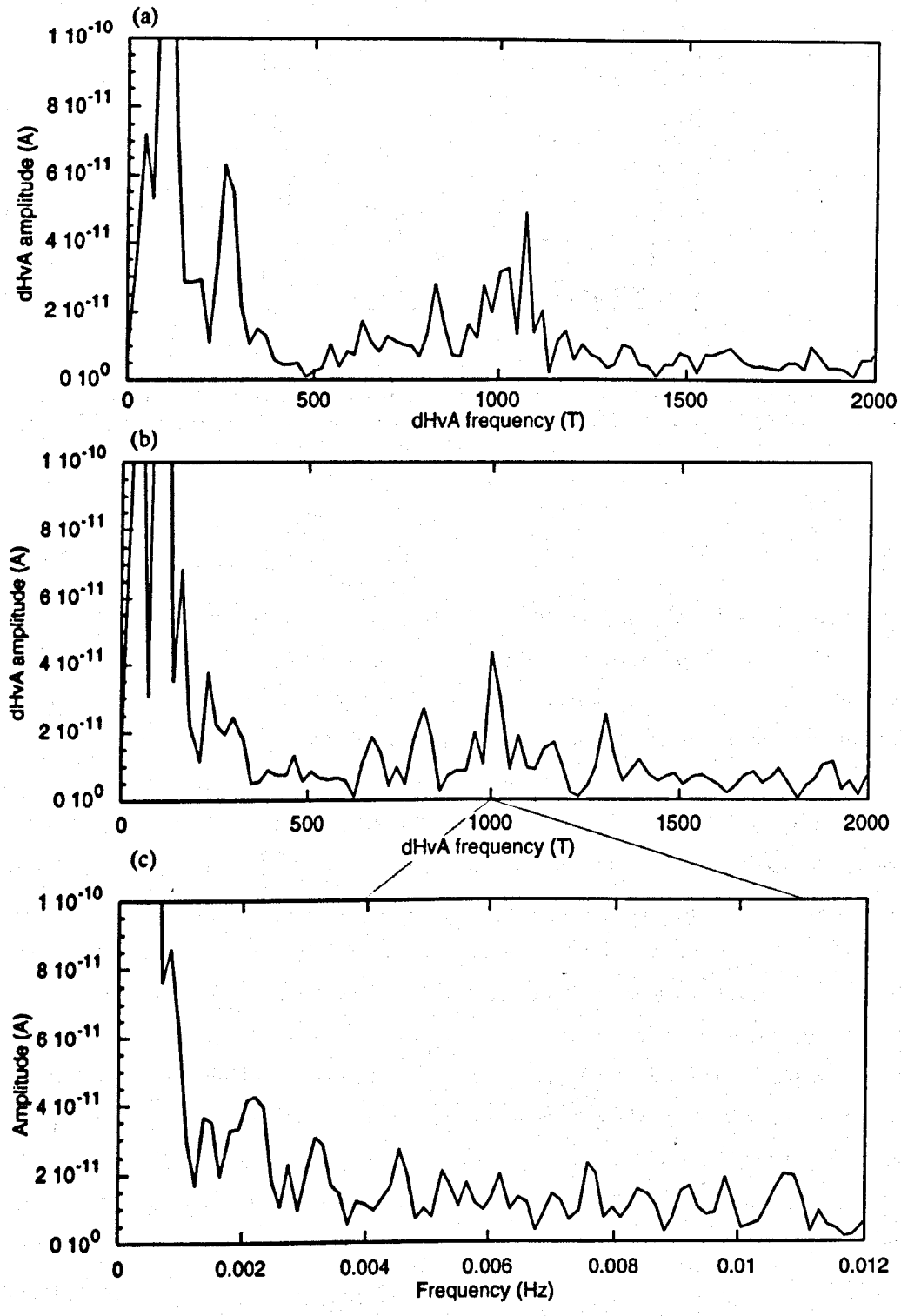

Figure 7.20: Comparison of the oscillations measured by the main field susceptometer in field sweeps between 14.5 T and 8.7 T. (a.) With the $CeCu_2Si_2$ crystal present. (b.) Without the $CeCu_2Si_2$ crystal. (c.) Without the $CeCu_2Si_2$ crystal, analysed with respect to time. The lines indicate the equivalent real time frequencies at either end of the field sweep.

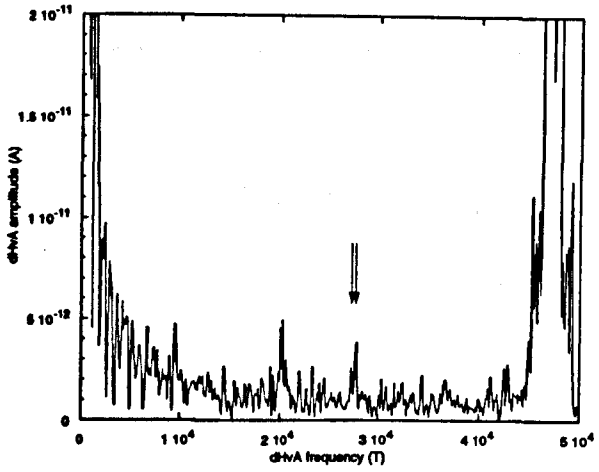

Figure 7.21: Fourier transform of a field sweep between 13 and 15 T with the sample removed. The oscillations that were originally attributed to $CeCu_2Si_2$ at 27,250 T and 27,850 T are still clearly visible.

7.7.6 Microscopic analysis.

The silver sample mount was analysed using Energy Dispersive X-Ray Analysis (EDX) installed on a JEOL 6400 Scanning Electron Microscope (SEM). In this technique, high energy electrons in the SEM beam impinge on the sample, so atomic electrons are excited from the K, L and M shells into the continuum of empty states above the valence or conduction bands by inelastic interaction. Chemical analysis is achieved by counting the number of x-rays, of specific energies, emitted as electrons return to these unfilled states. The detector is a liquid nitrogen cooled silicon crystal. Collimated x-rays entering the detector, excite electron-hole pairs in the silicon. The number of pairs produced is proportional to the x-ray energy and appears as a pulse at the electrodes of the detector. A multichannel analyser is used to amplify and process every pulse, allowing rapid data collection.

The silver post was gently cleaned with acetone and ethanol, so that any trace of silver paste was removed. The EDX analysis of the region on which the sample was mounted is shown in figure 7.22 a. The largest peak was seen to correspond to the indium $L_{\alpha 1}$ line at 3.487 keV. This was not totally conclusive proof of the presence of indium because that frequency also corresponds to the silver $L_{\beta 2}$ line, although this line is never usually observed to be more intense than the silver $L_{\alpha 1}$ line. When a different part of the cold finger was tested, which was known to have never been exposed to indium, the peak in question was dramatically reduced, so there is strong indication that indium was present in the experiments.

A quantitative value for the volume of Indium is not available using EDX but fortunately it was possible to identify the region of indium under an optical microscope due to its slightly duller grayer colour.

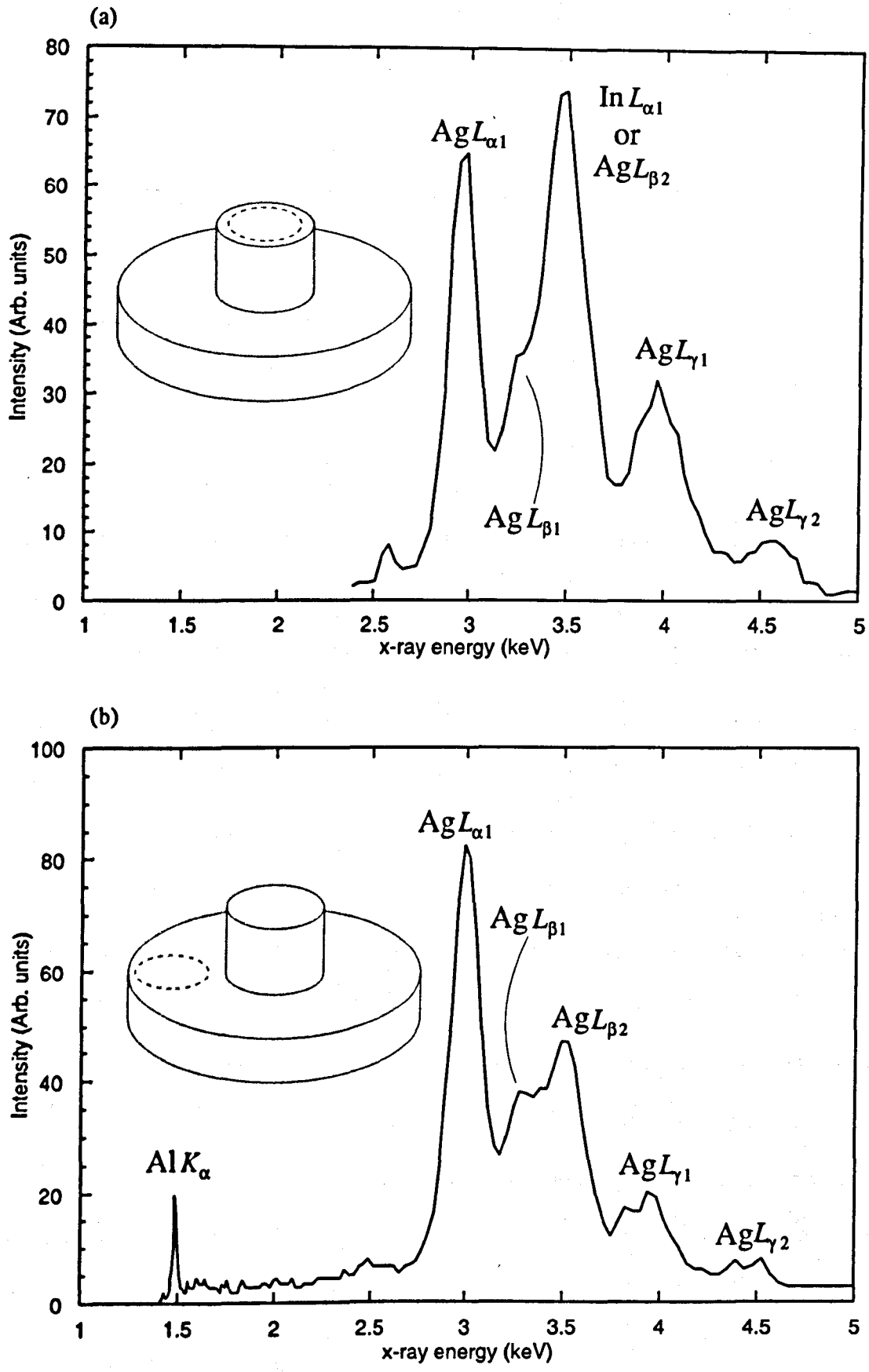

Figure 7.22: Energy dispersive x-ray analysis spectra of the tip of the cold finger, for (a) The location where indium is suspected of being present and (b) a clean reference part of the cold finger.

Chapter 8

Discussion.

8.1 Introduction.

The results displayed in the previous chapter left many unanswered questions and it is the purpose of this chapter to give a quantitative analysis of these observations. There are very few clear cut inferences that can be made, and many of the points raised in this chapter will rest upon more than one experiment. For this reason a large amount of cross referencing to earlier sections is unavoidable.

Firstly, there arises the question of why the background susceptibility displayed an unusual variation with field and modulation frequency. A model will be presented that calculates the effect of the silver r.f. shielding surrounding the sample, and the silver post onto which the sample was attached. These combined effects qualitatively account for the observed behaviour. The observation of the $CeCu_2Si_2$ superconducting transition is then used to provide a calibration of the sensitivity of the susceptometer.

The next question to address is the origin of the observed oscillations. Calculations will be presented which suggest that a combination of the silver post onto which the sample was mounted, and indium contaminants, are sufficient to explain the amplitudes and frequencies of all the observed oscillations. A discussion will also be presented as to whether genuine $CeCu_2Si_2$ oscillations were seen. Constraints are put on the range of possible Dingle temperatures and effective masses, which are not immediately explicable in terms of the observed linear contribution to specific heat for $CeCu_2Si_2$. Various reasons for this will be presented.

Some of the oscillations that were observed also showed unusual field and temperature variation. The strange low temperature dip in the amplitude of the 1,400 T oscillation (observed in the secondary susceptometer) is interpreted with a range of models, the most favoured of which pictures an interference effect arising from a dHvA oscillation and the second harmonic of a lower frequency. The oscillatory field variation in the amplitude of the 27,850 T frequency is discussed as arising from magnetic interaction in indium, as has been observed previously [72].

Another puzzling aspect of the experiment is the fact that the metamagnetic transition between

the A and B phases of $CeCu_2Si_2$ was only observed when the experiment was performed in pulsed field mode and not using the field modulation technique. This fact is interpreted by proposing that the magnitude of the susceptibility peak at the metamagnetic transition is sweep rate dependent.

This chapter closes with a comparison of the sensitivities of the the SQUID susceptometer and a conventionally amplified susceptometer. Finally, modifications are proposed that could boost the sensitivity of the SQUID susceptometer.

8.2 The background susceptibility.

Before discussing the oscillations that were observed in this experiment, it is worth considering the background susceptibility in detail. The reasons for this are twofold - The behaviour that was observed does not correspond to what one might have first expected, and so must be explained if we are to have confidence in these and any other results observed with the susceptometer. Also, by studying the background susceptibility we can gain insight into the sensitivity of the susceptometer.

Comparison of figures 7.9 and 7.10 (page 79) shows that when a signal is injected into the electronic balancing coil the expected filtering response is produced, however when the signal is provided by the modulation coil, an anomalous frequency dependence is seen. Further unusual behaviour is visible in the field dependence (figures 7.7 and 7.8 on page 78). The signal can be interpreted as a sample with a susceptibility which is seen to possess a paramagnetic peak with respect to magnetic field. The location of the peak depends upon the frequency of the modulation field, and is found at higher fields when higher frequencies are used.

In short, the diamagnetic character becomes apparent at higher fields and lower frequencies. Variation with frequency and field suggests that a skin depth effect might be active, however if one calculates the skin depth for the $CeCu_2Si_2$ sample, estimating its resistance to be $4 \times 10^{-8}\,\Omega$m, and using the equation

$$\delta = \left(\frac{2\rho}{\mu_0 \omega}\right)^{\frac{1}{2}} \tag{8.1}$$

where ρ is the resistivity, and ω is the angular frequency of the applied modulation field, one finds that even up to frequencies of 700 Hz ($\omega = 4.4 \times 10^3$) the skin depth is still 4 mm which is in excess of the sample size, so this is probably not the cause of the effect. The silver cold finger, alternatively, will possess a resistivity of around $2 \times 10^{-10}\,\Omega$m producing a skin depth of 0.3 mm, which might be of great relevance. This idea is confirmed by the fact that the characteristic background behaviour was still present when the sample was removed, and that this unusual behaviour was not observed when a signal was injected into the electronic balancing coil, which is isolated from the experimental region.

The principle problem in producing a satisfactory model, is to account for the fact that the susceptibility does not change monotonically with field or frequency, so that no single diamagnetic or paramagnetic effect can explain this result. One way of producing this characteristic curve is to have a diamagnetic response that increases with field and a paramagnetic response that also increases but

then saturates. A possible cause of this, is the present coil arrangement (see figure 8.1), where large pieces of silver are located in the field and the sample is surrounded by a 0.25 mm thick silver shield, which will screen it.

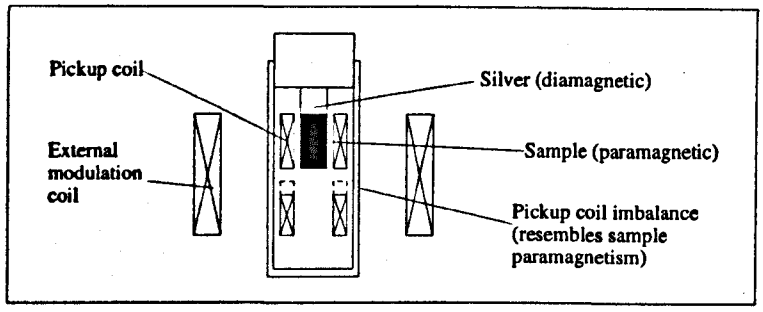

Figure 8.1: Sketch of the contributions to the apparent susceptibility in the main field susceptometer.

As the field increases, so will the magnetoresistance of the silver and thus so will the skin depth. The bulk silver is large compared with the skin depth so its diamagnetic contribution will increase monotonically. The thickness of the silver shield is comparable with the skin depth, so the paramagnetic contribution from the sample and any coil imbalance will level off when the skin depth appreciably exceeds the thickness of the shield.

As a preliminary test of this idea, one can see what effect the skin depth has on the frequency response. We assume that the dominant contribution to the signal is due to the imbalance of the coils (which is justified later in this section). By modelling the attenuation of the signal reaching the coil by $\exp(t/\delta(\omega))$, where $\delta(\omega)$ is the frequency dependent skin depth of silver, given by equation 8.1 and t is the thickness of the silver shield, one obtains the dependence depicted in figure 8.2(b). If one multiplies the (well understood) frequency dependence of the electronic balancing coil (part (a)) by the attenuation factor, one obtains a dependence (part (c)) that bears a striking resemblance to the input coil behaviour shown in figure 7.9 on page 79.

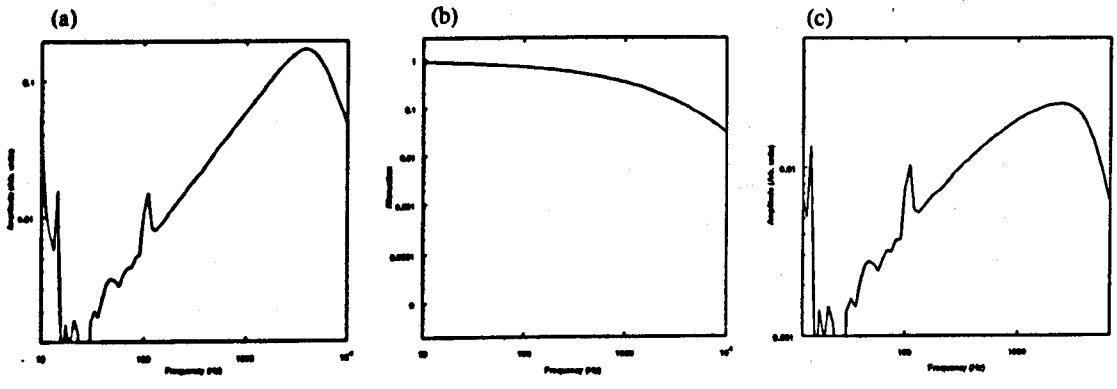

Figure 8.2: Model of the effect of screening due to the silver shield, on the frequency response of the SQUID input. (a) The frequency response measured by the electronic balancing coil. (b) The estimated attenuation due to screening by the silver shield. (c) The product of a. and b.

To model the field dependence shown in figures 7.7 and 7.8 (page 78), the diamagnetic contribution from all the silver in the vicinity of the pickup coil must be considered. For simplicity, the silver is modelled as a cylinder of radius, r=5 mm and height, h=5 mm. These dimensions are large compared to the skin depth so the fraction of the volume that contributes to the diamagnetic susceptibility is estimated to be given by $2\pi rh\int_0^\infty \exp\left(\frac{-x}{\delta(H)}\right)dx$ which reduces to $2\pi rh\delta(H)$ by the well known integral relation. We are now considering the field dependence of the skin depth due to magnetoresistance $\rho(H)$, which we model as $\rho(H) = ((2\times10^{-10}) + (2\times10^{-11})H)\,\Omega$m, assuming the linear rise in magnetoresistance which one associates with a polycrystalline sample. The susceptibility of silver is taken as -2.39×10^{-5} (dimensionless SI units) [73].

The paramagnetic contribution of the silver is modelled as before except now we consider the effect of field on the screening by $\delta(H)$, rather than $\delta(\omega)$. The susceptibility of $CeCu_2Si_2$ at these temperatures is 1.63×10^{-3} [74]. The volume of the $CeCu_2Si_2$ sample is again taken to be 5.25 mm^3. The coil imbalance is modelled as a constant, Θ.

The total susceptibility is therefore

$$(V_{sample}\chi_{sample} + \Theta)\exp\left(\frac{-t}{\delta(H)}\right) - \chi_{silver}2\pi rh\delta(H) \tag{8.2}$$

The calculated field dependence is shown in figure 8.3, for the measured frequencies of 217 Hz and 417 Hz. It can be seen that the general properties of the field and frequency dependence are explained although the exact quantitative dependence is not producible. This is presumably due to the approximations made in this calculation, such as the form of the magnetoresistance. In fact the linear increase in resistance with field is not valid over all field regimes and it begins to saturate at higher fields [75].

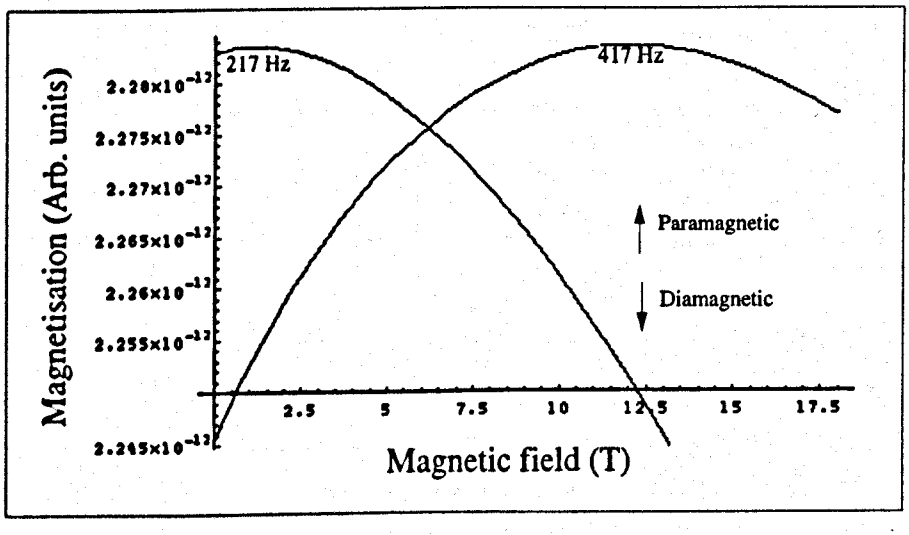

Figure 8.3: The predicted susceptibility based on equation 8.2, for the frequencies of 217 Hz and 417 Hz. This plot can be compared with figures 7.7 and 7.8.

8.2.1 The superconducting transition.

Another notable feature of figure 7.9 is the reduction in signal amplitude at 0 T. This is due to the sample going superconducting. It should be noted that although the superconducting transition changes the signal amplitude dramatically, it does not change the phase of the signal by 2π (from paramagnetic to diamagnetic). It therefore indicates that our initial assumption that the majority of the imbalanced signal comes from unbalanced coils, is well justified.

The diamagnetic contribution can also provide an exact value for the *minimum* sensitivity of the susceptometer. By assuming that all the sample displays the Meissner effect and possesses a susceptibility of -1, it is possible to calculate a conversion from susceptibility to SQUID input current. The approximation of 100 % of the sample displaying the Meissner effect should be a good one for a pure single crystal such as this, rather than a Meissner fraction of 30 % measured by Steglich *et al.* [55] in the original superconductivity study on a polycrystalline sample.

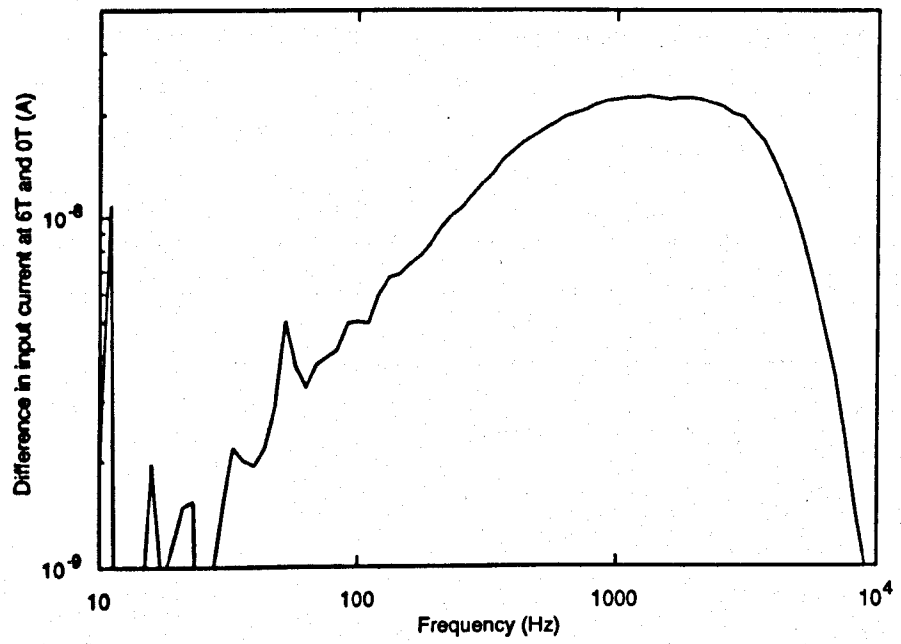

Figure 8.4: The difference in the SQUID input current when the sample is superconducting and when it is normal.

Figure 8.4 shows the susceptibility measured at 6 T (normal state) minus that measured at 0 T (superconducting state). The y-axis has been calculated to display the current entering the pickup coil of the SQUID. In going from the superconducting to the normal state, the susceptibility changes from -1 to 1.63 $\times 10^{-3}$, which can be approximated as a change of 1. Being a type-II superconductor, it is necessary to assume that the 6 T curve is above B_{c2}, which is seen to be the case from the B/T phase diagram (figure 7.15). It is also necessary to assume that the nominal 0 T sweep is below B_{c1}. Any remnant magnetic field in the main solenoid is estimated to be less than 0.005 T. The value of B_{c1} can be calculated from the measured value of B_{c2} (1.2 T) using the relation

$$B_{c2} = \sqrt{2}\kappa B_{c1} \tag{8.3}$$

where

$$\kappa = \frac{\lambda}{\xi} \tag{8.4}$$

where λ is the superconducting penetration depth and ξ is the coherence length. Using the measured values [76] of $\lambda = 4.5 \times 10^{-7}$ m and $\xi = 8.9 \times 10^{-9}$ m, gives $\kappa = 50$, which is in good agreement with the value calculated from the gradient of B_{c2} in the same study. We therefore expect B_{c1} to be 0.017 T, and so in excess of any remnant field.

Referring to equation 5.1, the current entering the SQUID, i, is given by

$$i = K(f)v = -K(f)S(f)cV\frac{dM}{dt} = -K(f)S(f)cV\chi h_0\omega\sin(\omega t) = \frac{-K(f)S(f)cV\chi h_0\omega}{\sqrt{2}} \tag{8.5}$$

where $K(f)$ is the I/V transfer function of the input circuit, v is the voltage generated in the input circuit, $S(f)$ is the attenuation due to screening, c is the coil coupling constant, V is the sample volume, χ is the sample's susceptibility and M its magnetisation. The simplification carried out in the third term assumes that the variation of M with H is linear.

One can then simply calculate

$$\frac{i}{\chi h_0\omega} = -\frac{K(f)S(f)cV}{\sqrt{2}} \tag{8.6}$$

for the time averaged signal. For this part of the experiment, the lock-in gain was ×50, the SQUID gain was 1.49 $\times 10^7$ V/A and the modulation field was 0.04 μT. This value is shown in figure 8.5.

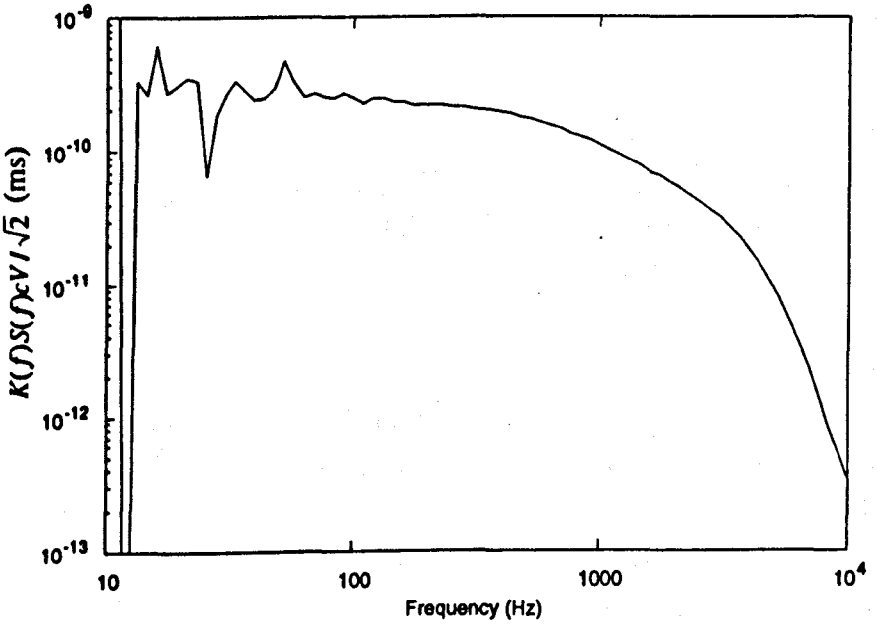

Figure 8.5: The measured value of $-\frac{K(f)S(f)cV}{\sqrt{2}}$, assuming a perfectly diamagnetic sample. Note $-\frac{K(83)S(83)cV}{\sqrt{2}} = 2.7 \times 10^{-10}$ms.

In this way it is possible to have a good estimate for the sensitivity of the susceptometer even though the contributing terms $K(f)$, $S(f)$, c and V are not known independently to such precision.

One can follow exactly the same procedure for the secondary susceptometer, only here the filter response is not attenuated by a shielding term, and obtain the value of $-\frac{K(f)cV}{\sqrt{2}}$ displayed in figure 8.6

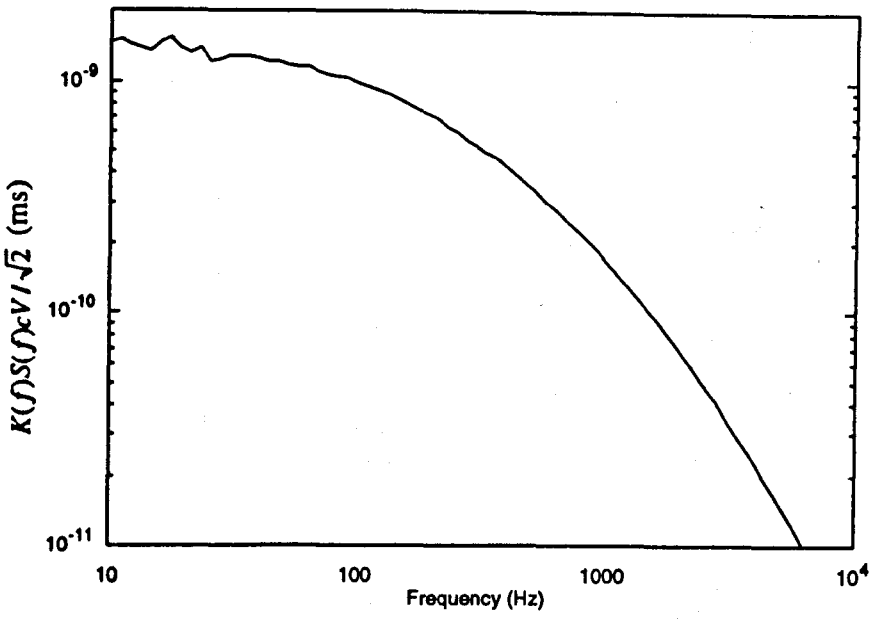

Figure 8.6: The measured value of $-\frac{K(f)cV}{\sqrt{2}}$, assuming a perfectly diamagnetic sample, for the secondary susceptometer. Note $-\frac{K(717)cV}{\sqrt{2}} = 2.4 \times 10^{-10}$ms.

8.3 Origin of the observed oscillations.

A range of oscillations were observed in both dHvA susceptometers. The experiments conducted in the main field will be discussed first, because their interpretation is slightly more transparent than that for the secondary susceptometer.

Figure 7.20 (page 88) shows clearly that the oscillations were still present in the main field susceptometer when the sample was removed, so the first topic to address is their origin. The most prominent oscillations observed were those at 46,400 T and 47,764 T (figure 7.4). Due to their frequencies, they almost certainly originated from the belly orbit of the silver post onto which the sample was attached and the silver paint which was used to make thermal contact (see figure 8.7). To ensure that this is the case, and to provide confirmation of the system sensitivity, it is worth checking how small the silver could be and still provide the measured signal.

We do not have a direct measure of how strongly coupled the silver is to the input coil, but the measurement of $-\frac{K(f)S(f)cV}{\sqrt{2}}$ in section 8.2 lends confidence to the calculated input impedance of the SQUID input circuit, so it just remains to calculate the coupling constant to the input coil. This is displayed in figure 8.8 for a point dipole at a range of positions.

The coupling of the silver to the coil will be reduced, but not too significantly because the end of the post is adjacent to the edge of the coil. From figure 8.8 we can see that coil coupling constant, c, will be $1.9 \times 10^{-3}\,\Omega m^{-2}s$ as opposed to $3.2 \times 10^{-3}\,\Omega m^{-2}s$ for the maximal position.

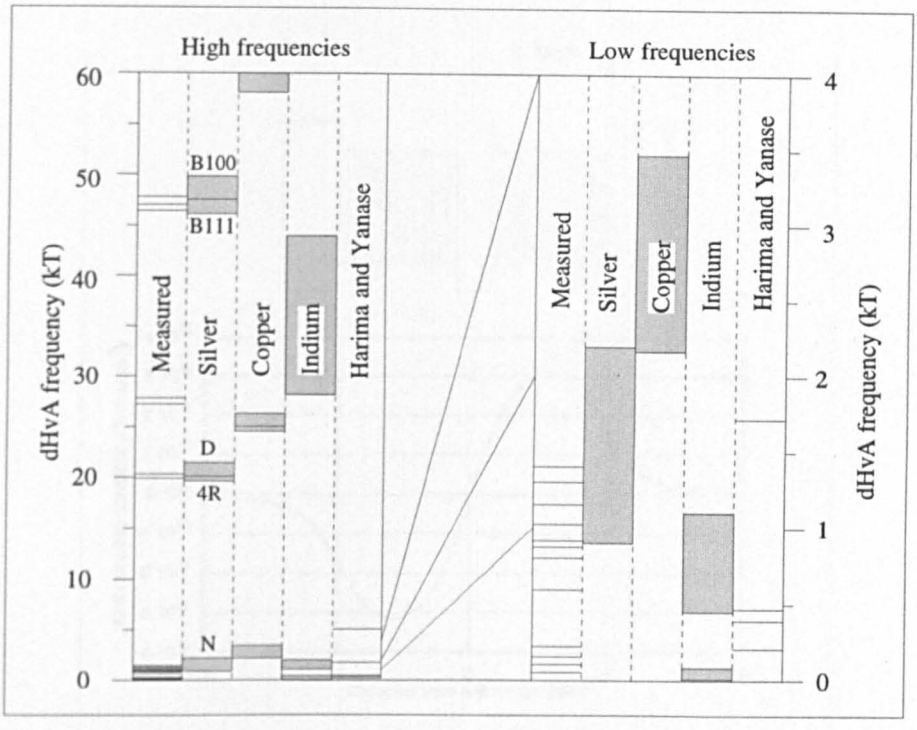

Figure 8.7: The locations of the measured dHvA oscillations along with those of silver [77], copper [78], indium [72, 79] and the DFT prediction of Harima and Yanase for $CeCu_2Si_2$. The grey boxes illustrate the range of frequencies for all orientations yet measured. The letters on the silver oscillations represents their common designations. N - Neck, 4R - 4 Rosette, D - Dog's bone, B111 - [111] direction Belly and B100 - [100] direction Belly.

When all the physical constants are substituted into the Lifshitz-Kosevich equation (4.31), one obtains

$$v_{k,r} = 1.305 \frac{TFcVkR_\sigma J_k(\lambda r) \exp(-14.7m^*T_D/m_eB)}{|A''|^{\frac{1}{2}} B^{\frac{1}{2}} \sinh(14.7m^*T/m_eB)} \sin\left(\frac{2\pi F}{B} + \phi - \frac{\pi}{2}\right) \tag{8.7}$$

where we are now considering only the first dHvA harmonic. Using the following estimates for the properties of the silver, one can work backwards from a signal amplitude of 4×10^{-9} A to see that the silver need only be 1.1×10^{-11} m^3 in volume to produce the measured signal.

T (mK)	3	i (A)	3.8×10^{-19}
B (T)	13.9	b_0 (T)	4.1×10^{-6}
F (T)	47,750	$\lvert A''\rvert$	2π
m^*T_D/m_e (K)	1	R_σ	1
ω (s^{-1})	$2\pi \times 83$	$c(\Omega\ m^{-2}s)$	0.0019

Table 8.1: Quantities used to estimate the volume of silver.

This is far less than the actual quantity of silver in the vicinity of the coil. However, it must be remembered that we are dealing with a polycrystal where only a fraction of the randomly oriented crystallites will be contributing to the signal.

Apart from the belly oscillations there are also some of the other standard oscillations that one expects to see from silver. From figure 8.7 it appears that the following orbits (listed with their orien-

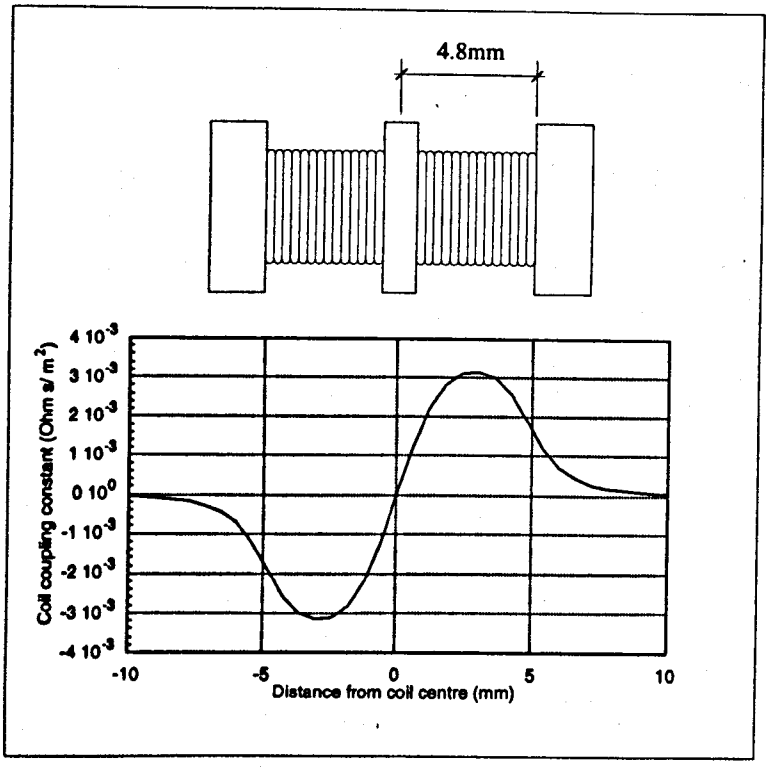

Figure 8.8: The coil coupling constant calculated for various positions relative to the main pickup coil. A dipole approximation was used and a negative value for c implies a signal 2π out of phase with that of the sample. The maximum possible coil coupling for this density of turns is $4\times10^{-3}\,\Omega m^{-2}s$.

tations) were observed. Neck:[111], 4-Rosette:[001], Dog's-bone:[110], Belly:[111] and Belly:[100]. So it appears that the signal was contributed to by a large number of crystallites with many orientations.

Silver alone cannot explain the range of frequencies observed. Particularly bewildering are those below 800 T (the neck orbit at 890 T is the lowest possible frequency in silver). It is very difficult to envisage any undiscovered orbits in such a simple metal and other effects such as magnetic breakdown can only lead to larger orbits.

To see whether the oscillations are genuinely periodic in 1/B rather than B they were Fourier transformed with respect to time as well (see figure 7.20 on page 88). Those oscillations that remain in the time Fourier transform are always smaller in amplitude than those present when the Fourier transform is with respect to 1/B. This evidence does not prove *per se* that the oscillations are periodic in 1/B but it does indicate that whatever functional form they possess, it more closely resembles periodicity in 1/B than time, which is the most likely other alternative. It can also be seen from figures 7.12 and 7.13 (pages 81 and 82) that the oscillations possess the characteristic thermal damping, referred to in chapter 4.

Having demonstrated that the observed signals are dHvA oscillations it follows that they must originate from within the main field region and they must have a strong coupling to the pickup coil. In the design of the susceptometer, only pure noble metals were used. Another possibility was that these oscillations were coming from the copper pickup coil itself, as has been seen before [35], but figure 8.7

suggests that this is not the case. We might even ask why we do not see the copper oscillations, since the SQUID is so sensitive, however if the pickup coil is adequately balanced, any copper dHvA should be cancelled out. The last candidate is indium, which was shown to be present in chapter 7. Comparison with figure 8.7 shows that the low frequency oscillations are in the correct region for indium, although it is necessary to assume that some of the oscillations are higher harmonics. The 27,250 T and 27,850 T oscillations are just outside the band of observed indium oscillations. However, it is conceivable that at some of the orientations which were not studied in these early experiments, lower frequencies are possible. As before one can estimate the quantity of indium required to produce the measured signals. Considering first the high frequency oscillations and substituting in the following values, one finds that a sample of volume $2 \times 10^{-13}\,\mathrm{m}^{-3}$ is capable of producing the oscillations.

T (mK)	15	i (A)	6×10^{-12}
B (T)	7	b_0 (T)	8.2×10^{-6}
F (T)	150	$\lvert A'' \rvert$	$2\,\pi$
$m^* T_D/m_e$ (K)	1	R_σ	1
ω (s^{-1})	$2\pi \times 83$	$c(\Omega\ m^{-2}s)$	0.0019

Table 8.2: Quantities used to estimate the volume of indium.

When observed under an optical microscope the indium is estimated to have a cylindrical shape with a diameter of 1.25 ± 0.1 mm and a thickness 0.2 ± 0.1 mm, giving a net volume of $(2.7 \pm 1.7) \times 10^{-10}$ m^3 (Note – the large error results from estimating the thickness). So, it can be seen that the volume of indium is far in excess of that required to produce the high frequency oscillations, which is what one would expect from a polycrystal.

A more puzzling result is obtained considering the low frequency oscillations. A similar analysis to above, shows that to produce the 100 T oscillation shown in figure 7.11, it is necessary to have $m_D^* T_D/m_e = 0.5\,\mathrm{K}$ and a curvature factor of 0.05 although the latter is not out of proportion as there are 'arms' of Fermi surface present in indium. The value required for the Dingle temperature is somewhat more suspect. It is not clear why a piece of material that was used as solder could approximate so well to a good single crystal. However, the indium employed was originally of a high purity and it could have produced large crystallites on solidifying. A possible indication that this might be the case is the limited number of oscillations present, whereas a continuum is possible in polycrystalline indium. Although this explanation is not entirely satisfactory it is within the bounds of possibility and seems the most probable explanation for the stray oscillations. It is also worth noting that the coil coupling to the solder has not been established experimentally and also that a smaller curvature factor can compensate for a larger Dingle temperature.

It would no doubt be possible to study the low frequency oscillations in greater detail and resolve some of these mysteries, but the EDX experiment showed quite conclusively that indium was present, so if the silver post is replaced with an alternative thermal connection and the oscillations are seen to disappear, this will be regarded as enough of a verification that indium was the cause of the problem.

8.3.1 $CeCu_2Si_2$ oscillations.

The question now arises, why the susceptometer was capable of seeing all these other contributions and not the sample itself. To calculate the expected signal amplitude we use the data collected in the conventional susceptometer. In figure 7.2 (page 70) it can be seen that the dHvA amplitude is equal to 1.5×10^{-9} V. As this was just a preliminary test to see whether the dHvA effect was present, no Dingle analysis was attempted, but an approximation to $m_D^* T_D/m_e$ can be estimated using the L.K. equation (8.7) and the following parameters.

T (mK)	20	V (m^3)	6×10^{-9}
B (T)	10.7	b_0 (T)	0.036
F (T)	150	$\|A''\|$	2π
v (V)	1.9×10^{-9}	R_σ	1
ω (s^{-1})	$2\pi \times 5.2$	$c(\Omega\ m^{-2}s)$	0.34

Table 8.3: Quantities used to estimate the Dingle temperature of $CeCu_2Si_2$.

Admittedly this will be a very crude estimate, but it will be a more faithful representation than just substituting in the measured susceptibility. Figure 8.9 shows that $m_D^* T_D/m_e = 1.1\,\mathrm{K}$.

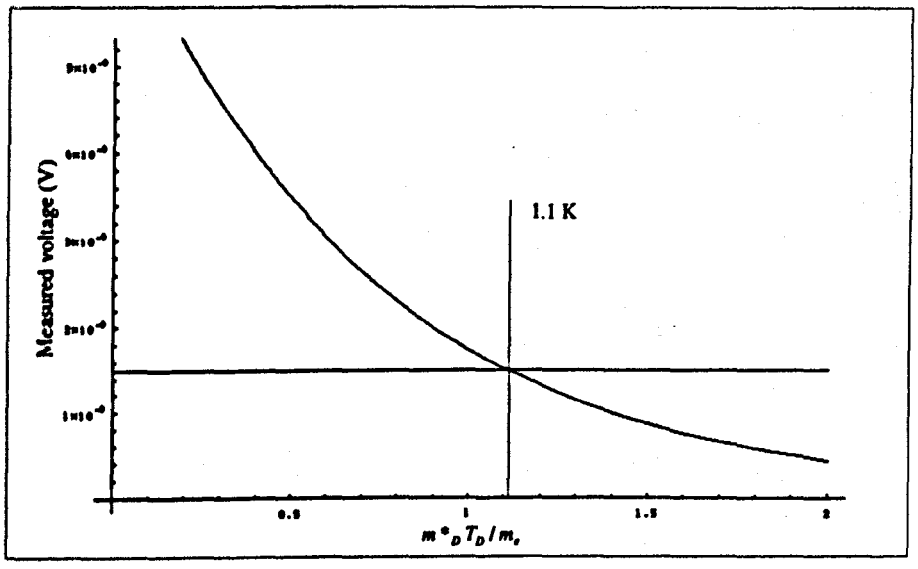

Figure 8.9: Estimation of the dingle temperature of the $CeCu_2Si_2$ crystal, based on the amplitude measured previously in the TLM.

Unlike for the contaminant signals it is possible to use the measured value of $-\frac{K(f)S(f)cV}{\sqrt{2}}$. When the parameters used in the sweep producing figure 7.11 on page 80, ($h_0 = 3 \times 10^{-6}$ T, $\omega = 2\pi 83$ Hz, $T = 15$ mK, $B = 6.5$ T) are substituted into the L.K. equation (8.7), the input current is calculated to be 2.75×10^{-11} A (see figure 8.10). This is slightly smaller than the (4×10^{-11} A) 150 T oscillation that was observed in figure 7.11. While this is well within the kind of errors associated with this calculation, it is also conceivable that the oscillation is a higher harmonic of the 50 T oscillation. The main point however is that the calculations are compatible with the observations.

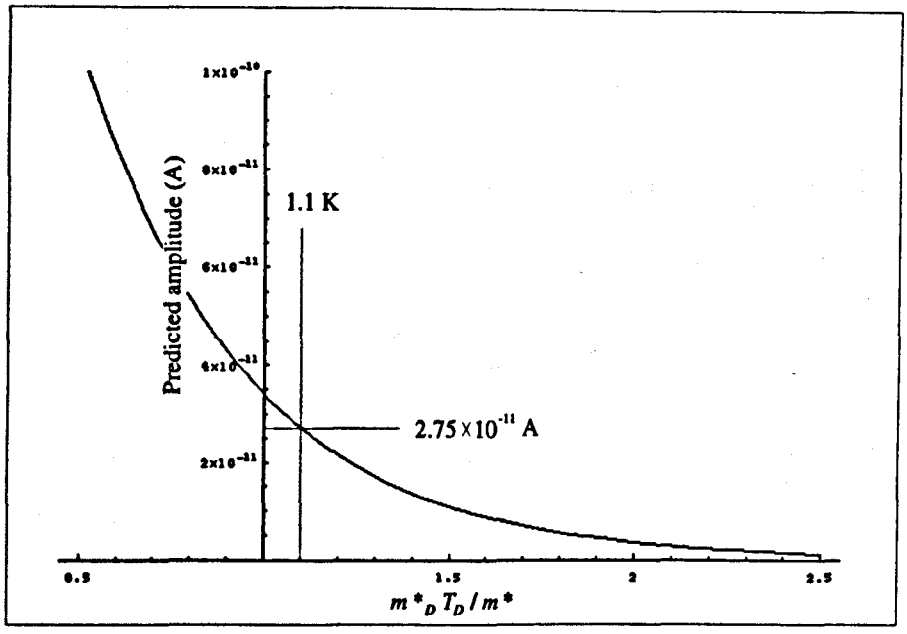

Figure 8.10: The predicted amplitude of the 150 T dHvA oscillation based observations in a conventional susceptometer.

We can also calculate the expected amplitudes of peaks at higher frequencies. The experiments that probed the different regions of dIIvA frequencies possessed different parameters, hence the different sections in figure 8.11.

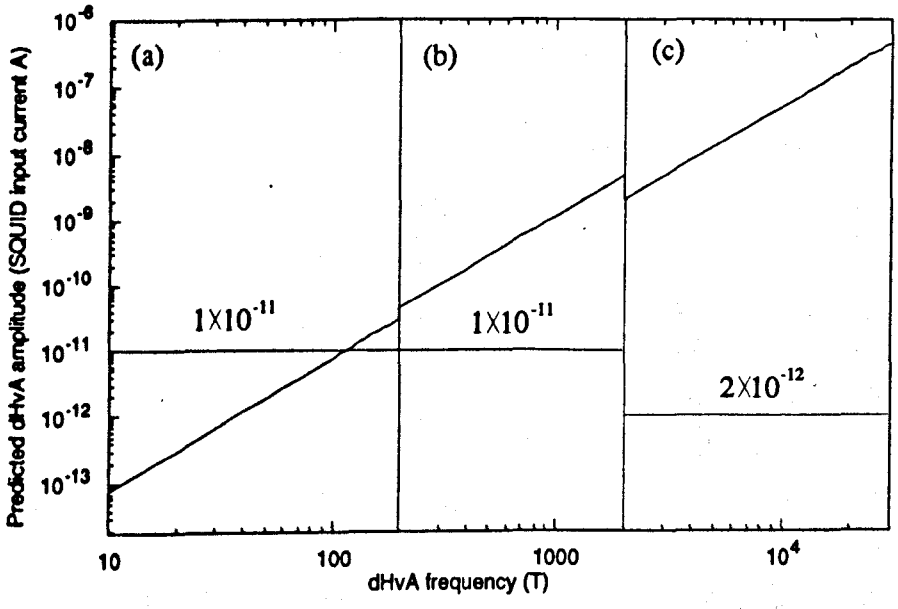

Figure 8.11: The predicted amplitudes for oscillations based on the properties measured in the conventional susceptometer. The different sections correspond to the experiments displayed in (a) figure 7.11, (b) figure 7.20-a and (c) figure 7.16. The horizontal lines indicate the noise floors.

8.3.2 Effective mass and Dingle temperature plots.

These calculations have relied on the Dingle temperature calculated from the conventional susceptometer measurement. One can produce a comparison of possible observable frequencies based on an arbitrary crystal, by considering the strength dHvA signal required to produce an oscillation above the noise floor in the long, cold experiment shown in figure 7.16 on page 84.

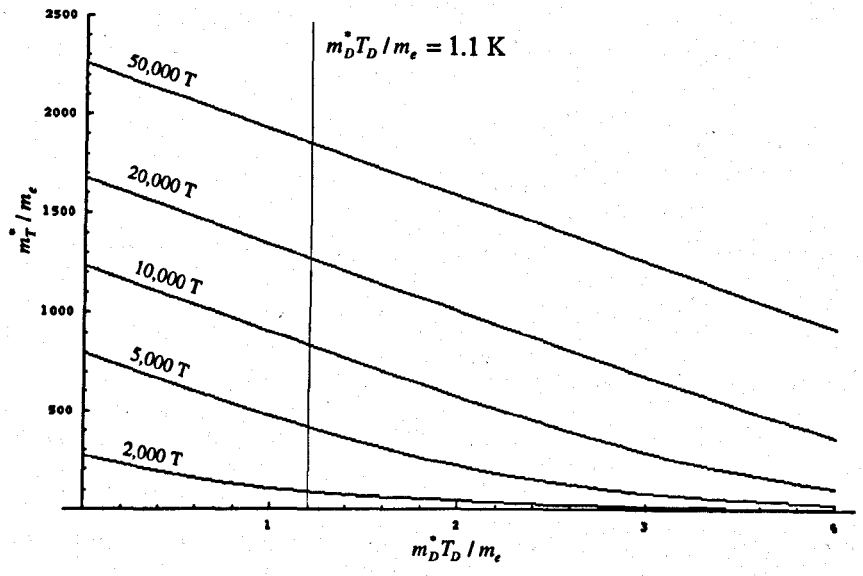

Figure 8.12: Attainable m_T^*/m_e for a given $m_D^* T_D/m_0$. The curvature factor is assumed to be 2π. Oscillations bounded by a particular frequency line should be visible.

Figure 8.12 shows a plot illustrating the conditions necessary to observe a range of oscillations. The x-axis is chosen to be represented by $m_D^* T_D/m_e$, even though this is not an immediately physically meaningful parameter, because it is widely used in the literature and (unlike the quasiparticle lifetime, τ^* or the quasiparticle mean free path, δ^*) it is possible to define it without making any assumptions about the shape of the Fermi surface or m_D^*.

It is also possible to turn to the DFT predictions of Harima and Yanase [65]. Figure 8.13 is the same sort of plot, but this time employing the predicted frequencies and curvature factors for $CeCu_2Si_2$. It should be noted that due to the complications of silver and indium oscillations at low frequencies, it would only be possible to unequivocally identify the predicted 5,040 T oscillation, but this oscillation is expected to have the largest amplitude and to be the most accurately predicted due to its (reciprocal space) size. It should thus be possible to put a lower limit on the effective mass of this oscillation. Assigning the value of $m_D^* T_D/m_0$ as 1.1 K, the minimum predicted m_T^*/m_e is 1,350 m_e. This designation of m_T^*/m_e is fairly arbitrary as the Dingle temperature was established in a rather crude manner, and most importantly, past experiments have shown $m_D^* T_D/m_0$ to be anisotropic [80] and so it might well vary among the different sheets of the Fermi surface. However, the value does lie between those previously encountered ($m_D^* T_D/m_0$ = 1–2 K), and is so assumed to be a fairly good estimate.

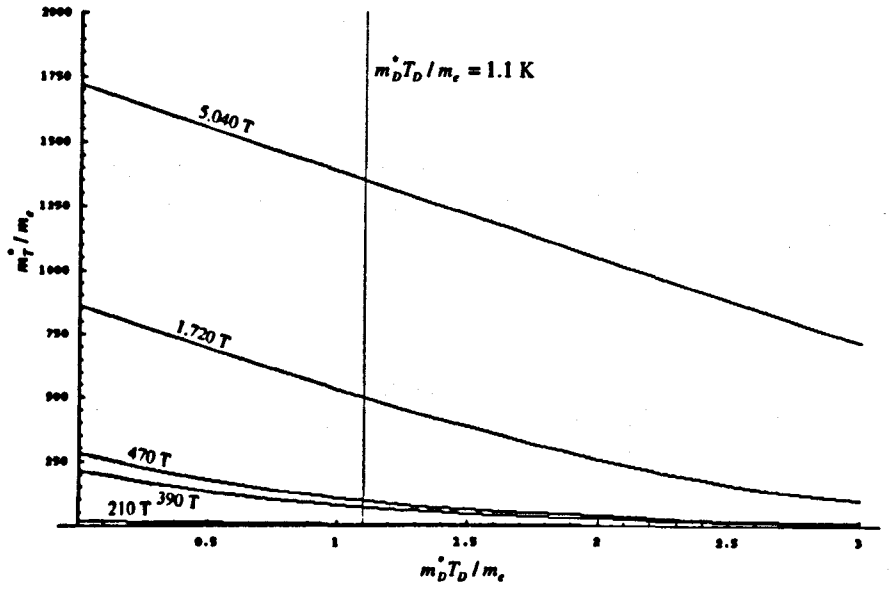

Figure 8.13: Attainable m_T^*/m_e for a given $m_D^* T_D/m_0$, using the calculated frequencies and curvature factors of Harima and Yanase [65].

Using the lower limit to the effective mass $1{,}350\, m_e$, it is possible to compare the predicted density of states to that measured in specific heat measurements, in the manner of Chapman *et al.* [81]. In terms of parameters accessible by dHvA measurements, the density of states is given by

$$g(E_F) = \frac{1}{4\pi^3} \int_S \frac{dS}{\hbar |v^*|} = \frac{1}{4\pi^3 \hbar} \sum_i \frac{S_i}{v_i^*} \tag{8.8}$$

where

$$\langle v^* \rangle = \frac{\hbar k_0}{m^*} \tag{8.9}$$

with

$$\pi k_0^2 = \frac{2\pi e F}{\hbar} \tag{8.10}$$

where the sum is over Fermi surface sheets, each of area S_i, v^* is the quasiparticle velocity averaged around a particular orbit, F is the dHvA frequency of that orbit ($F = \frac{\hbar}{2\pi e} A$), k_0 is its average radius in reciprocal space and m^* is the measured quasiparticle mass for the orbit.

For simplicity, if one assumes spherical sheets of Fermi surface of area $4\pi r^2$, the density of states can be simplified to

$$g(E_F) = \frac{m_e}{\pi^2 \hbar^2} \left(\frac{2e}{\hbar}\right)^{\frac{1}{2}} \sum_i \frac{F_i^{\frac{1}{2}} m_i^*}{m_e} = 4.58 \times 10^{44} \sum_i \frac{F_i^{\frac{1}{2}} m_i^*}{m_e} \text{ states m}^{-3}\,\text{J}^{-1} \tag{8.11}$$

Considering just the *single* sheet of Fermi surface at 5,040 T with an effective mass of $1{,}350\ m_e$, one finds

$$g(E_F) = 4.4 \times 10^{49} \text{states m}^{-3}\,\text{J}^{-1} \tag{8.12}$$

In order to compare this figure to the measured linear contribution to specific heat, it is worth noting that the specific heat in heavy fermion compounds is commonly found to be quenched in high

fields. However, in the case of $CeCu_2Si_2$ this phenomenon is found to be sample dependent. In some crystals it was observed to decrease by only 5% upon the application of a 23 T field [82], whereas in others [83] by 30 %. There is also some divergence on the low temperature value of γ. Taking the maximum value that has been observed [83], $\gamma = 1.4\,\mathrm{JK^{-2}mol}$, (although that particular study only went down to a temperature of 0.3 K, where γ was still found to be rising with falling temperature), and using the simple relation (see e.g. [32]).

$$\gamma(0) = \left(\frac{\pi^2}{3}\right) k_B^2 g(E_F) = 6.27 \times 10^{-46} g(E_F) \tag{8.13}$$

one obtains a value of 2.2×10^{45}states $\mathrm{mol^{-1}\,J^{-1}}$. Inspection of figure 6.1 (page 60) indicates a molar volume of $5.03 \times 10^{-5}\mathrm{m^{-3}}$ for $CeCu_2Si_2$, so

$$g(E_F) = 2.2 \times 10^{45}\mathrm{states\,mol^{-1}\,J^{-1}} = 4.4 \times 10^{49}\mathrm{states\,m^{-3}\,J^{-1}} \tag{8.14}$$

Thus, the predicted dIIvA value and the specific heat value are the same. This is somewhat coincidental as the predicted density of states from the specific heat is expected to be larger because we considered only one sheet of the Fermi surface and at other orientations there are expected to be other, far larger sheets (see figure 6.8 on page 66). Within the errors of this measurement (and that of the specific heat) it is possible that only the 5,040 T oscillation is strongly renormalised and the other oscillations possess only light masses, as was observed for the 150 T oscillation [64]. However this is a highly contrived situation, so the question must be asked why the 5,040 T oscillation was not observed.

8.3.3 Reasons for the absence of the 5,040 T oscillation.

The first suspect must be the reasoning employed to calculate figure 8.13. Rather than presenting each stage in the calculation, it is probably better to put forward a series of justifications (which unavoidably involve comparison with a wide range of results presented earlier in this thesis). The sensitivity employed in these calculations was that measured in section 8.2, which agreed quite well with the predicted sensitivity. On the evidence of the oscillations that were observed coming from the indium, this sensitivity appears to be correct, if not an under-estimate. It is also consistent with the predicted 150 T amplitude. Inspection of equations 8.7, 4.32 and figure 4.5 (page 30), indicate the signal amplitude should be proportional to F^2 in the limit of small modulation fields. So to a certain extent, figure 8.11 is validated. Then comparing figure 8.11 with figure 4.4 (page 27) the x-axis of figure 8.13 is established. Likewise, figure 8.11 and figure 4.3 (page 26) confirm the y-axis. So within the assumptions that were used to derive it, figure 8.13, would appear to be correct.

There are a variety of other possibilities to explain the absence of the oscillations. It is conceivable that the predicted frequencies and curvature factors are incorrect. If the oscillation is substantially smaller than predicted, it could be lost within the low frequency indium and silver 'neck' oscillations, whereas if it is larger it could be obscured by the silver 4-rosette and dog's-bone oscillations. A larger than predicted curvature factor, can also substantially reduce the amplitude of oscillations. On the

other hand, it is a fairly large sheet of Fermi surface that should be resilient to any deficiencies in the calculations.

There is also great uncertainty in the Dingle temperature employed in these calculations. However, it is not considered worthwhile to pursue finding the 150 T Dingle temperature with greater accuracy because, although it will be an indicator of sample purity, it will not present us with more confidence in the 5,040 T Dingle temperature. If $m_D^* T_D / m_e$ is as high as 3 K, the effective mass need only be $720\, m_e$ which is more consistent with specific heat measurements.

Another concern is field homogeneity. It can be seen from figure 7.9 (page 79) that there is a prominent out of balance signal in the pickup coils. This, coupled with the fact that the indium solder produced such strong oscillations, might indicate that the modulation coil is not centred on the sample. Alignment to the field centre is made with reference to a fiducial plate which is bolted to the 4 K plate. Distances of the field centres to the plate were measured when the fridge was originally installed. Using this reference plate, the field centre is measured to be exactly in the middle of the sample. These measurements should still be valid after the repairs that were performed on the magnet, because none of the work involved disassembling the magnet support structure.

There are other reasons to doubt whether this is the cause of the absent signal. Firstly, the unusual properties are shared with the secondary susceptometer, which is known to be well centred with respect to the modulation coil. So presumably the unbalanced signal is due to actual pickup coil imbalance or (as has been found by other group members) stray inductance. Also, it can be seen in appendix B that the modulation field centre is shifted by 2 mm from its intended location, so it is possible to have a significant imbalance whilst still being correctly positioned for the main field. Finally, at 14 T a 5,000 T oscillation will have a period of 0.04 T, so for this magnet with a homogeneity of 0.1 % over 10 mm, it would be necessary to be misaligned by 7.6 mm to dampen the oscillations (using the criterion that the dIIvA period be five times larger than the field inhomogeneity). This kind of error is unlikely.

Another possible reason why the 5,040 T oscillation is not seen, is the observation that in heavy fermion materials the oscillations are often found to be absent along directions of high symmetry. This idea might have its origin in the limited number of samples studied or perhaps be due to interference effects coming from multiple sheets of Fermi surface. This study was entirely conducted along the a-axis of this tetragonal compound, due to available sample geometry.

One of the most worrying concerns is that the sample might not be cooling properly. The calculations performed in section 7.3 suggest that the modulation should not be large enough to warm the sample significantly. However these are not measured parameters and there is a lack of knowledge about the Kapitza boundary resistance of the silver loaded paste and between the cold finger and the demagnetisation stage. One reassuring fact is that if excessive heat is introduced, it will enter by the cold finger (not the sample), which is well coupled to the melting curve thermometer, so any temperature rise should be visible. As this aspect of the experiment is such a crucial issue, it might be worth conducting some tests to ensure that the sample is cooling properly. The standard method for

this, is to see how the dHvA amplitude of a 'heavy' oscillation varies with modulation field amplitude, but unfortunately that presupposes the existence of a clear signal.

One fairly quick check might be to measure the temperature dependent background susceptibility of the sample (it will be necessary to have removed the spurious sources of susceptibility), at a range of modulation field amplitudes. One could then locate a fine bundle of palladium-iron wires in the other half of the balanced pair, thermally attached to the sample. Palladium doped with very small quantities of iron is known to follow the Curie-Weiss law down to sub-millikelvin temperatures, (for small enough iron concentrations), and so can act as a thermometer. By subtracting the sample's background susceptibility, it should be possible to establish its temperature. In order for the dominant heating to be in the sample and not the palladium bundle, the wires will need to be 0.1 mm in diameter, and for the signal to be clearly detectable there will need to be 100 of them. This test will only work in the absence of the main field but it would at least provide information about the thermal link to the sample.

One explanation that should not be ignored is the possibility that the heaviest quasiparticles do not exist. Despite strenuous efforts, the maximum m^* observed in dHvA experiments, always seems to be limited to around $150\,m_e$. One possible reason for this could be the theory of Kagan *et al.* [27], where γ is also contributed to by uncharged 'spinons', but within this theory one would still expect to see some lighter, charged quasiparticle bands. It is also worth considering whether the Born-Oppenheimer approximation is still valid. If the electron effective masses are truly approaching 1,000 m_e, their dynamics will become comparable with that of the ionic nuclei due to equation 8.9, so it will no longer be possible to decouple the two systems. The effect of this on theoretical predictions is somewhat unknown because it is generally a tacit assumption that this approximation is valid.

It appears that at present, this is not quite a publishable case for the imbalance of the density of states measured by the dHvA effect and the specific heat, so it is instructive to see what is required. Clearly the most important factor is temperature, which has already been discussed. Then what is needed is an experiment that displays no spurious oscillations and preferably with some known $CeCu_2Si_2$ dHvA oscillations present. Later in this chapter, improvements are suggested that should make this possible. If a full angle resolved study were then performed and compared with a specific heat measurement on the same crystal, it would provide quite a conclusive test.

8.3.4 Oscillations observed by the secondary susceptometer.

The 8T experimental region presents slightly more ambiguous results, since the oscillations that were present when the sample was in place, disappeared when it was removed. However, there are a number of clues suggesting that these oscillations might also be a remnant of the experiment.

The low frequency oscillations can presumably be assigned to the indium solder (employed in this experimental region too), as they do not match the 150 T oscillations, observed in the conventional susceptometer. The difference was originally ascribed to misalignment of the crystal, however later Laue back-scattering x-ray studies indicated that this was not the case. There remains the problem of

explaining why the oscillations would then disappear once the crystal was removed, however it should be noted that between these two events a study was attempted on a wider piece of crystal and so a different pickup coil was installed. Although the coil was supposed to have superficially the same coupling to the sample, the coupling to the indium will depend sensitively upon the exact distance to the indium on the silver post (see figure 8.14). It is not so easy to control this distance as in the main susceptometer, due to the geometry of the r.f. shielding. Another important factor, is that the post was cleaned thoroughly with acetone between experiments to remove the silver paint and this might have dislodged pieces of indium.

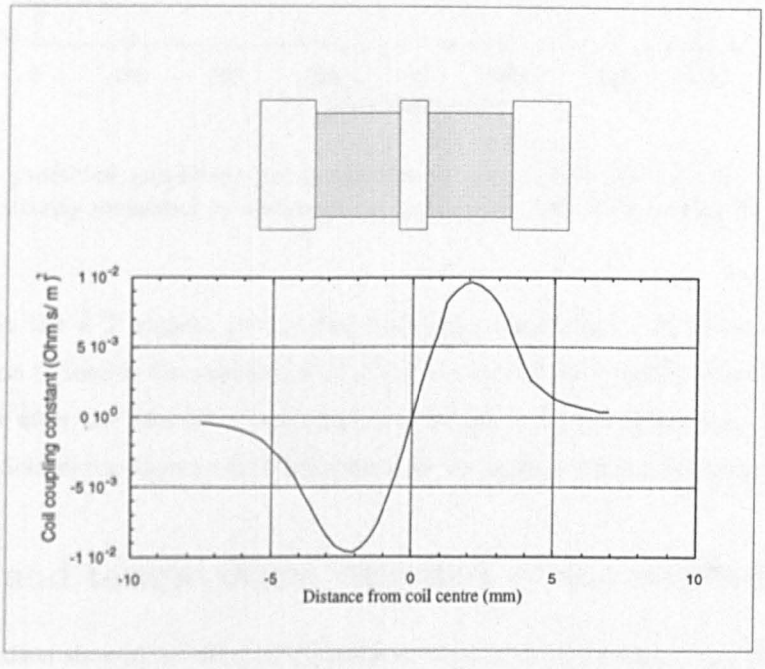

Figure 8.14: The coupling constant for the pickup coil in the secondary susceptometer.

So perhaps it will be impossible to establish whether the peaks are definitively due to indium or $CeCu_2Si_2$ but it will be possible to see whether the susceptometer would be sensitive enough to detect $CeCu_2Si_2$ oscillations at these frequencies. Using the sensitivity measured in figure 8.6, it is possible to predict the dHvA frequency dependence of the signal amplitude (see figure 8.15).

Comparison of figures 8.15 and 7.19 indicate that it is within the limits of the susceptometer that the observed oscillations could arise from $CeCu_2Si_2$. The obvious counter to this assertion is to ask why the oscillations were not then subsequently observed in the main field susceptometer. It is possible that the Dingle temperature was somehow increased during the exchange of the crystal. However the crystal was always treated carefully so there is no obvious reason for this. There is a suspicion that thermal cycling can increase the Dingle temperature but it is difficult to imagine it having such a dramatic effect. It should also be born in mind that any $CeCu_2Si_2$ oscillations might be obscured by those arising from indium.

Another reason to question the origin of these peaks is that they lie within a region of the frequency domain which is known to have shown oscillations from indium, although there is the qualitative

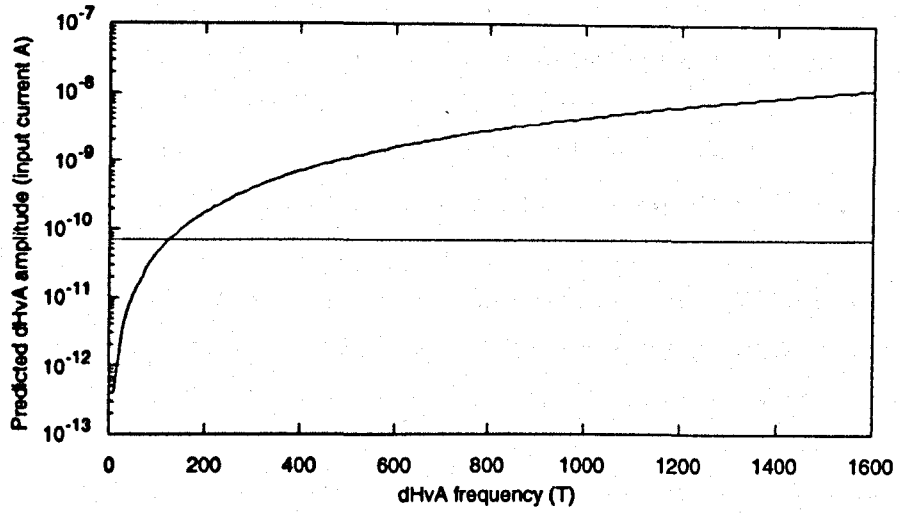

Figure 8.15: The predicted amplitude for an oscillation with curvature factor 2π and $m_D^* T_D/m^* = 1.1$ K, for the sensitivity measured in the secondary susceptometer. This prediction can be compared with figure 7.19.

distinction that in the 8 T region, the oscillations were more defined. It seems that there is not enough information to resolve the problem so it would perhaps be worthwhile returning the sample to the susceptometer after the improvements outlined in section 8.7 have been performed. The unusual temperature and field dependences will be discussed in the framework of both interpretations.

8.4 Field and temperature variation of the oscillations.

The 1400 T oscillation showed an unusual decrease in amplitude on reducing the temperature below 500 mK. Before discussing possible mechanisms that could account for this behaviour, it is worth considering whether it could be an artifact of the experimental method.

8.4.1 Experimental error.

The most obvious culprit would be poor thermometry. Much of the experiment was conducted at a higher temperature than that accessible by melting curve thermometry so measurements were made using the 200 Ω Matsushita resistance thermometer mounted on the mixing chamber. This is slightly remote from the sample but between each temperature change a period of one hour was allowed to elapse before conducting experiments. Also, the resistance thermometer was only used at higher temperatures where relaxation times are seen as less of a problem. Perhaps the most decisive evidence that the thermometry was not at fault is the fact that all the other dHvA peaks follow the expected temperature variation (Even if some of the peaks are too small to fit to an $X/\sinh(X)$ curve, they still decrease at elevated temperatures).

So the alternative is that perhaps the oscillation is being attenuated by some mechanism that switches on when the temperature is reduced. As the other peaks are not effected (and this is the

highest frequency) we require something that produces a low pass filtering effect where the cutoff frequency scales with temperature. It is very difficult to envisage such a mechanism, because the signal is still in the form of an amplitude modulated oscillation. The only filtering taking place inside the fridge is the very wide band filtering of the SQUID input circuit. Only the lock-in amplifier has a suitably narrow filter that it could effect the signal and this is clearly not dependent upon the sample temperature.

Lastly, it is well known that a Bessel minimum can attenuate a particular frequency (although the effect is not usually temperature dependent). However, in this experiment the first Bessel minimum would occur with a modulation field of 20 mT and the actual modulation field was only 34 μT, so this is presumably not the cause either.

8.4.2 Polycrystalline and second harmonic effects.

Perhaps the simplest explanation would be an interference effect between either separate crystallites of silver/indium or between silver/indium and $CeCu_2Si_2$ or even (less probably) interference due a twinned $CeCu_2Si_2$ crystal. To achieve the effect one would require two sets of oscillations at the same frequency but possessing a (dIIvA or instrumental) phase approximately π out of phase with each other. The oscillations must also possess different temperature dependences (different effective masses). The effect is sketched in figure 8.16.

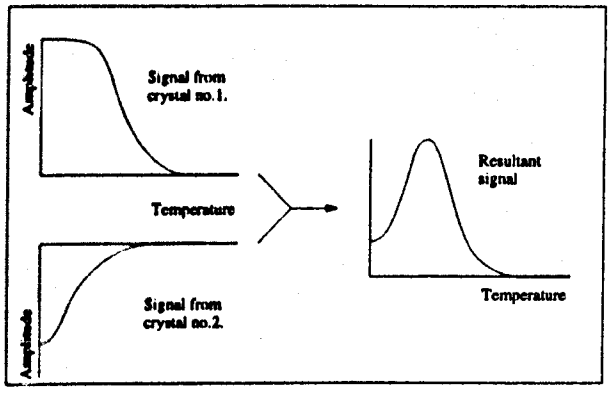

Figure 8.16: The effect of adding two oscillations which are out of phase and have different temperature variations.

Taking this idea, one can fit to the data, to calculate the separate properties of the oscillations. One such fit is shown in figure 8.17. The fit was originally attempted with four fitting parameters (the two amplitudes and m^*s) but it gave unphysical results, so the amplitude of the larger oscillation was fixed at 20 mV, leaving the other three parameters to be fitted. The fit is still not particularly convincing for the lighter oscillation although the heavier oscillation appears to be represented quite well. If we assume that the masses predicted by this are reasonable, then it would appear that the lighter mass is of a suitable size to be coming from silver or indium and the heavier mass is of a sufficient magnitude (3.7 m_e) to be likely to originate from the sample.

Another way that masses can appear enhanced is by looking at higher harmonics. The L.K.

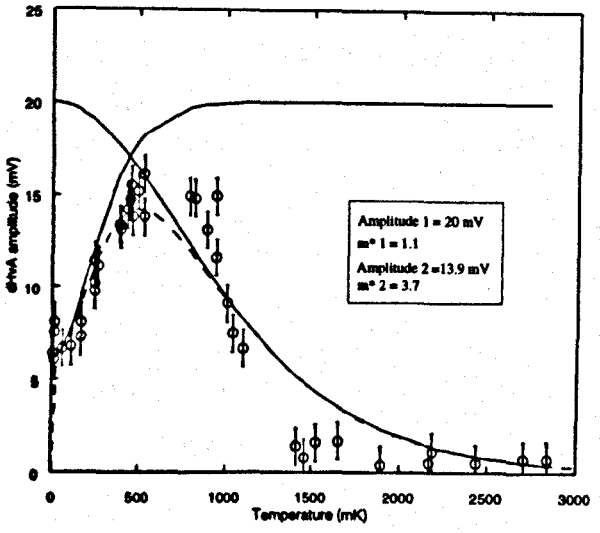

Figure 8.17: Fitting to the anomalous peak as the difference between two, thermal damping terms. The solid lines show the separate dependences and the dashed line is the difference.

equation (4.10) indicates that the both the effective mass and Dingle temperature are multiplied by the harmonic index. There is another oscillation suitably located at 730 T, but its amplitude is only 20 mV (see figure 7.6c on page 76). It is possible to calculate what value of $m_D^* T_D/m_e$ would be capable of producing this reduction using the following rearrangement of the Dingle term

$$\frac{m_D^* T_D}{m_e} = \frac{H}{14.693}(\ln(A_1/F_1^2) - \ln(A_2/F_2^2)) \tag{8.15}$$

where A_1 and A_2 are the amplitude of the first and second harmonic signals, and F_1 and F_2 are their frequencies (to make allowance for the sensitivity of the susceptometer). One thus obtains $m_D^* T_D/m_e = 0.85\,\mathrm{K}$, which is very low, but is not inconceivable for either the $CeCu_2Si_2$ sample or, judging by the calculations performed in section 8.3, for indium solder either.

The next question to address is how the signals could be π out of phase. Once more the most natural interpretation is in terms of a second harmonic. The spin slitting term is given by

$$R_\sigma = \cos\left(\frac{\pi r m^* g}{2m_0}\right) \tag{8.16}$$

and for sufficiently simple metals, g is close to $2/(m^*/m_e)$, so R_σ reduces to $(-1)^r$. So a second harmonic will automatically be π radians out of phase with a first harmonic signal.

Other possible origins do not follow quite so simply and the phase constants γ of metals are thought to be well represented by $\frac{1}{2}$.

8.4.3 Effects due to the $CeCu_2Si_2$ crystal.

Although second harmonic interference would appear to be the most probable interpretation, it is also worth considering whether the anomalous behaviour might arise solely from the $CeCu_2Si_2$ crystal because some similar behaviour has been seen in the isostructural heavy fermion compound $CeRu_2Si_2$.

This material has been extensively studied, and due to its stable chemistry and moderate effective masses, clean dHvA oscillations have been observed [84]. There is a well known phenomenon known as a spin splitting minimum where the spin splitting term becomes zero. This occurs when $\pi g m^*/2m_0 = \frac{\pi}{2} \pm 2n\pi$. However the Tsukuba group also noticed that the location of the minimum was both field and temperature dependent, and was accompanied by a change in dHvA frequency. In an effort to explain this, they envisaged effectively two Fermi surfaces arising from the up and down electrons. Implicit in the derivation of the standard L.K. equation is the fact that amplitude, frequency, effective mass and g-factor are spin independent, but if one makes no such assumptions and ascribes the two orientations with their own temperature and field dependent effective masses, many of the phenomena can be explained. In this more general case a minimum can occur when

$$\xi_\downarrow(H) - \xi_\uparrow(H) = \pi \pm 2n\pi \tag{8.17}$$

where

$$\xi_\uparrow = -\frac{\pi m^*_\uparrow g_\uparrow}{2m_0} \tag{8.18}$$

and

$$\xi_\downarrow = \frac{\pi m^*_\downarrow g_\downarrow}{2m_0} \tag{8.19}$$

Deviations from g=2 are either due to spin orbit coupling or e-e many body interactions, and are therefore of relevance in the present work. To fit their measurements it was necessary for the Tsukuba group to invoke oscillations from up spin electrons with a heavier mass than from the down spin oscillations. This will produce the same kind of beating effect seen in figure 8.16.

Perhaps a more natural interpretation than this would be to consider how these terms might change on entering either phase A or phase B. It can clearly be seen in the B/T phase diagram (figure 7.15) that the field sweeps conducted between 6.2 and 7.8 T are well located to enter the A phase (and presumably the B phase) at approximately 500 mK. Both these phases are assumed to be of magnetic origin, so it is proposed that either the up/down g-factors are changed so as to interfere with each other in the way described above, or their values change in a more conventional way that produces a spin splitting zero.

8.4.4 Field dependent effects.

Perhaps the most striking field dependent effect is a comparison between figures 7.12 and 7.13 (pages 81 and 82). Performing the same experiment in different field regions produces different frequencies and different effective masses. This can most easily be ascribed to having polycrystals present. They will inevitably introduce beating effects so various frequencies will come and go above the noise floor. The effective masses present in indium have been found to vary between 0.2 and 0.4 m_e along the [001] to [100] plane [85] so this is consistent with the masses measured in this study, if higher harmonics are also considered.

Also of interest is figure 7.18 (page 85) where the 27,850 T oscillation is seen to not show the characteristic exponential increase with field. From the section measured in this study it appears

that the oscillations display an oscillatory variation of amplitude. Originally this fact was of interest because the oscillations were thought to be coming from the $CeCu_2Si_2$ sample, however the fact is still of relevance because it might act as another clue for the origin of these oscillations. Indeed, in an early study on indium [79] the authors note *... the dHvA data were complicated, showing complex aperiodic beat patterns. This effect is probably due to material behaviour problems peculiar to In, rather than to an intrinsic Fermi surface property.* Later work [72] suggested that the origin of the beats might be magnetic interaction from the third zone electrons.

Unfortunately, since these oscillations are obscured by silver oscillations, it is impossible to see directly how the amplitude behaves with field. Figure 7.18 was obtained by Fourier analysing sections of field sweeps, so it is worth ensuring that this method cannot introduce spurious effects. The most obvious error that could be introduced would result from aliasing, as was discussed with reference to data acquisition. As the amplitude is sampled at a finite number of points, one might imagine that the low frequency variation of dHvA amplitude is a higher frequency variation that has been 'folded down'. However this is not possible because this method has its own in-built anti-aliasing filter in the form of the finite Fourier transform sections.

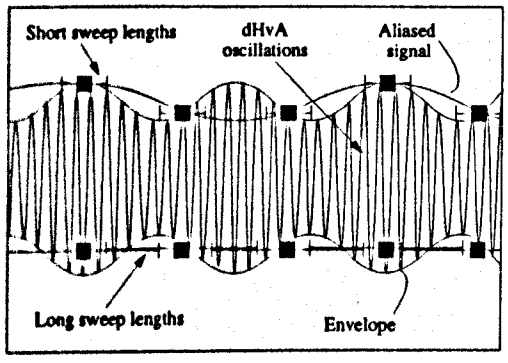

Figure 8.18: The effect of finite point interval and finite Fourier transform length on signals for a hypothetical variation of dHvA amplitude. If an insufficient number of sections are Fourier analysed, aliasing can occur. However, if the sections are long compared with any characteristic features an anti-aliasing effect is produced.

As can be seen from figure 8.18 if the sections of field sweep are short compared with the point spacing then aliasing can occur. If the sections are longer, the variation in amplitude is averaged out and so acts like a low pass filter. In this particular case the separation of each point is typically $\frac{1}{10}$th of the section lengths, which are almost as long as the variations so aliasing can be ruled out, and in fact the variations in amplitude must be appreciably greater than measured.

Another concern is that the variation might be random noise on the signal. To ensure that this is not the case, the experiment was repeated, and it is evident from figure 7.18 that the points from separate sweeps show the same behaviour.

The period of the envelope oscillation appears to be 4 T when the field is at 14 T. If this is due to magnetic interaction this will correspond to a dHvA frequency of 49 T, which is indeed approximately the location of a prominent measured peak and also well within the range of those previously seen in indium. This helps to confirm that the high frequency oscillations originate in the indium.

8.5 Detection of the metamagnetic transition.

An important question relating to the sensitivity of the susceptometer is why it was possible to detect the metamagnetic transition when the susceptometer was used in the pulsed field mode, and yet the transition was never seen when the susceptometer was used employing the field modulation technique, but the exact opposite is true for the low frequency dHvA oscillations. This effect is strikingly visible in figure 8.19.

The most obvious starting point is to consider whether the frequency dependent sensitivity of the field modulation technique is discriminating against the transition, whereas the broad band sensitivity of the pulsed field experiment succeeds in detecting it.

Firstly, one can estimate the magnitude of the peak in $\frac{dM}{dH}$ at the transition. For a pulsed field experiment, the voltage generated in a pickup coil is given by

$$v = -cV\frac{dM}{dt} = \frac{dM}{dH}\frac{dH}{dt} \tag{8.20}$$

So the input current of the SQUID will be

$$i = K(f)v = -cVK(f)S(f)\frac{dM}{dH}\frac{dH}{dt} \tag{8.21}$$

The group of terms $-cVK(f)S(f)$ has been established in section 8.2 and is displayed in figure 8.5. However we are faced with choosing an appropriate frequency for the term $K(f)S(f)$. As a crude approximation the peak in $\frac{dM}{dH}$ is modelled as half a sinusoidal oscillation (see figure 8.19).

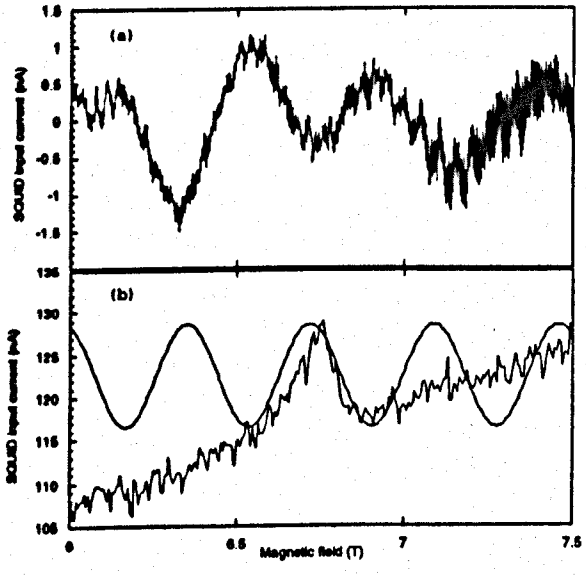

Figure 8.19: Comparison of experiments conducted using (a.) the field modulation technique and (b.) the pulsed field technique. In (a.) the sweep rate was 0.02 T/min, the modulation amplitude was 4 $\times 10^{-5}$ T and the modulation frequency was 83 Hz. In (b.) the metamagnetic transition is modelled by a sinusoidal oscillation of period 0.37 T. The field sweep was conducted at 0.693 T/min ($9.2 \times 10^{3}\mathrm{Am}^{-1}\mathrm{s}^{-1}$) so this corresponds to a frequency of 0.031 Hz.

Having a frequency of 0.031 Hz, this is in the extreme low frequency limit and $\frac{K(f)S(f)cV}{\sqrt{2}}=2.8\times 10^{-10}$ ms (so $K(f)S(f)cV=2\times 10^{-10}$ ms). The amplitude of the peak is 12 nA, so one obtains a value of $\frac{dM}{dH}=4.7\times10^{-3}$. The noise floor on this measurement (with respect to field) is 3 nA corresponding to a susceptibility of $\frac{dM}{dH}=1.2\times10^{-3}$, in the low frequency limit.

For the field modulation experiment it is necessary to account for the finite size of the modulation field amplitude relative to features in the susceptibility curve. However because of the low modulation amplitude, the Bessel function is strictly in the linear regime.

$$i = K(f)v = -cVK(f)S(f)\frac{dM}{dH}\frac{h_0\omega}{\sqrt{2}} \tag{8.22}$$

Now one employs the value of $\frac{K(f)S(f)cV}{\sqrt{2}}$ at 83 Hz, which is 2.5×10^{-10} ms. The dHvA amplitude is 1.5×10^{-9} nA, in the region of interest. So this corresponds to a susceptibility of only 5.1×10^{-4}. It is therefore clear that the dHvA oscillations were too small to be observed in the pulsed field experiment. What remains puzzling is why the metamagnetic transition was not seen in the field modulated experiment, as it seems to have a similar frequency to the dHvA oscillations. There is a feature in the field modulation experiment that could be identified with the transition, but this only corresponds to a susceptibility change of 3.4×10^{-4}, rather than 4.7×10^{-3}.

It is possible that the explanation for this might arise from the other great difference between the experiments - The main magnet was swept 35 times as fast in the pulsed field experiment. All the previous conventional susceptometer experiments, which clearly showed the transition, were also performed at a fast sweep rate. Perhaps the susceptibility at the metamagnetic transition also depends upon the dynamics of the experiment. It is conceivable that if the A-phase is a spin glass (as was proposed by Uemura *et al.* [59]) that the final state might depend upon the (magnetic) history of the sample. Unfortunately no data was collected employing the field modulation technique at fast sweep rates using the SQUID susceptometer, because it is not possible to supply a large enough modulation current that the condition $\dot{h}_0 \gg \dot{H}$ is valid.

There appears to be no mention of studies of sweep rate effects in the literature, so if the opportunity arises it would make a suitable quick experiment to perform in our top-loading cryostat. If this interpretation is correct, it is possible to infer from this experiment that the amplitude of the susceptibility peak at the metamagnetic transition drops from 4.7×10^{-3} to less than 3.4×10^{-4} when the sweep rate is reduced from 0.693 T/min to 0.02 T/min.

8.6 Absolute sensitivity compared to a conventional susceptometer.

The fact that the SQUID susceptometer failed to observe the dHvA oscillations seen in the conventional susceptometer would appear to suggest that this approach has failed to produce an adequate sensitivity. However, it should be born in mind that while the conventional system was operating over its optimum parameter range, the signal entering the SQUID susceptometer was compromised by the low dHvA frequencies encountered. Using the measured coupling of the sample to the SQUID and the calculated sensitivity of the conventional susceptometer, it is possible to compare their properties over a range of magnetic fields and frequencies. The experiments performed in the SQUID susceptometer were generally slower than those performed in the conventional system so the fairest way of calculating the relative sensitivities would be to express them in terms of sensitivity per $\sqrt{\text{Hz}}$.

First considering the smallest $\dot{m}$ detectable, one can divide the noise floor by $-\frac{K(f)S(f)c}{\sqrt{2}}$, which is obtained from figure 8.5 and a sample volume of $5.25\times10^{-9}\text{m}^3$. From the field sweep in figure 7.16 (page 84), the noise floor is calculated to be 4×10^{-10} A, so the low frequency $\dot{m}$ sensitivity is 1.05×10^{-9} Am^2s^{-1}. This compares with the TLM's $\dot{m}$ resolution of $10^{-8}\,\text{Am}^2\text{s}^{-1}$. The SQUID susceptometer is therefore ten times as sensitive to $\dot{m}$.

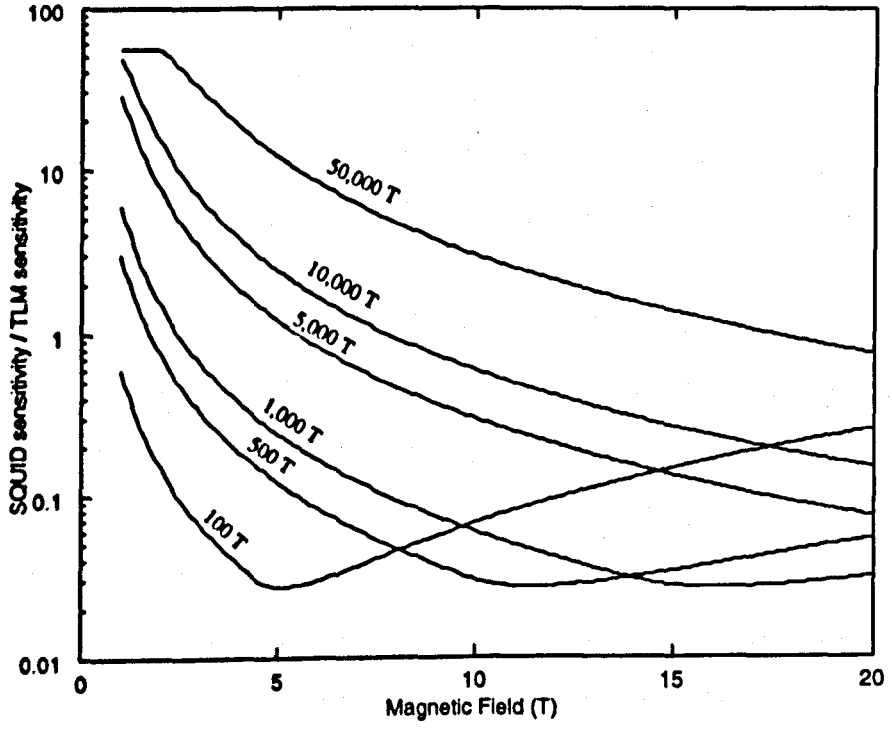

Figure 8.20: Comparison of the sensitivity of the SQUID susceptometer with that of the conventional susceptometer in the TLM refrigerator.

As the susceptometer is intended for dHvA detection, which has a subtle dependence upon all the factors outlined in chapter 4, it is necessary to consider the sensitivity over a range of dHvA

frequencies and magnetic fields (see figure 8.20). It can be seen that the SQUID susceptometer is generally less sensitive at lower dHvA frequencies, because the difference between the linear first order Bessel function and the quadratic second order Bessel function is most apparent. Eventually the conventional susceptometer reaches its Bessel maximum (so the modulation frequency is reduced to keep the signal maximised) whereas the SQUID sensitivity is still rising. This can be seen for e.g. the 100 T frequency below 5 T. For high enough frequencies even the SQUID susceptometer can be optimised as can be seen for the 50,000 T oscillation below 2 T, although under these circumstances field inhomogeneity and impurity effects would dominate. The sensitivities presented here are far less than those presented earlier by Hill [42], for an r.f. SQUID susceptometer. The reason for this is thought to be due to certain incorrect assumptions in the original formulation, about how noise scales with lock-in amplifier bandwidth.

These figures for the sensitivity only tell half the story, and the real achievement is the low temperatures and high magnetic fields available. To allow a fairer comparison, figure 8.12 is replotted for the parameters in a typical conventional susceptometer sweep (see figure 8.21). It can be seen that the SQUID susceptometer covers a far greater area of the parameter space.

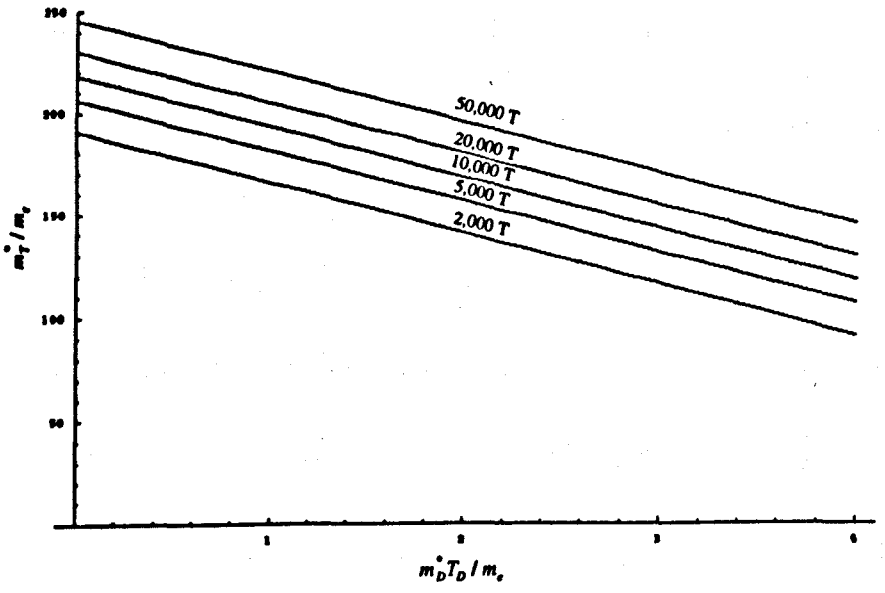

Figure 8.21: The range of available effective masses and Dingle temperatures available for a typical dHvA experiment on the conventional susceptometer.

The susceptometer is still at a formative stage of development and the sensitivities expressed in figure 8.20 represent a fairly conservative design where the emphasis was on making the SQUID stable in high fields. Now that these problems are partially solved it will be possible to boost the sensitivity. There are also a variety of other possible improvements that have come to light in the course of this study.

8.7 Improvements to the system.

Perhaps the most pressing problem to solve will be the removal of all possible origins of background dHvA oscillations. Any solution involving a pure metal like silver will inevitably introduce oscillations. One alternative would be to employ a miniature He bath contained within a cell constructed of an inert material. The technological problems that would need to be overcome to build such a device are formidable. For a start, if the coupling to the sample is not to be dramatically reduced, the pickup coil would have to be located inside the capsule.

A simpler solution would be to still make the connection out of a metal, but choose a compromise between thermal conductivity and Dingle temperature. Fortunately, these are not totally connected properties, and dHvA oscillations are more susceptible to small angle scattering which leaves thermal (and electrical) conductivity relatively unaffected. In this spirit, a work-hardened piece of silver, would perhaps be the best compromise. However, to be certain of not observing any oscillations an alloy would be optimum. Performing a similar calculation to that in section 8.3, it can be seen that a Dingle temperature of 10 K would be sufficient to make any dHvA oscillations undetectable. This could quite easily be achieved by brass, giving a thermal conductivity of typically $\kappa = 10^{-4}$ $Wcm^{-1}K^{-1}$. This is one hundredth of that of silver at similar temperatures but for the present design the estimated thermal resistance will only rise from 22,000 KW^{-1} to 54,000 KW^{-1}, which will be more than compensated for by the reduction in eddy current heating. We would be left with a greater problem of determining the sample temperature, because we could no longer rely on the dominant heating entering the cold finger itself, so it might be necessary to make a second connection to the bottom edge of the crystal. To minimise the length of cold finger that need be constructed out of brass one can see from the calculations in section 8.3 that at a distance of 10mm from the pickup coil centre the signal is reduced by a factor of 60, which should be sufficient. The distance of 10 mm is also a particularly good location to make the connection of the brass to the silver because the modulation field zero is located here (see figure B.1) so it will be possible to have a large surface area of silver in contact, without undue heating.

Once a suitable material is found with which to construct the post, there remains the more challenging problem of attaching the sample to it. Obviously, indium solder can be ruled out because of the problems it has already presented and because it does not wet many of the heavy fermion compounds well. Silver paste is used at present, but we have already seen that only a minute quantity of silver is required to produce visible oscillations. All the alternatives possess flaws. For sufficiently geometric samples it would be possible to clamp them in a miniature brass vice for thermal contact. However, considering the crystalline purity required for these experiments one might doubt whether this method would introduce too many dislocations to the sample. Attaching the sample with G.E. varnish is frankly unpalatable, due to its poor thermal conductivity. Eventually it might suffice to opt for silver paste and measure the background carefully a number of times to see how reproducible the frequencies are. For the large numbers of crystals present, it is likely that the averaging will produce

quite faithfully the 'preferred angle' extremal area frequencies. It should also be noted that this will be less of a problem than that presented by indium due to silver's far simpler Fermi surface.

The next problem to address is the improvement of the smallest detectable dHvA amplitude. An increased signal to noise ratio can be achieved by a combination of three methods. Attempting to reduce the noise in the input circuit, increasing the sensitivity of the input circuit and finally by increasing the modulation amplitude.

The first two problems can be tackled by altering the resistances in the input circuit. The Johnson noise in the input circuit does not respond exactly as one might expect because a resistance will also attenuate current as well as generating voltage. The result of this is that an increased series or parallel resistance actually reduces the Johnson current.

At present the circuit is arranged in a fairly conservative manner with the emphasis on stability to rapid flux changes, however now that this problem has largely been solved, we can review whether it is worth increasing the parallel resistor. This would not be an immediately simple procedure because, while it is possible to quantify the effects on the Johnson noise as the parallel resistor is reduced, it is rather more difficult to foresee what effect it will have on the stability of the susceptometer. Although attempts were made to gain a more quantitative understanding of the vibrations originating in the magnet, they were found to not only be dependent upon sweep rate but also the history of the magnet. This manifested itself in the calm half tesla at the beginning of each sweep and also a tendency for there to be less vibrations after the magnet had been ramped a few times. In short, there were rather too many variables to get a systematic picture of how many jumps could be expected and what their amplitudes would be for a particular sweep. One clearly apparent result, was that after the magnet had been well trained, it was possible to sweep at 0.005 T/min in the knowledge that approximately 80 % of the time, no jumps will be present of any amplitude. Using this as a guide it might be tempting to start experimenting with a higher parallel resistor. However by increasing the resistance from 0.02 to 0.2 Ω the noise will only drop by 25 % and the cutoff will increase to well above the SQUID slew rate, so this is considered an improvement best left for when it becomes a case of really 'fine-tuning' the system.

The series resistor is slightly easier to quantify and in this case it is a balance between reducing the resistance to gain extra sensitivity and the higher Johnson and vibrational noise one can expect. The simple model outlined in chapter 5 indicated that overall, a reduction in the series resistance will increase the ratio of the input circuit I/V transfer function, $T(f)$, to the noise floor.

The improvement to the signal strength can be seen in figure 8.22. One can preserve the same signal by keeping b_0 constant and reducing ω, so for the same amount of heating one can increase b_0. This must be balanced against the rising amplitude of the low frequency vibrations, visible in figure 5.18. The maximum vibration produces a current of 2.5×10^{-7} A, which, for a gain of ×200 corresponds to 1.5 V, so these vibrations are already on the edge of what is tolerable. However, these problems can be solved. It was observed that application of a field as small as 0.5 T to the demagnetisation stage was sufficient to reduce the vibrational noise in the main field SQUID by a factor of four. It is

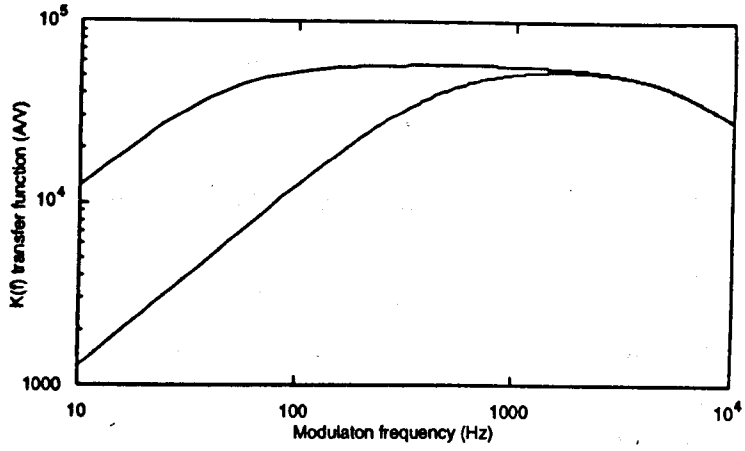

Figure 8.22: The predicted frequency responses with the current input circuit (series resistor = 0.05 Ω) and with a smaller series resistor (0.005 Ω). With the new circuit K(83Hz) is five times larger, but unfortunately K(20Hz) is nine times larger.

also possible to operate the SQUID at a lower gain and compensate for this by operating the lock-in amplifier with a higher gain. Most importantly of all, it would appear that these oscillations are due to the motion of the demagnetisation stage, so perhaps the problem could be solved by holding it in place with nylon spacers touching the radiation shield. If these were 10 mm long with a 0.2 mm by 0.2 mm cross section, they would introduce a heat leak of less than 5×10^{-12} W each. There are also plans to construct a larger demagnetisation stage, so more effort can be put into ensuring that it is connected very rigidly to the mixing chamber.

We might also ask whether the vibrations might show up as noise on the dHvA measurement itself. However, if we operate the modulation field at 83 Hz we are separated from the dominant 20 Hz oscillations by 63 Hz. For a lock-in time constant of 1s, this contribution will be attenuated by a factor of 4×10^{-11}, placing it well below the noise floor.

So with a combination of each of these developments, it should be possible to reduce the series resistor to 0.005 Ω with the only adverse consequence being that the low frequency Johnson noise rises by a factor of two.

One might consider whether it would be possible to replace the resistors with capacitors, so that no Johnson noise is generated. Unfortunately this is impossible, because it would require a capacitance of 3 mF, which would clearly be impractical. However, it is possible to reduce the Johnson noise quite dramatically by locating the resistances in a region at a lower temperature. A suitable position would be in the low field region at the base of the demagnetisation stage. There already exists a junction box to hold the electronic balancing coil and this could be extended to house and heat-sink the resistances. It should be simple to heat sink the resistors because the heat generated in them will be infinitesimally small ($\approx 10^{-11}$ W). One concern is that the input circuit gain might change with temperature, but this is unlikely as the thermal coefficient of manganin is vanishing at low temperatures. Reducing the temperature of the tags to 3 mK, it should then be possible to reduce the Johnson noise by a factor of 22, giving a new value of 1.4×10^{-11} A/$\sqrt{\text{Hz}}$.

Next comes the question of what is the maximum possible modulation signal that can be applied. The limitations on this, are sample heating, background susceptibility and in the case of the main field susceptometer, magnet heating. It is here where principle and practice will probably diverge most strongly, so conservative estimates will be used throughout.

Whilst the $CeCu_2Si_2$ experiments were being conducted, a third SQUID was installed on the refrigerator with an unshielded pickup coil, to assess the possibility of abandoning all the r.f. shielding. The results of these tests were slightly ambiguous. The SQUID did work reliably and was completely free from the intermittent unlocking that was found in transport Dewar tests. This can be ascribed to the fridge behaving like a Faraday cage and the care that was taken to filter all electrical connections. However, the noise floor was reduced in an anomalous way at high frequencies, suggesting that a change had occurred to the SQUID. This SQUID had been used for the early prototyping work and so endured numerous thermal cycles, and it appeared that it had eventually failed to operate reliably. This idea was confirmed by re-testing the SQUID in a transport Dewar, where it showed the same behaviour. The noise test is still of some validity because it was still found to be possible to introduce a signal to the SQUID from a very remote modulation coil although it was not possible to measure its sensitivity directly. However, even if some of the higher frequencies were being attenuated, a similar effect can be achieved with a parallel resistance, so it would appear to be safe to remove the r.f. screening.

Considering first the sample heating, it has already been shown in section 7.3 that eddy current heating from the silver shielding is 1000 times that due to the sample itself, so if the silver shielding is removed it will be possible to use $b_0\omega \approx 0.4\,\mathrm{Ts}^{-1}$, which for a modulation frequency of 83 Hz, corresponds to a b_0 of 8×10^{-4} T. It is necessary to consider what this corresponds to in terms of Joule heating in the modulation coil. The field/current transfer function for the modulation coil is 2×10^{-3} T/A, and the estimated resistance of the modulation coil is 20 mΩ at 4 K and 17 T. So currently the Joule heating in the bath is only 3.5×10^{-7} W. Increasing the modulation field b_0 to 8×10^{-4} T will increase this to 8×10^{-3} W. The latent heat of evaporation of ^{4}He is 2.56 kJ/l, so this kind of heat input would only boil off 0.3 l/day. It should also be remembered that the modulation coil is in close proximity to the main magnet, so care must be taken to avoid a magnet quench. It is difficult to predict this effect, although in our top loading cryostat, which also possesses a modulation coil in the bore of the superconducting magnet, it is possible to apply magnetic fields of up to 0.1 T.

What will probably limit the current more than heating effects will be reliably balancing the SQUID. Problems will arise from two directions. There will no doubt remain some field dependent background susceptibility after the silver has been removed. The early attempts at dynamically balancing the signal phase presented in chapter 5, indicate that the method is viable if a suitable function generator can be found capable of varying the amplitude in a smooth enough manner. Discussions are currently underway with the physics department electronics group to construct such a device and all the suitable software is already written. There will also be a problem of finding a current generator with a low enough noise level. As a result of all these factors the maximum permissible modulation

field is assumed to be only 1×10^{-4} T. When all these estimates are combined together, one obtains the new values presented in table 8.4.

	Current value	Value after modifications
K(83) (A/V)	10,300	58,500
S(83)	0.73	1
Noise floor (A)	3×10^{-10}	1.4×10^{-11}
b_0 (T)	1×10^{-5}	1×10^{-4}

Table 8.4: Estimates of the improvements that can be made to the susceptometer.

It is now possible to replot figure 8.20, with the new parameters to obtain figure 8.23. It therefore appears that the improvements would be well worthwhile. The SQUID susceptometer would also have the useful property of always being more sensitive than the conventional susceptometer. So it would then be possible to use the top loading refrigerator, as a 'filter' for good samples, which would then be guaranteed to show dIIvA oscillations in the (time consuming) SQUID susceptometer.

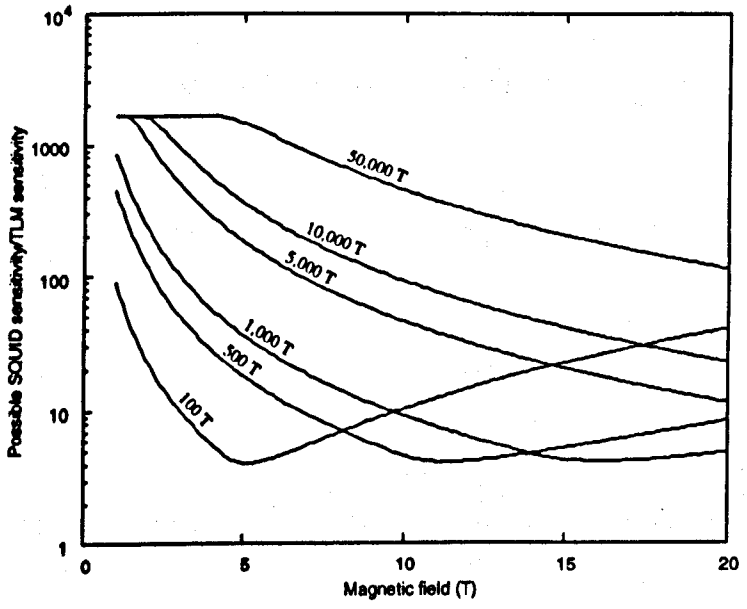

Figure 8.23: The possible ratios of sensitivities achievable if the modification discussed in this chapter are implemented.

Chapter 9

Conclusion.

This thesis is concluded by summarising the key results of these experiments and by considering some of the developments that would improve the cryomagnetic system. The principle achievement is the construction of the d.c. SQUID susceptometer. The previous r.f. SQUID susceptometer worked only intermittently, but with the continual improvement of commercially available SQUIDs it became possible to construct a reliable high sensitivity susceptometer. In the course of developing the system, some previously hidden problems came to light. The issue of magnet vibrations was partially solved and currently, if one sweeps the magnet slowly enough (which is necessary in these experiments anyway) the vibrations are not present. Electronic balancing was successful for this particular experiment, where phase changes in the susceptibility were the dominant contribution (rather than amplitude changes). It will probably be desirable in the future to develop a dynamic balancing system which could balance amplitude to the same accuracy. This will be of particular importance if any studies of dIIvA oscillations in the superconducting state are attempted.

A series of experiments were conducted on the heavy fermion compound $CeCu_2Si_2$. There was a large diversity of oscillations observed, however subsequent background tests conclusively showed that the majority of oscillations were due to contaminants in the experimental area. There were some oscillations which could conceivably have originated from the sample although, until more conclusive experiments are conducted, they must be viewed with caution.

By looking at the superconducting transition of $CeCu_2Si_2$ it was possible to derive a value for the sensitivity of the susceptometer and, whilst being consistent with an absence of the low frequency oscillations in the sample, suggested that it was unusual that no high frequency oscillations were visible. The absence of oscillations has been discussed in relation to experimental details and consequences for $CeCu_2Si_2$.

There were a variety of other anomalous properties that were traced to a design flaw of having a damping of the signal due to r.f. shielding. A more curious property observed was in relation to the metamagnetic transition of $CeCu_2Si_2$, which on the evidence of this experiment, would appear to have a height that depends upon sweep rate.

Along the way much insight has been gained in how to improve the susceptometer, and a series of modifications were suggested that should boost the sensitivity to greater than that of a conventional susceptometer, whilst still maintaining temperatures below 3 mK.

It can be seen that many technical problems have been overcome, and no doubt many more await. It is therefore relevant to ask if there is a simpler way of performing this experiment. The most important parameter in the study of heavy fermions must surely be temperature, and in previous studies using a conventional susceptometer it was found that it was not possible to reliably cool the sample to less than 20 mK and still maintain a good signal. To achieve lower temperatures one is then forced to mount the sample on metal to make thermal contact and the issue of eddy current heating is immediately heightened. It is possible to try and solve these problems using conventional voltage amplification and better coil design. One can strive to employ thinner wire to improve the coil coupling constant and it is possible to achieve better signal to noise properties using a cold transformer. However, it seems that these methods will asymptotically approach some limit, while admittedly many useful experiments are performed along the way.

The instant one adopts the idea of using a SQUID there is a tremendous amplification available. Nevertheless, there are clear problems encountered too. Commercial SQUIDs are only just at the stage where they may be used without concern about their reliability, and when a SQUID is detecting in a large field, the difficulties are multiplied. In this study a particular problem was encountered from vibrational sources in the main magnet, and whilst these problems were being solved it was not possible to reliably obtain data. Similar problems due to background signals have made it difficult to draw conclusive inferences from these experiments. However, it is worth persevering, because when these problems are solved there will instantly be a range of experiments possible that could not be performed on a conventional susceptometer. This is most evident in the m_T^*/m_e, $m_D^* T_D/m_e$ phase diagrams presented in chapter 8. If it eventually becomes possible to map out the *entire* Fermi surfaces of the heavy fermion compounds then it should finally be possible to discriminate between the rival theories and gain insight into the nature of the heavy quasiparticles.

Appendix A

SQUID operation.

SQUIDs have reached the stage of development that they can generally be regarded as a black-box for most applications. However, in this experiment alterations were made to the wiring employed, so it became necessary to consider the function of the device in more detail. This appendix will present the basics of SQUID operation and introduce some of the SQUID jargon employed in the thesis.

Initially consider the behaviour of a fully superconducting ring. The order parameter of the superconducting wavefunction is denoted by a complex number, ψ_0, multiplied by a phase factor, $\exp(\phi i)$. (The group velocity is given by $\nabla\phi$). In the presence of a magnetic field the order parameter is

$$\psi = \psi_0 \exp\left(\frac{2eAi}{\hbar}\right) \tag{A.1}$$

The order parameter must always be single valued, so if we consider a loop geometry as shown in figure A.1 a, we demand

$$\frac{2e}{\hbar}\oint \mathbf{A}\cdot d\mathbf{l} = 2\pi n \tag{A.2}$$

Applying Stokes' theorem, one finds

$$\oint \mathbf{A}\cdot d\mathbf{l} = \int \nabla\times\mathbf{A}\cdot d\mathbf{S} = \int \mathbf{B}\cdot d\mathbf{S} = \Phi \tag{A.3}$$

so

$$\Phi = \frac{2\pi n\hbar}{2e} = \Phi_0 n \tag{A.4}$$

where

$$\Phi_0 = \frac{h}{2e} \tag{A.5}$$

Therefore, the total flux in the ring is always a multiple of the flux quantum, $\Phi_0 = \frac{h}{2e} = 2.0678\times 10^{-15}$ Wb, because superconducting screening currents produce a diamagnetic response. If one were to start off with no field and gradually increase it, the flux in the ring would remain zero (as in the inside of a simply connected piece of superconductor) until eventually the screening currents would exceed the the critical current of the superconductor. Then the ring would go normal allowing an uncontrolled amount of flux to enter to bring the flux in the ring to a different multiple of Φ_0.

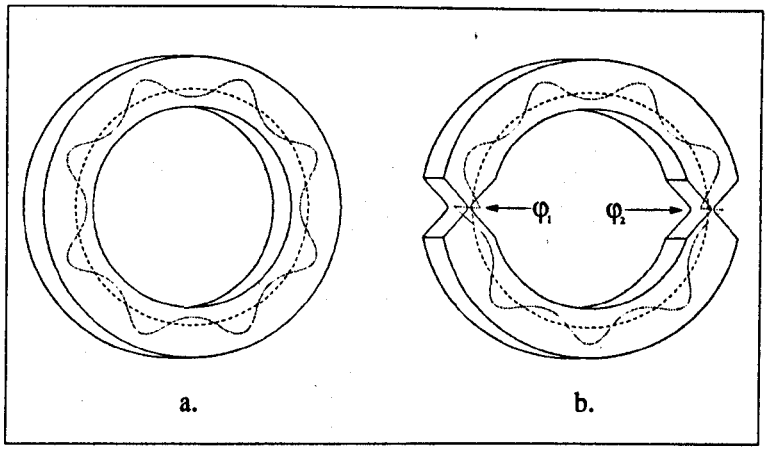

Figure A.1: Schematic illustrations of a component of the order parameter (e.g.$\Re(\psi)$) for different configurations. Note, this is not the phase ϕ, which is linear except at the junctions, where it jumps discontinuously. Part (a.) depicts the situation for a solid superconducting ring, and part (b.) a ring possessing 2 weak links. The discontinuities in $\Re(\psi)$ result from discontinuities in the phase ϕ_1 and ϕ_2.

In the case of a d.c. SQUID there are two weak links present that each have a critical current comparable with that generated by half a flux quantum. The weak links (Josephson junctions) can be of many different forms such as a constriction or a thin insulating barrier.

The operation of the SQUID relies on some properties of weak links, derived by Josephson [86]. The d.c. Josephson effect shows that there is a phase shift in the order parameter at the junction whenever a current flows through it.

$$I_S = I_c \sin\phi \tag{A.6}$$

where I_c is the critical current of the weak link. The a.c. Josephson effect indicates that the phase change evolves continuously if a voltage is established across the junction.

$$\frac{d\phi}{dt} = \frac{2eV}{\hbar} \tag{A.7}$$

For a finite voltage, the two effects together produce an oscillating current of frequency $2eV/h$. Considering a ring possessing two weak links, and applying the d.c. Josephson effect there is an additional phase shift ϕ_1 and ϕ_2 at each of the junctions (see figure A.1 b). By analogy to equation A.3 and considering a complete circuit one must allow for the difference of these two phase changes $\Delta\phi = \phi_1 - \phi_2$.

$$\Delta\phi - \frac{2e}{\hbar}\oint \mathbf{A}\cdot d\mathbf{l} = 2\pi n \tag{A.8}$$

so

$$\Delta\phi = 2n\pi + 2\pi\left(\frac{\Phi}{\Phi_0}\right) \tag{A.9}$$

If one attaches contacts to the top and bottom of the SQUID and conducts an experiment to measure

the critical current of the entire device, it will simply be the sum of the two junction's critical currents.

$$I_c^{Total} = I_c^1 \sin(\phi) + I_c^2 \sin(\phi + \Delta\phi) \tag{A.10}$$

Assuming that the junctions are identical, using trigonometric identities and equation A.10, one finds

$$I_c^{Total} = 2I_c \left| \cos\left(\frac{\pi\Phi}{\Phi_0}\right) \right| \tag{A.11}$$

where the modulus sign shows that we are only concerned in the value of the critical current and not its direction. The result, known as the Mercereau effect, shows that the critical current is now a periodic function of the flux inside the ring, Φ.

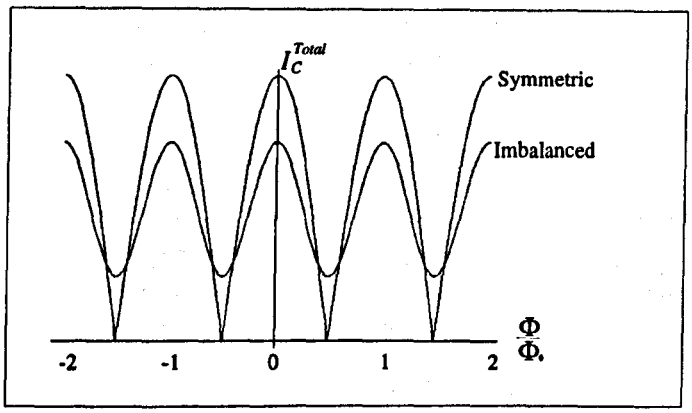

Figure A.2: Illustration showing how the flux dependence of the critical current is modified by having junctions of different critical currents. The curve begins to resemble a sine curve.

This is the main principle behind the flux interferometer. The d.c. SQUID is a device which allows this periodicity to be measured continuously, rather than by performing a series of critical current experiments. Other points to note are that Φ is the flux inside the SQUID ring, including the contribution from screening currents, and need not be a multiple of Φ_0, as is the case for a perfectly superconducting ring. If the critical currents of the two junctions are not identical the curve is rounded off (see figure A.2) and if we wish to plot the externally applied flux instead, the curve is slanted.

In order to detect the variation, the SQUID is biased at a constant current, just above $2I_c$, and the voltage generated is measured (see figure A.3). One aims to maximise the range of the voltage swing produced, by choosing a suitable value of *bias* current.

For insensitive measurements it would suffice to count the number of voltage maxima to calculate the change in flux, however the SQUID is usually used in a mode where the flux in the ring is continually nulled and the signal fed back is a measure of the flux (see figure A.4). The strength of the feedback signal (the *modulation*) is another tuning parameter.

For large rates of change of field it is possible for the slew rate of the feedback electronics to be exceeded so it locks on to the next flux quanta. This event is known as *unlocking*. Each unlocking will generally cause a larger modulation signal to be fed back to the SQUID so if the effects are cumulative it can compromise the SQUID performance, as the feedback electronics fails to deliver a suitable current. To prevent this happening it is possible to programme a *reset* - a fixed amount

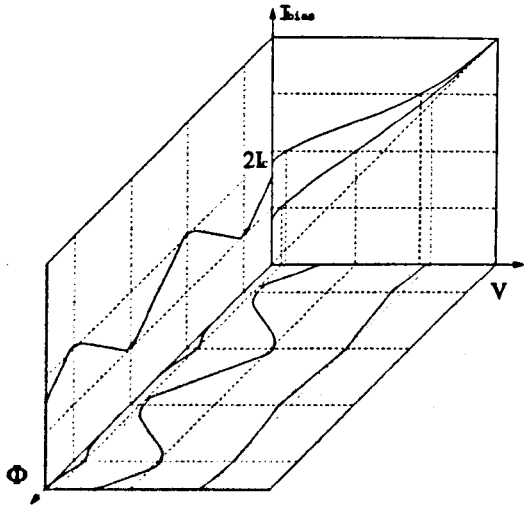

Figure A.3: Plot displaying the behaviour of a d.c. SQUID when biased by a current.The periodic nature of the critical current manifests itself in the V/I curve so a finite current across the ring produces a flux dependent voltage. The voltage swing is a maximum when the SQUID is biased just above its (integer Φ_0) critical current.

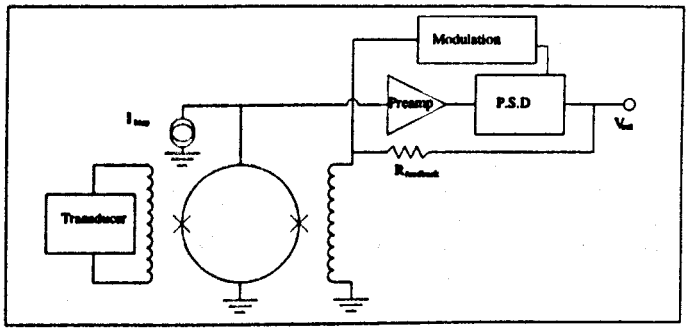

Figure A.4: The feedback circuit of a d.c. SQUID. To achieve optimum performance, one tunes the bias current and the feedback voltage. The feedback circuit is located at room temperature. As the cable was changed there is an extra resistance introduced to all lines going to the SQUID. After Gallop [87].

of modulation current at which the feedback circuit finds its zero again. While a reset occurs, the SQUID output voltage fluctuates, so these events are strongly detrimental to experiments.

Appendix B

The Modulation Coil

This appendix summarises the installation of the main field modulation coil, which was designed by Hill and installed and tested by Hill and the author. The original design of the modulation coil was a small solenoid wound on a *Hysol* [88] former. As the ambient magnetic field exceed the critical field of most superconducting wire (NbSn was not suitable for this application) it was necessary to use Cu wire.

Considering a small Cu modulation coil employing 0.3 mm diameter wire driven by a current of 7 mA at 200 Hz, there will be a resistive heating of 1 μW (If the resistance is assumed to be 20 mΩ at 4 K and 10 T). However, the eddy current heating into the silver post is estimated to be only 5 nW.

It therefore seemed beneficial to locate the modulation coil away from the sample, and attach it to the inside of the main field magnet. A slender coil former slots between the bore of the main magnet and the IVC. In order to reduce the modulation field over the large diameter section of the silver cold finger, cancellation coils were added. The positions of these have been optimised to also minimise the out of balance signal induced by the modulation field in an empty pickup coil pair. Figure B.1 shows the calculated field profile in relation to the position of the cold finger, sample and pickup coils. The main coil is 10 mm long, centred at z=0, with two cancellation coils; the first 7 mm long, centred at z=11.5 mm, and the second 2 mm long, centred at z=17 mm. All coils have two layers of (0.35 mm diameter) windings. The sample is centred on the main field maximum at z=0.

After installation, the field profile was measured with a 100 turn search coil mounted 21 mm below the base of the r.f. shield. It was possible to measure the field profile of the modulation coil by simply applying a sinusoidal signal and measuring the output of the pickup coil with a lock-in amplifier. The field profile of the main magnet was measured by performing a four terminal measurement of the pickup coil magnetoresistance. The results are displayed in figure B.2. It can be seen that the form of the measured field profile fits the predicted one rather well, although its maximum is closer to the main field maximum than desired, leading to a larger out of balance signal.

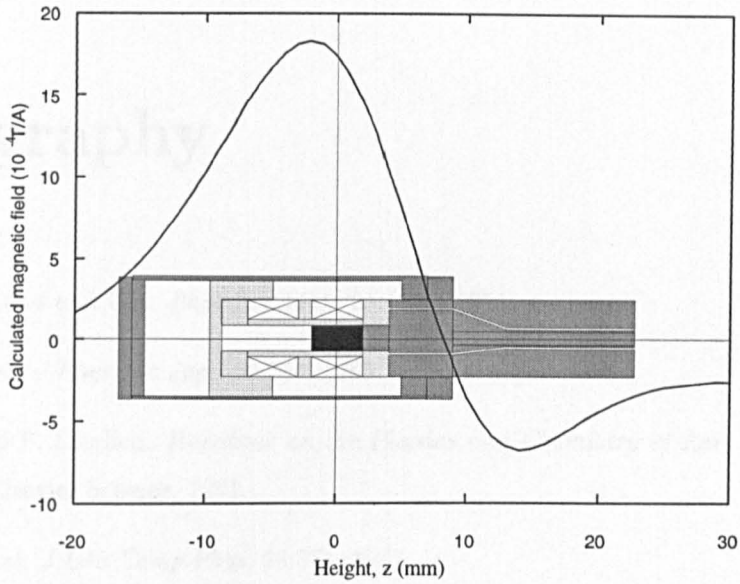

Figure B.1: The predicted field profile for the modulation coil.

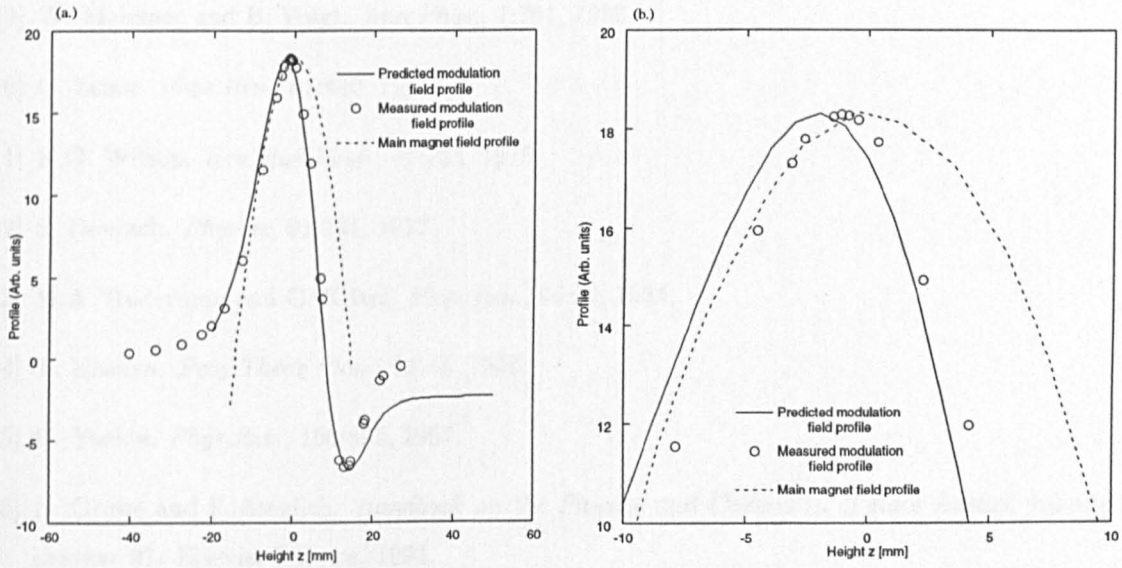

Figure B.2: Comparison of the predicted and measured field profiles of the modulation coil. The main magnetic field profile is also measured using magnetoresistance. The y-axis is not to scale. Part (a.) shows the general form of the curve and part (b.) shows the detail close to the sample region.

Bibliography

[1] Graebner Andres and Ott. *Phys.Rev.Lett.*, 35:1779, 1975.

[2] Y. Onuki et al. *J.Phys.Soc.Jap.*, 54:304, 1985.

[3] N. Grewe and F. Steglich. *Handbook on the Physics and Chemistry of Rare Earths*, volume 14, chapter 97. Elsevier Science, 1991.

[4] A. Amato et al. *J.Low Temp.Phys*, 68:371, 1987.

[5] H.R. Ott. *Phys.Rev.B*, 33:126, 1986.

[6] H.R. Ott et al. *Solid State Comm.*, 53:235, 1985.

[7] L. Landau. *Sov.Phys.JETP.*, 8:70, 1959.

[8] Peter Fulde. *Electron Correlations in Molecules and Solids.* Springer Verlag, 1991.

[9] W. Meissner and B. Voigt. *Ann.Phys.*, 7:761, 1930.

[10] C. Zener. *Phys.Rev.*, 81:440, 1951.

[11] K.G. Wilson. *Rev.Mod.Phys.*, 47:773, 1975.

[12] S. Doniach. *Physica*, 91:231, 1977.

[13] M.A. Ruderman and C. Kittel. *Phys.Rev.*, 96:99, 1954.

[14] T. Kasuya. *Prog.Theor.Phys.*, 16:45, 1956.

[15] K. Yosida. *Phys.Rev.*, 106:893, 1957.

[16] N. Grewe and F. Steglich. *Handbook on the Physics and Chemistry of Rare Earths*, volume 14, chapter 97. Elsevier Science, 1991.

[17] P.W. Anderson. *Phys.Rev.*, 124:41, 1961.

[18] Z. Tesanovic and O.T. Valls. *Phys.Rev. B.*, 34:1918, 1986.

[19] D.M. Newns and O.T. Read. *Adv.Phys.*, 36:799, 1987.

[20] P. Coleman. *Phys.Rev. B.*, 29:3035, 1984.

[21] L.H. Thomas. *Proc.Cambridge Philos. Soc.*, 23:542, 1927.

[22] E. Fermi. *Z.Phys.*, 48:73, 1928.

[23] P. Hohenberg and W. Kohn. *Phys.Rev.*, 136 B:864, 1964.

[24] W. Kohn and L.J. Sham. *Phys.Rev.*, 140 A:1133, 1965.

[25] G. Zwicknagl. *Physica Scripta.*, T49:34, 1993.

[26] G.G. Lonzarich. *J.Magn.Magn.Mat.*, 76-77:1, 1988.

[27] Kagan et al. *Physica B.*, 182:201, 1992.

[28] L.W. Shubnikov and W.J. de Haas. *Proc.Netherlands Roy.Acad.Sci.*, 33:130, 1930.

[29] D. Shoenberg and B.R. Watts. *Phil.Mag*, 15:1275, 1967.

[30] P. Sullivan and G. Seidel. *Pys.Lett.*, 25 A:229, 1967.

[31] Mavroides et al. *Phys.Rev.Lett.*, 9:451, 1962.

[32] N.W. Ashcroft and D. Mermin. *Solid State Physics.* Saunders College Publishing, 1976.

[33] I.M. Lifshitz and A.M. Kosevich. *Dokl.Akad.Nauk. SSR*, 96:963, 1954.

[34] R.B. Dingle. *Proc.Roy.Soc*, A 211:517, 1952.

[35] D. Shoenberg. *Magnetic oscillations in metals.* Cambridge University Press, 1984.

[36] J.M. Luttinger. *Phys.Rev.*, 119:1153, 1960.

[37] A.B. Fowler. *Physics*, 1:315, 1965.

[38] S. Englesberg and G. Simpson. *Phys.Rev.B.*, 2:1657, 1970.

[39] A. Wasserman and M. Springford. *Adv.Phys.*, 45:471, 1996.

[40] D. Shoenberg and P.J. Stiles. *Proc.Roy.Soc*, A 281:62, 1964.

[41] C.M. Varma. *Comments solid state phys.*, 11:221, 1985.

[42] R.W. Hill. *PhD Thesis.* University of Bristol.

[43] Oxford Instruments. Oxford, OX8 1TL, (0865) 882855.

[44] R.M. Mueller et al. *Rev.Sci.Instr.*, 49:515, 1978.

[45] F. Pobell. *Matter and methods at low temperatures.* Springer-Verlag, 1992.

[46] D.S. Greywall. *Phys.Rev.B*, 33:7520, 1986.

[47] Straty and Adams. *Rev.Sci.Instr.*, 40:1393, 1969.

[48] Conductus Inc. 10623 Roselle Street, San Diego, CA 92121,U.S.A.

[49] J.C. Gallop. *SQUIDs, the Josephson Effects and Superconducting Electronics.* Adam Hilger, IOP Publishing, Techno House, Redcliffe Way, BRISTOL, BS1 6NX, 1990.

[50] T. van Duzer and C.W. Turner. *Principles of Superconductive Devices and Circuits.* Elsevier, 52 Vanderbilt Avenue, New York,10017, 1981.

[51] Mathematica. Wolfram Research Europe Ltd, info@wolfram.co.uk.

[52] T. Jarlborg et al. *Z.Phys.B.*, 52:295, 1983.

[53] P. Gegenwart. *Phys.Rev. B*, 230-232:572–575, 1997.

[54] Müller-Reisener. *PhD Thesis.* University of Darmstadt, 1995.

[55] F. Steglich et al. *Phys.Rev.Lett.*, 43:1892–1896, 1979.

[56] H. Nakamura et al. *J.Magn.Magn.Mater.*, 76-77:517, 1988.

[57] U. Rauchschwalbe et al. *J.Magn.Magn.Mater.*, 63-64:447, 1987.

[58] M. Lang et al. *Physica Scripta*, T39:135, 1991.

[59] Y.J. Uemura et al. *Phys.Rev. B*, 39:4726, 1989.

[60] O. Trovarelli et al. *Phys.Rev.B.*, 56:678, 1997.

[61] F. Steglich et al. *Physica B.*, 237:192, 1997.

[62] S. Horn et al. *Phys.Rev.B*, 23:3171, 1981.

[63] D. Vasumathi et al. *Phys.Rev.B*, 55:11,714, 1997.

[64] M. Hunt et al. *J.Phys.Cond.Mat.*, 2:6859, 1990.

[65] H. Harima and A. Yanase. *J.Magn.Magn.Mat.*, 108:145, 1992.

[66] J. Sticht et al. *Z.Phys.B.*, 65:149, 1986.

[67] J. Kang et al. *Phys.Rev.B.*, 41:6610, 1990.

[68] H. Razafimandimby et al. *Z.Phys.B.*, 54:111, 1984.

[69] N.D. Mathur et al. *Nature*, 394:39, 1998.

[70] A. Bjorneklett et al. *Int.J.Adhesion.Adhesives.*, 12:99, 1992.

[71] R.W. Hill. *PhD Thesis*, 1996.

[72] J.H.B. van Weeren and J.R. Anderson. *J.Phys.F.*, 3:2109, 1973.

[73] Alpha catalogue. Johnson Matthey.

[74] Z. Fisk et al. *Science*, 239:33, 1988.

[75] A.B. Pippard. *Magnetoresistance in metals.* Cambridge University Press, 1989.

[76] U. Rauchschwalbe. *Physica B.*, 147:1, 1987.

[77] U. Joseph and A.C. Thorsen. *Phys.Rev.*, A138:1159, 1965.

[78] M.R. Halse. *Phil.Trans.Roy.Soc.*, A265:507, 1969.

[79] W.J. O'Sullivan et al. *Phys.Lett.*, 27A:144, 1968.

[80] M. Hunt. *PhD Thesis.* University of Bristol, 1992.

[81] S. Chapman et al. *J.Phys.Cond.Matt.*, 2:8123, 1990.

[82] B. Andraka et al. *Phys.Rev.B.*, 39:6420, 1989.

[83] B. Andraka et al. *Phys.Rev.B.*, 48:3939, 1993.

[84] M. Takashita et al. *J.Phys.Soc.Jap.*, 65:515, 1996.

[85] A.J. Hughes and J.P.G. Shepherd. *J.Phys.C*, 2:661, 1969.

[86] B.D. Josephson. *Phys.Lett.*, 1:251, 1962.

[87] J.C. Gallop. *SQUIDs, the Josephson effects and superconducting electronics.* Adam Hilger, 1991.

[88] Dexter Hysol. Rose Industrial Estate, Bourne End, Buckinghamshire.